Development and Analysis of Advanced Techniques for GNSS Receivers

POLITECNICO DI TORINO

SCUOLA DI DOTTORATO

Research Doctorate Course in

Elettronica e delle Comunicazioni

XXVI ciclo

Final Dissertation

Development and Analysis of Advanced Techniques for GNSS Receivers

Xinhua Tang

Tutor	Coordinator of the Research Doctorate Course
prof. Letizia Lo Presti	prof. Ivo Montrosset

25 January 2014

To my family

Try not to become a man of success but rather try to become a man of value.

by

Albert Einstein

Acknowledgments

I would like to express sincere gratitude to my supervisor Prof. Letizia Lo Presti for her supervision, continuous caring and patience throughout my research all these three years. It is her who first pointed out the correct direction for me in Ph.D. study and guided me to the deep heart of the GNSS techniques. Her personal quality impressed me a lot and gave me the hint of definition of a real scholar.

A special thanks to my co-tutor Emanuela Falletti who squeezed out her precious time to supply continuous support, valuable discussions and constructive suggestions for me. Her help saved me much time and energy which smoothed my Ph.D. life dramatically. Meanwhile, she set a good example for me to be positive and understanding.

I owe special thanks to Gianluca Falco,Davide Margaria and Muhammad Tahir for their guidance in special research topics.

Thanks to all the colleagues in NavSas group for making the life in lab colorful and providing the pleasurable environment, especially for selfless help both in research and daily life, I would like to express my apology that I cannot enlist all the names here.

Finally, i am greatly thankful to my parents, my wife, my parents-in-law, my younger brother, my uncles and aunts for their unconditional love, without their support both economically and mentally, i would never have gotten this far.

Abstract

With the rapid development of digital techniques, the concept of software-defined radio (SDR) emerged which accelerates the first appearance of of the real-time GNSS software receiver at the beginning of this century, in the frame of a software receiver, this thesis mainly explores the possible improvement in parameters estimate such as frequency estimate, code delay estimate and phase estimate.

In the first stage, acquisition process is focused, the theoretical mathematical expression of the cross-ambiguity function (CAF) is exploited to analyze the grid and improve the accuracy of the frequency estimate. Based on the simple equation derived from this mathematical expression of the CAF, a family of novel algorithms are proposed to refine the Doppler frequency estimate. In an ideal scenario where there is no noise and other nuisances, the frequency estimation error can be theoretically reduced to zero. On the other hand, in the presence of noise, the new algorithm almost reaches the Cramer-Rao Lower Bound (CRLB) which is derived as benchmark. For comparison, a least-square (LS) method is proposed. It is shown that the proposed solution achieves the same performance of LS, but requires a dramatically reduced computational burden. An averaging method is proposed to mitigate the influence of noise, especially when signal-to-noise ratio (SNR) is low. Finally, the influence of the grid resolution in the search space is analyzed in both time and frequency domains.

In the next step, a new FLL discriminator based on energy is proposed to

adapt to the changes brought by the new introduced signal modulation. This new discriminator can determine the frequency error only using the minimum period of data, it can also extend the pull-in range to nearly six times larger as the traditional arctangent discriminator. The whole derivation of the method is presented. From the comparison with traditional ATAN and another similar discriminator that is also based on energy, it is shown that the new proposed discriminator can inherit the merits of these two references, avoiding their drawbacks at the same time. Owing to the property of the new discriminator, in case of composite GNSS signals such as Galileo E1 Open Service (OS) signal, coherent combination of data and pilot channels can be adopted to improve the frequency estimate by exploiting the full transmitted power.

In order to incorporate all the available information, the structure of a tracking loop with Extended Kalman Filter (EKF) is analyzed and implemented. The structure of an EKF-based software receiver is proposed including the special modules dedicated to the initialization and maintenance of the tracking loop. The EKF-based tracking architecture has been compared with a traditional one based on an FLL/PLL+DLL architecture, and the benefit of the EKF within the tracking stage has been evaluated in terms of final positioning accuracy. Further tests have been carried out to compare the Position-Velocity-Time (PVT) solution of this receiver with the one provided by two commercial receivers: a mass-market GPS module (Ublox LEA-5T) and a professional one (Septentrio PolaRx2e@). The results show that the accuracy in PVT of the software receiver can be remarkably improved if the tracking is designed with a proper EKF architecture and the performance we can achieve is even better than the one obtained by the mass market receiver, even when a simple one-shot least-squares approach is adopted for the computation of the navigation solution. Furthermore in depth, KF-based tracking loop is analyzed, a control model is derived to link the KF system and the traditional one which can provide an insight into the advantages of KF system.

Finally, conclusions and main recommendations are presented.

Table of contents

List of tables

List of figures

List of acronyms

ATAN	Arctangent
ACF	Autocorrelation Function
ADC	Analog to Digital Converter
AltBOC	Alternative Binary Offset Carrier
AWGN	Additive White Gaussian Noise
BOC	Binary Offset Carrier
CRLB	Cramer-Rao Lower Bound
BPSK	Binary Phase Shift Keying
CAM	Channel Access Methods
C/A	Clear/Acquisition or Coarse/Acquisition
C/N_0	Carrier-to-Noise-Density Ratio
CDMA	Code Division Multiple Access
CBOC	composite binary offset carrier
CAF	Cross-Ambiguity Function
DLL	Delay Lock Loop
DFT	Discrete Fourier Transform
DSP	Digital Signal Processor
DSSS	Direct Spread Spectrum Sequence
EU	European Union
EKF	Extended-Kalman-Filter
FFT	Fast Fourier Transform
FLL	Frequency Lock Loop
FDMA	Frequency Division Multiple Access

GDOP	Geometric Dilution of Precision
GIOVE-A,B	Galileo Test Satellites
GLONASS	Global Orbiting Navigation Satellite System
GPS	Global Positioning System
GNSS	Global Navigation Satellite System
GPRS	General Packet Radio Service
GSM	Global System for Mobile Communications
I	In-Phase Component
ICD	Interface Control Document
IEEE	International Electrical and Electronic Engineers
IF	Intermediate Frequency
INS	Inertial Navigation System
IMU	Inertial Measurement Unit
KF	Kalamn Filter
LUT	Look-Up Table
LORAN	Long-range Radio Navigation
LFSR	Linear Feedback Shift Register
LTI	Linear Time-Invariant
LS	Least Squares
ML	Maximum-Likelihood
MGF	Mason's Gain Formula
NCO	Numerically Controlled Oscillator
OS	Open Service
PDF	Probability Density Function
PLL	Phase Lock Loop
PN	Pseudo Noise
PRN	Pseudo-Random Noise
PSD	Power Spectral Density
PFT	Preparation-For-Tracking

PSK	Phase Shift Keying
PVT	Position, Velocity and Time
Q	Quadrature Component
QPSK	Quadrature Phase Shift Keying
RF	Radio Frequency
ROC	Receiver Operating Characteristics
RMSE	Root-Mean-Square Error
S/A	Selective Availability
SIS	Signal-In-Space
SNR	Signal-to-Noise Ratio
SoL	Safety-of-Life service
SDR	Software-Defined Radio
U.S.	United States
VORs	VHF omnidirectional radios
WAAS	Wide Area Augmentation System

Chapter 1

Introduction

1.1 Background and Motivation

Navigation is the science of getting a craft or person from one place to another. It can be traced back to a long time ago. Ancient Polynesians used angular measurement of the natural stars to develop their own navigation skills. Chinese compass which can indicate 'magnetic north' was used in Song Dynasty by the military for navigational orienteering by 1040-1044. With the development of radios, new navigation aids were born, they include radio beacons, VHF omnidirectional radios (VORs), long-range radio navigation (LORAN), and OMEGA[1].

In order to achieve the following attributes: global coverage, continuous/all weather operation, ability to serve high-dynamic platforms, and high accuracy[1], the space-based system named Global Positioning System (GPS) was initialized in 1973 by the United States Department of Defense (DoD). The system can satisfy the requirements within an acceptable cost, especially, compared with previous systems like Transit, GPS can supply the global service continuously with high accuracy (as shown in Fig. 1.1) even in high-dynamics. Almost simultaneously, the plan of GLONASS was also launched in Russia. As time is going on, recently, more satellite navigation systems are coming

up, such as European Galileo, Chinese Beidou (or Compass) system and other regional navigation systems that are in the process of developing in Europe, India and Japan.

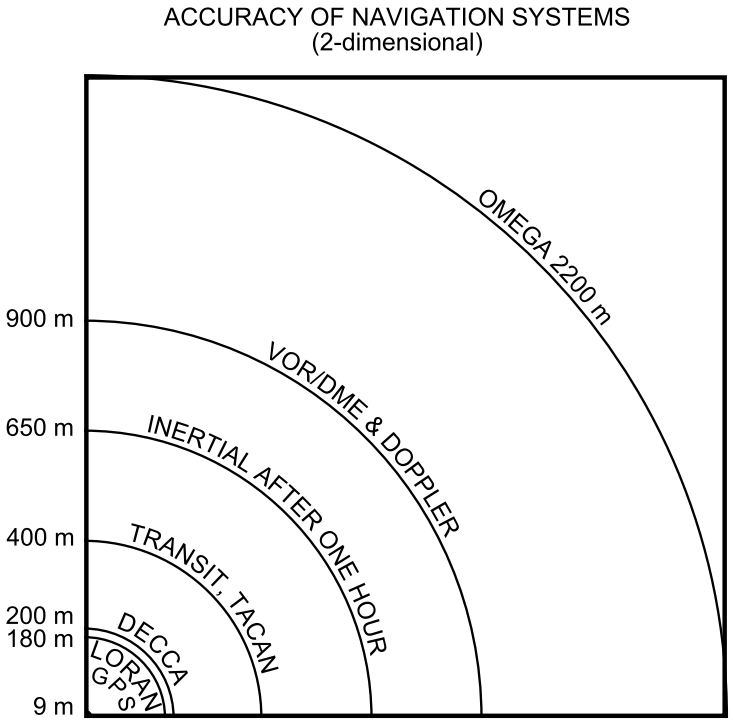

Figure 1.1: Accuracy of different navigation system.

With the development of the signal transmitter (GPS,GLONASS,etc.), the corresponding GNSS (Global Navigation Satellite System)receiver techniques are also developing in a fast manner. On one hand, the size and cost of hardware receiver decrease drastically due to the rapid development of electronic components and advancement in assembly technologies etc. On the other hand, the continuous developments of software-defined radio (SDR) technology result in the appearance of real-time GNSS software receivers at the beginning of this century which not only makes the research itself more easier for a large number of scholars in GNSS community, but also largely increases the signal-processing capability by involving more advanced algorithms. To some extent, potentially it can bring out another new commercial success.

Compared with a traditional GNSS receiver in ASIC platform etc. SDR is more flexible and easier to develop, therefore, it can benefit the researchers

substantially to test new advanced algorithms such as new detection techniques, vector tracking, high-accuracy positioning processing and so on. In this sense, SDR can bridge the gap between the theory study of the complex algorithms and their implementation, therefore, in research centers of both universities and companies, SDR becomes a necessity. As we all know, to develop a navigation receiver does not necessarily require an in-depth theoretical knowledge of signal-estimation and signal detection theory [2]. Many textbooks indeed skip the highly theoretical signal-estimation and signal-detection framework and focus on engineering aspects which causes the disadvantage that the existing navigation signal-processing theory has limits and does not always provide an optimal algorithm for detection or estimation [2]. Hereafter in this thesis, based on the traditional receiver framework, innovative improvements will be proposed and analyzed in the processes of acquisition and tracking. In details, parameters estimation including frequency and phase will be focused in this thesis.

In the following section, some of the previous works related to parameters estimation will be reviewed and their limitations will be also presented.

1.2 Literature Review and Limitations

Generally, especially in a GNSS software receiver, the structure of the system can be simply divided into three parts named as acquisition, tracking and PVT (Position, Velocity, Time)computation as shown in Fig.1.2.

In the frame of a GNSS receiver, the task of acquisition process is to detect the visible satellites and to provide, for each detected satellite, a coarse estimate $\left\langle \hat{f}_d^a, \hat{\tau}^a \right\rangle$ of the Doppler frequency f_d and the code delay τ . Traditionally, $\hat{f}_d$ and $\hat{\tau}$ are picked in a search plane only considering the peak cell without any usage of the other cells [3, 4]. The acquisition process for GNSS application is based on the maximum-likelihood (ML) estimation theory [5]. In theory, in terms of frequency estimate, different frequencies have to be evaluated

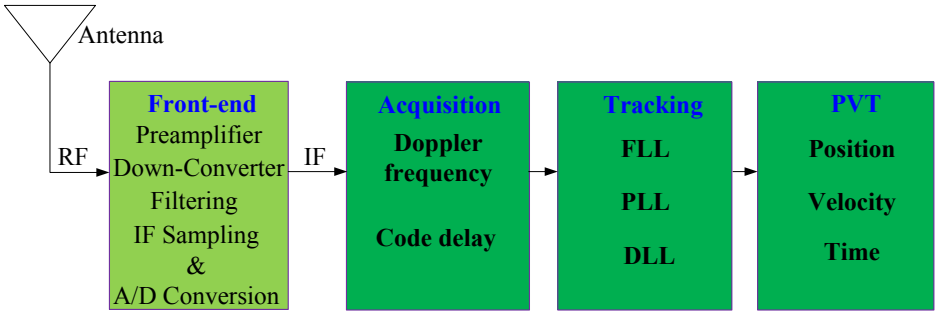

Figure 1.2: The structure of a GNSS receiver.

continuously, but in a real implementation, only discrete frequencies with intervals equal to a searching step f_{sp} can be tested in a certain range , so given that the correct peak cell is detected, the traditional the frequency estimate error is located in the range $[-\frac{f_{sp}}{2}, \frac{f_{sp}}{2}]$. In order to achieve the accuracy requirement for the next tracking loop, frequency estimate has to be refined to an acceptable level, like several Hertz. A system typically used is the Frequency Lock Loop (FLL) mentioned in [1, 6]. A FLL needs additional data and a special structure, which is generally embedded inside the tracking loops. Another typical technique, [3, 7], which exploits the phase relation of consecutive data (p.150 in [3]), also needs additional data, and, at the same time, encompasses an ambiguity problem in the phase measurement, that has to be solved. Actually this technique is essentially similar to an FLL with a particular discriminator. An interpolation method is introduced in [8] to estimate the true value of the Doppler frequency, but it is based on an empirical approximation. In this thesis, a new method will be proposed which can be treated as a single further step with the usage of neighbour cells around the peak cell in the two-dimensional search grid generated in a traditional acquisition process.

Focusing on carrier tracking, a traditional well-designed receiver starts from a FLL stage with a wide-band carrier loop filter to refine the coarse frequency estimate to some acceptable degree, and eventually it moves into a PLL using a bandwidth as narrower as the anticipated dynamics permits. In terms of

FLL discriminator, most of the techniques proposed in the literature always adopted the discriminators listed in [1, 4] which can be commonly accepted as the 'optimal' choices. However, all these discriminators compute the frequency error using the phase difference of the two consecutive data. Here come the main problems, the first one is the presence of data-transition. In [6], both four-quadrant and two-quadrant arctangent discriminators in FLL are analyzed to cope with this problem. Four-quadrant arctangent discriminator is sensitive to data-transition, though two-quadrant arctangent (ATAN) function can solve the problem but it narrows the pull-in range at the same time. The second problem is the pull-in range which can affect the acceptable dynamics, as can be obtained from the Cramer-rao lower bound (CRLB) derived for GNSS case in [9]. The pull-in range is reversely proportional to the length of involved data, therefore a longer period of data results in a narrower pull-in range. Last but not least, the real implementation of ATAN function always involves approximations, and usually a LUT (look-up table) technique has to be used to achieve 'real-time' ATAN function which degrades the accuracy and occupies more memory sources. To avoid aforementioned problems, novel FLL discriminators based on energy can be employed. To author's best knowledge, there is only one available FLL discriminator which is based on energy of the signal as shown in [10] among the related previous literature. However the mathematical expression of the discriminator is complex, it involves approximation and also needs to know the value of signal amplitude and code delay error to compute the exact frequency error. Hence, in this thesis, a new FLL discriminator also based on energy will be proposed which can deal with the shortages involved in [10]. Additionally, the FLL discriminators based on energy can also improve the sensitivity of FLL which is especially beneficial in weak-signal scenarios [11].

Furthermore, in tracking loops, the application of Kalman-filter brings a revolutionary innovation. In conventional digital receiver designs, the tracking loop always consists of a Frequency-Lock-Loop (FLL), a Phase-Lock-Loop

(PLL) and a Delay-Lock-Loop (DLL), but in the Kalman-filter based counterpart, all these lock loops are substituted by one single unit named as Kalman system which will be in charge of estimating all the unknown parameters such as Doppler frequency, carrier phase and code phase etc. in a coupled manner [12]. The different measurements result in two main kinds of Kalman systems, one is Extended-Kalman-filter (EKF) based tracking loop, the other one is linear Kalman-filter-based (KF) tracking loop. In case of EKF, In-phase (I) and Quadrature-phase (Q) outputs of the correlators are used as measurements while on the other hand, the outputs of discriminators are exploited [13]. Literature has demonstrated that KF-based or EKF-based tracking loop outperforms traditional one in multiple aspects. In [14] it is confirmed that KF-based tracking loop outperforms the traditional counterpart in terms of sensitivity and accuracy. In [15] the advantage of EKF-based tracking in terms of positioning accuracy is also presented by using a professional receiver as reference. At the same time, this work has been extended to other important applications such as

- The application in different implementations of GPS/INS integration system: loose, tight, ultra-tight [13]
- The application in weak signal scenarios [16, 17, 18]
- The application in Presence of Ionospheric Scintillations [19]
- Vector tracking [20, 11]

Although the advantage of Kalman filter in GNSS field has been demonstrated in a rich variety of previous papers, the analysis of Kalamn filter itself hasn't got comparable attention. In most cases, the applications just follow the definition of Kalman filter and focus on the performance improvement without giving any deep insight into the Kalman filter itself. Only recently, typical analysis results can be available in [21, 22, 23]. [21, 22] compared KF-based

tracking loop with a traditional one using experimental methodology, while [23] offered more comprehensive and sensible analysis, but it only considered two states in the KF model, and used an approximated observation matrix which can only work well where the integration time is very small (like a few milliseconds) or the frequency error (and frequency rate error) is close to zero; in addition, the values of initial error covariance, process noise covariance and measurement noise covariance are set in an empirical way. Upon these issues, in this thesis, a more strict and accurate analysis will be presented, and furthermore, the relationship between KF-based tracking loop and traditional one can also be found which can facilitate the real implementation of KF-based tracking loop in the frame of current hardware receivers. At the same time, the analysis can give a hint on how to set the loop factor more precisely.

From another different perspective, KF-based or EKF-based tracking loop can be treated as a 'small-scaled' vector tracking (VT) which integrates all the parameters into a single vector. In this sense, the parameters involved are all connected rather than individually estimated. At a higher level, [20, 11] give a detailed description about the concept of vector tracking which combines several different channels into one single vector to improve the overall sensitivity of the system. In this way, one tracking channel can help other channels via the estimated receiver's position, velocity, clock offset, and clock drift. As more satellites become available, VT gains more attention, therefore, this work is also our future research topic.

1.3 Research Objectives

Given the lack of researches as mentioned above, this thesis starts from the fundamentals of GNSS receiver techniques and extends the work more in-depth to derive innovative improvements in terms of parameters estimation. With all these new algorithms, the GNSS receiver system can be enhanced

especially in a software version. At the same time, the whole process of analysis in theory can bring benefit on system design even in traditional hardware receiver. As long as the basic components of the system are understood clearly, the extended work in higher level like integrated navigation system with other different sensors, different implementations of vector tracking, etc. will become much easier. To make the GNSS signal processing techniques more enhanced and integrated, here, in this thesis, the following goals are mainly pursued:

- Analyze and investigate the fundamentals of GNSS receiver techniques utilized traditionally in order to give the brief description and summary of the necessary theory which can help us understand the following content more clearly and easier.

- Refine the frequency estimate in acquisition process in a simple way which can be treated as a single further step based on the previous acquisition process. In theory, the new proposed method also really fulfills the ML estimation process closely.

- Develop a new FLL discriminator based on energy in order to broaden the pull-in range which is beneficial to high-dynamics and low signal-to-noise ratio (SNR) scenarios. With the introduce of pilot components in the newly coming-up modulation, the combination of data component and pilot component is adopted to improve SNR by fully making use of the transmitted power.

- Test the advantage of EKF-based tracking loop in a real scenario in terms of PVT results, two professional receivers are used as reference to evaluate the new technique. Further more, Kalman filter is analyzed in depth which can give an insight into the relationship between KF-based and traditional tracking loop. In this way, the real implementation of KF algorithm in the frame of traditional hardware receivers becomes

possible and easy. At the same time, Kalman tuning is also strengthened to develop more concrete reasonable strategy.

- Introduce the concept of vector tracking in a high level, and explain the key techniques involved.

Generally, most importantly, the ultimate goal is to analyze GNSS receiver techniques in depth, as this is the only way to develop more powerful innovations in this field.

1.4 Thesis Outline

The structure of this thesis is organized as follows:

Chapter 1 first simply gives a brief background and motivation, and then presents the summary of current related available works that have been done, and finally, proposes the central objectives of the research discussed in the thesis.

Chapter 2 mainly covers some specific fundamentals involved in this thesis including GNSS signal structure and signal processing basis. In the first part, a general mathematical expression of the GNSS signal will be given and every term will be discussed separately. In the second part, some basic key theories involved are analyzed at high level rather than in details.

Chapter 3 introduces a fast nearly ML Doppler frequency estimation method in GNSS signal acquisition process, which can be treated as a single further step based on the original acquisition process. First, the whole derivation is given in details. This method mainly exploits the adjacent cells around peak cell in the two-dimensional search space calculated in acquisition process, and a general mathematical expression of the algorithm is given. CRLB and a least-square method are also derived as references to evaluate the performance of the new proposed algorithm. From the comparison results, it

can be concluded that the new algorithm is close to CRLB which means that can be treated as the best estimation algorithm in this circumstance. Finally, other two main non-AWGN nuisances including the peak point's location and the code delay error are discussed, especially, the influence of peak point's location is more strengthened, and the corresponding treatment to counteract the influence is also proposed.

Chapter 4 proposes a new FLL discriminator, different from the traditional FLL discriminators that mainly exploit the phase difference between two consecutive received data to compute the frequency error. The new proposed discriminator is based on energy. First, the derivation of the discriminator is presented in details and the corresponding implementation scheme is also designed. Later, the performance of the new FLL discriminator is evaluated through the comparison with traditional ATAN discriminator and the only available discriminator which is also based on energy. The result shows that the new FLL discriminator inherits the advantages of two aforementioned counterparts but avoids their shortages, and in conclusion, it can be treated as a ML discriminator with the help of lock loop. Thanks to the new structure, it only needs one single period of data and can broaden the pull-in range. Finally, with the introduce of pilot channel in new modulation schemes, a new structure which combines data and pilot channels is employed to improve the estimate accuracy of the new FLL discriminator.

Chapter 5 first introduces the background of the employment of Kalman filter in tracking loop, there are mainly two different types of Kalman systems which are EKF and KF. Later, EKF-based tracking loop is implemented in the frame of a real receiver. The structure of the whole receiver system based on EKF-based tracking loop is described including acquisition, tracking and PVT parts, but differently from traditional structure, new dedicated blocks are added to serve EKF-based structure. In acquisition part, Preparation-For-Tracking (PFT) is added to prepare for the following tracking loop. Its

main function includes the refinement of initial frequency estimate and computation of (carrier-to-noise ratio) CNR, within the EKF-based tracking loop, EST block is dedicated to maintaining the CNR estimate. In PVT part, the simple one-shot least-square method is adopted. With the new designed system, one campaign in a real scenario is fulfilled to evaluate its performance in terms of positioning accuracy, meanwhile, two professional receivers are used as references. Furthermore, KF-based tracking is analyzed in depth. Based on the structure of a KF system, a new control system is derived, from which KF system can be related to the traditional tracking loop, from which the advantage can be easily understood and disclosed. At the same time, the analysis can provide an insight into the real implementation of a KF system in the frame of traditional tracking loop even in hardware without large modification.

Chapter 6 mainly summarize the whole work that has been done in this thesis. At the same time, some recommendations are proposed for future work including vector tracking loop study, implementation of a real-time KF-based tracking loop, the detection of phase jump and integrated navigation system.

Chapter 2

Fundamentals of GNSS receivers

This chapter mainly covers the necessary fundamental knowledge involved in GNSS receiver design which can help us understand the system in depth. In return, with these basic theories, the performance improvement or tech breakthrough in this field becomes possible and promising. First, this chapter starts from the introduction of signal components, and eventually, it brings out the key theories specially beneficial for the subsequent chapters.

2.1 GNSS Signal Structure

A satellite-based navigation system is a special application of a communication system in geometric positioning field. Briefly, for each individual channel, the whole process can be illustrated in Fig.2.1

As shown in Fig.2.1, in order to broadcast the message data (Navigation data in GNSS field), a transmitter has to be used to modify the baseband signal for efficient transmission. It usually consists of the following subsystems [24]:a preemphasizer, a quantizer, a coder, and a modulator. Correspondingly, in order to extract the message from the received signal, the receiver may consist of demodulator, a decoder, a filter and deemphasizer.

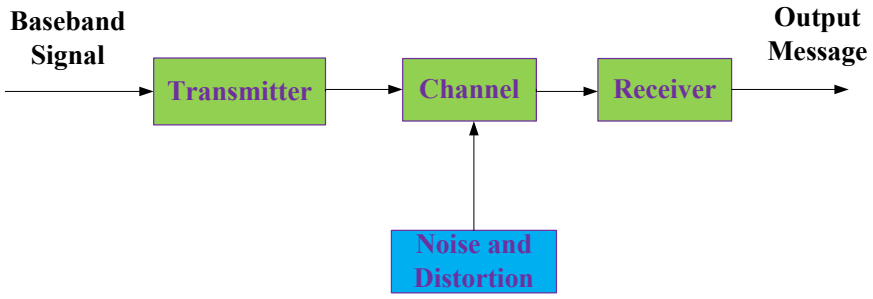

Figure 2.1: The structure of one single channel in GNSS.

Generally, baseband signals are not suitable for direct transmission due to their low frequencies. Therefore, different modulation techniques are introduced to facilitate the transmission. In old days, Binary Phase Shift Keying (BPSK) was adopted in signal modulation, such as GPS, GLONASS. As GNSS develops nowadays, the source of availability of frequency bands becomes limited, and the Binary Offset Carrier (BOC) modulation proposed by Betz J. [25]is commonly used in modern GNSS to minimize the interference between different navigation systems.

In terms of channel identities, two main channel access methods (CAM) are utilized which are Code Division Multiple Access (CDMA) and Frequency Division Multiple Access (FDMA), and as time is going on, CDMA becomes the main trend. Briefly, the main features of the current satellite systems are described Table 2.1

Briefly, we can summarize the modulation adopted in GNSS field as described in Fig.2.2. It is necessary to make it clear that Fig.2.2 just presents the simple description of the modulation, and the details of specific GNSS signal generation can be found in corresponding Interface Control Documents (ICD) [26].

From Fig.2.2, it can be learned that during the whole process, one signal may consists of four components: Pseudo-Random Noise (PRN)code, Navigation data, Sub-carrier, Carrier. Furthermore, sub-carrier is only introduced in case of BOC modulation in modern GNSS such as Galileo, Compass and

Table 2.1: Key Features of Current Main Satellite Navigation Systems

System	**GPS**	**GLONASS**	**Galileo**	**COMPASS**
Country	USA	Russia	European Union	China
Modulation / CAM	BPSK / CDMA	BPSK / FDMA,CDMA	BOC / CDMA	BOC / CDMA
Number of Satellites (Planned)	36	31	30	35
Carriers	-L1=1.57542GHz, -L2=1.22760GHz -L3=1.38105GHz -L4=1.37991GHz -L5=1.17645GHz	-L1,FDMA = 1602 + n × 0.5625 MHz -L2, FDMA =1246 + n × 0.4375 MHz - L1,CDMA=1.5754GHz - L2,CDMA=1.242GHz - L3,CDMA=1.20714GHz - L5,CDMA=1176.45GHz	-E1-L1-E2=1.559-1.592GHz - E6=1.260-1.300GHz -E5=1.164-1.215GHz	-B1=1.561098GHz -B1-2=1.589742GHz -B2=1.20714GHz -B3=1.26852GHz

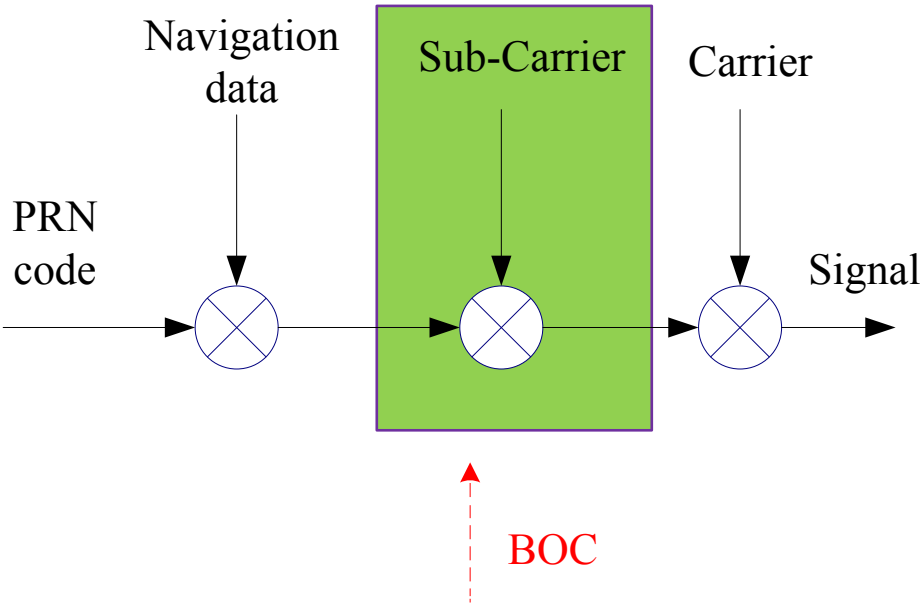

Figure 2.2: The Generation of GNSS signals.

GPS modernization, that is to say, in old BPSK modulation in GPS, the highlighted part in Fig.2.2 can be omitted. So, mathematically, the basic signal y_i can be expressed as

$$y_i(t) = A_i \cdot d_i \cdot c_i \cdot c_{sub,i} \cdot Car_i(2\pi f_{Car} t + \theta) \tag{2.1}$$

where A_i denotes the amplitude of the signal, d_i denotes the navigation data (sometimes it can also stand for secondary code like the pilot component of E1 signal in Galileo), c_i represents the PRN code, $c_{sub,i}$ represents the sub-carrier which is only adopted in BOC modulation ($c_{sub,i} = 1$ when no sub-carrier is involved), Car_i represents the carrier function which is usually Sinusoid function (sin)or Cosine function (cos), f_{Car} is frequency of the carrier, θ means the initial phase of the carrier.

In the following part, we will provide a more detailed introduction of each component.

2.1.1 Navigation data

Navigation data is the goal of a GNSS receiver, only given the data, can positioning result be calculated correctly. Different satellite navigation systems have their own specific definition of navigation message both in structure and contents. Navigation data contains all the parameters needed in positioning service, they are stored in each satellite with a validity duration and broadcasted world-widely. There are mainly four types of parameters for positioning[26]:

- Ephemeris :indicates the position of the satellite to the user receiver
- Time and clock correction parameters: used to compute pseudo-range
- Service parameters: needed to identify the set of navigation data, satellites,and indicate the signal health
- Almanac: needed to indicate the position of all the satellites in the constellation

When comparing two typical different satellite systems, GPS and Galileo, the main difference in terms of navigation data is that data rate has been extended

from 50HZ in GPS to 125Hz in Galileo. In this sense, the broadcasting of navigation message becomes more efficient but the data-transition problem should be more taken care of in Galileo signal processing.

2.1.2 Pseudo-Random Noise (PRN) code

Pseudo-Random Noise (PRN) codes transmitted by satellites are deterministic periodic sequences bearing a close resemblance to a random sequence. Each PRN code is generated using a tapped linear feedback shift register (LFSR)[26]. The most important characteristics that decide its application in CDMA systems are described as follows:

- Spread Spectrum

  PRN is also referred to as spreading code, as literally explained, PRN code can spread the bandwidth of data signal due to its higher chip rate compared with counterpart in data signal. Therefore, once radiated power is fixed, the corresponding flux spectra density is decreased to avoid interference with terrestrial microwave line-of-sight communication and other radio systems[4]. From another different angle, with certain flux density constraints, the wider bandwidth can permit use of higher power level to achieve sufficiently precise ranging accuracy. Furthermore, this spread-spectrum technique is termed as direct-sequence spread spectrum (DSSS).

- Periodic Sequences

  All the PRN codes in GNSS field are periodic. In GPS, the period of C/A code is $T_{C/A} = 1ms$, and in Galileo, the period of E1-B code is extended to 4ms.

- Correlation Characteristics

As mentioned before, the introduce of PRN code can help identifying different channels or satellites due to its following properties (here, C/A code is taken as an example):

1. *Zero Cross Correlation*

All the PRN codes (e.g.,C/A codes) are uncorrelated with each other, that is to say, for C/A code c_i and C/A code c_j, the cross correlation in discrete time can be written as (the length of code is assumed as one single period $T_{C/A}$)

$$R_{i,j}(m) = \frac{1}{L}\sum_{n=0}^{L} c_i(L)c_j(L+m) \approx 0, \quad \text{for all } m. \tag{2.2}$$

where L is the total samples involved, $L = f_s \cdot T_{C/A}$ (f_s is the sampling frequency), m stands for code delay (units: samples)

As presented in Fig.2.3, no matter what value the code delay is, the correlation result of two different PRN codes (here, C/A code no.1 and no.2 are used as examples) is always close to zero.

2.*Auto-Correlation Property*

For all PRN codes, in the calculation of one PRN code's autocorrelation function (ACF), the peak value can only show up in case that they are perfectly aligned with zero time lag as shown in Fig.2.3. Similarly, in discrete time, ACF can be expressed as

$$R(m)_{i,i} = \begin{cases} 1 - |\frac{m}{T_c \cdot f_s}| & \text{if } 0 \leq |m| \leq T_c \cdot f_s \\ \\ 0 \quad \text{Otherwise} \end{cases} \tag{2.3}$$

where T_c is the chip period of C/A code, $T_c = \frac{T_{C/A}}{1023}$.

This property is used to synchronize the local code with the received signal. As it will be shown, in the tracking part,a Phase-Lock loop (PLL)

is dedicated to adjusting the local code to achieve synchronization in terms of code delay.

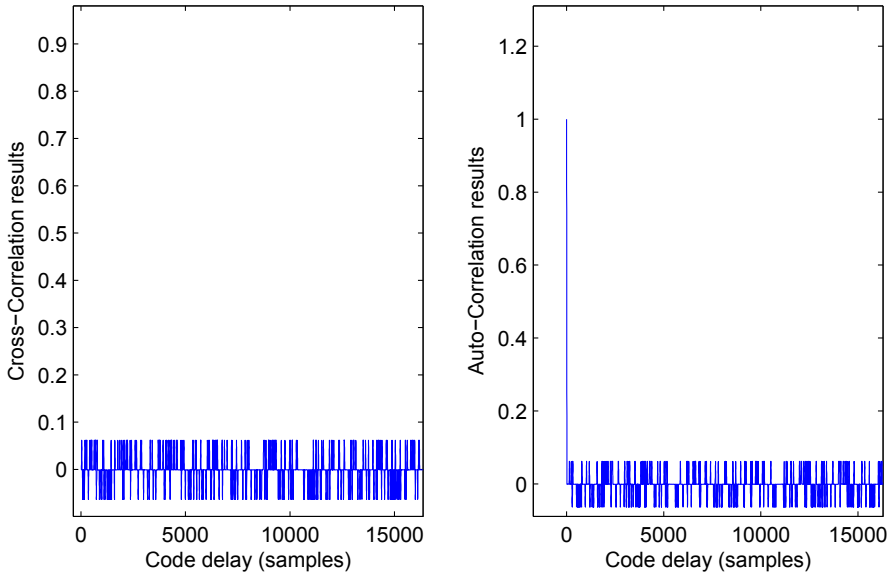

Figure 2.3: The Correlation property of C/A code (sampling frequency f_s=16.3676 MHz).

2.1.3 Carrier and Sub-Carrier

As discussed in 2.1, a data signal, due to its low frequency, can not be directly broadcasted as the size of radiating antenna should be on the order of one-tenth or more of the wavelength of the signal radiated [24]. In this sense, direct broadcasting of data signal would necessitate a dramatically large antenna which is impractical. Thus, carrier is modulated to increase the central frequency of signal to facilitate the radiation. The values of different carrier frequencies are shown in Table.2.1. To save frequency band several different satellite systems actually share some common central frequencies, for example, L1 signal (GPS) and E1 signal (Galileo) have the same carrier frequency which is 1.57542GHz. Since this will cause the increased interference between these signals, in new GNSS design (e.g., Galileo, Compass), the concept of

Sub-carrier is proposed which can split or shift the previous main lobe of the spectrum.

The first choice of sub-carrier is equal to the sign of a sine or a cosine waveform as expressed in (2.4) mathematically, this choice produces a symmetrical split spectrum with two main lobes shifted from the carrier frequency by the amount equal to the subcarrier frequency f_{sub} as shown in Fig.2.4. This technique is termed as BOC modulation [25].

$$S(t) = sign[\sin(2\pi f_{sub} t)] \tag{2.4}$$

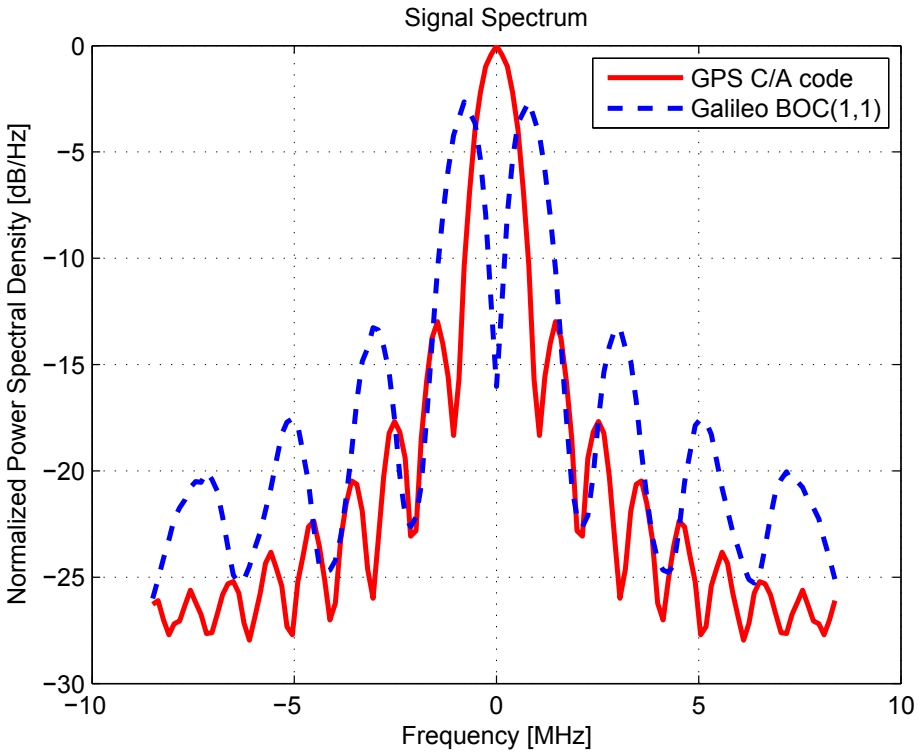

Figure 2.4: Difference in PSD between BPSK and BOC modulation.

BOC modulations depends on two independent design parameters :

- Subcarrier frequency f_{sub}
- Spreading code rate f_{code}

The signal with BOC modulation is usually noted as BOC(m,n),the parameter m stands for the ratio between f_{sub} and a reference frequency f_0 ($f_0 = 1.023MHz$) and n stands for the ratio between f_{code} and f_0. For instance, BOC(1, 1) means a 1.023MHz subcarrier frequency and a 1.023MHz code rate.

Different from BOC modulation, another conceptually similar option is Alternative BOC (AltBOC) modulation which introduces a complex sub-carrier so that the spectrum is not split up, as is the case of BOC, but simply shifted to higher or lower frequencies. It is more complicated than BOC. Here for simplicity, it won't be analyzed in depth, and more details can be found in [25].

2.2 Signal Processing Operations

This section mainly introduces the fundamentals of signal processing techniques involved in the GNSS receiver field, to facilitate the understanding of GNSS systems in depth and especially the subsequent chapters. There are mainly four parts that will be analyzed individually: Frequency-domain Analysis, Noise model, Kalman filter, Control system.

2.2.1 Frequency-domain Analysis

In signal processing, control systems engineering, etc., the frequency domain analysis refers to the analysis of systems or signals with respect to frequency, rather than time. Put simply, a time-domain graph shows how a signal changes over time, whereas a frequency-domain graph shows how much of the signal lies within each given frequency band over a range of frequencies. There are mainly three different mathematical transforms employed in frequency analysis as follows:

- Fourier transform

- Laplace transform (S transform)
- Z transform

These three transform methods are similar but they are applied in different contexts. In the remainder of this section, the evolution of Fourier transform will be focused first, and later, S transform and Z transform will be briefly introduced on the basis of the Fourier transform.

The development of Fourier analysis has a long history involving many individuals and the investigation of many physical phenomena. For instance, Babylonians first proposed the concept of 'trigonometric sums' to describe periodic phenomena, and eventually, more notable scientists were involved in this topic. Finally, the theory of Fourier series was broadly accepted by eminent scientists due to the contribution of Fourier and other related scientists and mathematicians, at the same time, Fourier extended his research work from Fourier series to Fourier transform which is still the powerful tool for the analysis of Linear Time-Invariant (LTI) systems [27].

1.Fourier series (for periodic signal)

The evolution of Fourier transform can be introduced starting from Fourier series, given a periodic continuous-time signal $x(t)$ with period T, its Fourier series representation can be expressed as:

$$x(t) = \sum_{k=-\infty}^{+\infty} a_k e^{jkw_0 t} = \sum_{k=-\infty}^{+\infty} a_k e^{jk(2\pi/T)t}, \tag{2.5}$$

where

$$a_k = \frac{1}{T}\int_T x(t)e^{-jkw_0 t}dt = \frac{1}{T}\int_T x(t)e^{-jk(2\pi/T)t}dt$$

The set of coefficients a_k are *Fourier series coefficients* of $x(t)$. These coefficients measure the portion of the signal $x(t)$ that is at each harmonic of the fundamental component (at fundamental frequency w_0).

Similarly, when it comes to discrete-time counterpart, suppose $x[n]$ is a periodic sequence with period N, the mathematically expression of its Fourier

series pair is :

$$x[n] = \sum_{k=<N>} a_k e^{jkw_0 n} = \sum_{k=<N>} a_k e^{jk(2\pi/N)n}, \tag{2.6}$$

where

$$a_k = \frac{1}{N} \sum_{k=<N>} x[n] e^{-jkw_0 n} = \frac{1}{N} \sum_{k=<N>} x[n] e^{-jk(2\pi/N)n}$$

where, $k =< N >$ means parameter k can vary over a range of N successive integers. e.g. $k = 0,1,...,N-1$ or $k = 5,6,7...,N+4$.

2.Fourier transform (for aperiodic signal)

Based on the Fourier series concept, in case of aperiodic signal, the mathematical expression of Fourier transform can be derived [27]. Given a aperiodic continuous signal $x(t)$, the Fourier transform pair can be written as:

$$x(t) = \frac{1}{2\pi} \int_{-\infty}^{+\infty} X(jw) e^{jwt} dw \tag{2.7}$$

where

$$X(jw) = \int_{-\infty}^{+\infty} x(t) e^{-jwt} dt$$

$X(jw)$ is termed as the *Fourier Transform* of $x(t)$.

Similarly, in case of discrete aperiodic signal $x(n)$, the Fourier transform pair can be written as:

$$x[n] = \frac{1}{2\pi} \int_{2\pi} X(jw) e^{jwn} dw \tag{2.8}$$

where

$$X(jw) = \sum_{n=-\infty}^{+\infty} x[n] e^{-jwn}$$

3.Discrete Fourier Transform (DFT)

As the digital technique develops, in real implementation, the signal processing is intended to be accomplished in a digital computer or digital hardware

rather than analogy circuits. In this sense, a continuous signal is always sampled and converted to discrete samples by A/D converter. Therefore, the Fourier analysis of discrete-time sequences becomes the focus in the field of practical frequency analysis of a signal. Eventually a technique termed as *DFT* for finite-duration signals emerged. The definition is as follows:

Given a signal of finite duration $x[n]$, suppose $x[n] = 0$ when outside the interval $0 \leq n \leq N_L - 1$, assume $N \geq N_L$, then DFT can be written mathematically as:

$$\tilde{X}[k] = \frac{1}{N} \sum_{n=0}^{N-1} x[n] e^{-jk(2\pi/N)n}, \quad k = 0,1,...,N-1 \tag{2.9}$$

and the original finite duration signal can be recovered from its DFT as:

$$x[n] = \sum_{k=0}^{N-1} \tilde{X}[k] e^{jk(2\pi/N)n}, \quad n = 0,1,...,N-1 \tag{2.10}$$

Practically,the fast Fourier transform (FFT) algorithm is employed for the calculation of DFT. Based on (2.9), we can rewrite it as

$$\tilde{X}[k] = \frac{1}{N} \sum_{n=0}^{N-1} x[n] e^{-jk(2\pi/N \cdot T_s)nT_s}, \quad k = 0,1,...,N-1 \tag{2.11}$$

where T_s is *sampling period*.

comparing (2.11) with (2.8), we can find actually that DFT corresponds to the samples of $X(e^{jw})$ taken with an interval $2\pi/T$ (T is the time length of signal $x[n]$). This also explains the physical meaning of DFT in practical computation.

4.S and Z transforms

As discussed before, Fourier transform can provide us with a representation for signals as linear combinations of complex exponentials of the form e^x with $x = jw$. In order to represent a broader class of signals, Laplace transform and Z transform are developed separately in continuous time and discrete time.

The definition of S transform is:

$$X(s) = \int_{-\infty}^{+\infty} x(t)e^{-st}dt \tag{2.12}$$

where s can be expressed as

$$s = \sigma + jw. \tag{2.13}$$

The definition of Z transform is:

$$X(z) = \sum_{n=-\infty}^{n=+\infty} x[n]z^{-n} \tag{2.14}$$

where z can be expressed as

$$z = re^{jw}. \tag{2.15}$$

(2.13) and (2.15) can provide an insight into the relationship between S transform ,Z transform and Fourier transform, which can help understanding S and Z transforms more in depth. After all, S and Z transforms rather than pure Fourier transform are the common tools for system analysis.

2.2.2 Kalman Filter

A Kalman filter is simply an optimal recursive data processing algorithm, which operates recursively on streams of noisy input data to produce a statistically optimal estimate of the underlying system state [28]. Here is only provided, a brief overview of this optimal estimator, key characteristics will be summarized to disclose the secret of Kalman systems.

Fist, the general mathematical expression of the system can be written as:

$$\begin{cases} \text{System model :} & X_k = A_k \cdot X_{k-1} + B_k \cdot U_{k-1} + W_k \\ \text{Measurememnt model :} & Z_k = H_k \cdot X_k + V_k \end{cases} \tag{2.16}$$

where

X_k is the state transition matrix.

B_k is the control-input matrix.

W_k is the process noise, and its covariance matrix is

$$E[W_k W_k^T] = Q_k \tag{2.17}$$

H_k is the observation matrix.

V_k is observation noise, and its covariance matrix is

$$E[W_k W_k^T] = R_k \tag{2.18}$$

and the whole structure of the system is illustrated in Fig.2.5 from which, it is shown that the system mainly includes two steps: Time update and measurement update.

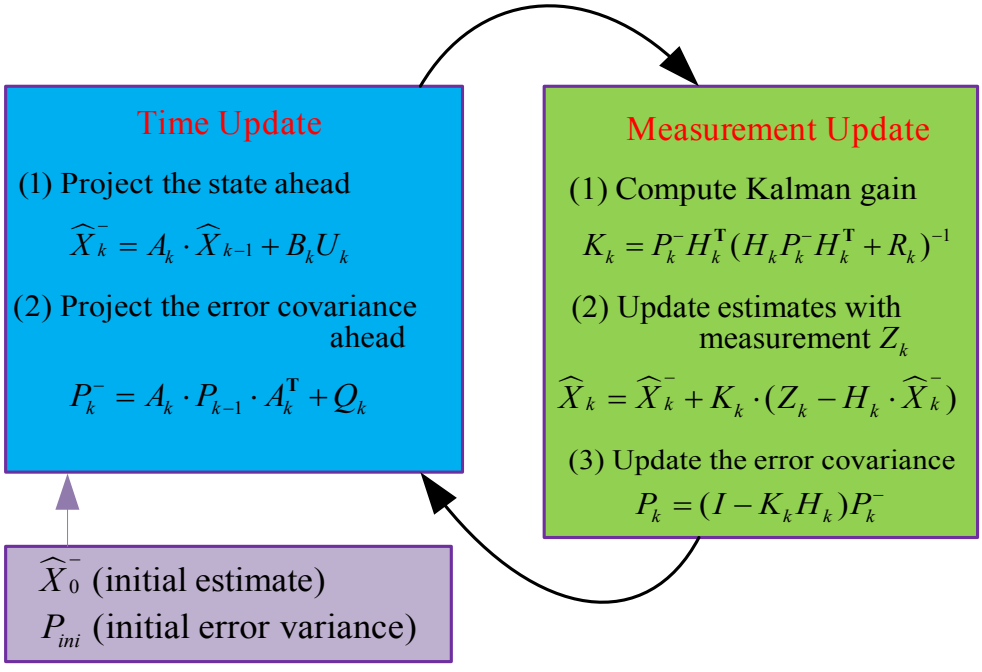

Figure 2.5: The structure of a Kalman system.

In addition, the detailed derivation of Kalman filter is presented in [29] where we can find that the key heart of the algorithm is an application of least-square

method (The derivation of Kalman gain K_k shown in Fig.2.5 is based on the least-square method)in a matrix system. Therefore, it is very important to point out the first key characteristic:

1. The error terms and measurements in the system are not necessarily Gaussian distributed, Kalman's original motivation is to minimize the covariance of estimations without any assumption in noise models.

But, in real applications, such as guidance, navigation and control of vehicles, Additive white Gaussian noise (AWGN) model is always adopted due to its tractability property. The use of AWGN model can make the system much more easier to be analyzed in mathematics with certain degree of accuracy [29], and furthermore, under the AWGN hypothesis, the estimate result of KF is unbiased. In the following part, the AWGN model is introduced.

AWGN is a channel model in which the only impairment to communication is a linear addition of white noise with a constant spectral density (PSD : $\frac{N_0}{2}$ W/Hz, two-sided.) and a zero-mean Gaussian distribution of amplitude.

Zero-mean Gaussian distribution:

Suppose that parameter X conforms to zero-mean Gaussian distribution, then it is noted as:

$$X \sim N(0,\sigma^2) \tag{2.19}$$

where σ^2 means the variance of X, and probability density function can be written as:

$$f(x) = \frac{1}{\sqrt{2\pi}\sigma} \exp[-\frac{1}{2\sigma^2}x^2] \tag{2.20}$$

In presence of noise, the received signal given in (2.1)can be expressed as

$$y_i(t) = A_i \cdot d_i \cdot c_i \cdot c_{sub,i} \cdot Car_i(2\pi f_{Car}t + \theta) + n_{IF}(t) \tag{2.21}$$

In addition, according to Nyquist theorem [27], the sampling frequency in front-end is set as

$$f_s = 2B_{IF} \tag{2.22}$$

where B_{IF} is the bandwidth of the front-end filter as shown in Fig.2.6, therefore, the variance of noise is :

$$\sigma^2 = N_0 \cdot B_{IF} = N_0 \cdot \frac{f_S}{2} \tag{2.23}$$

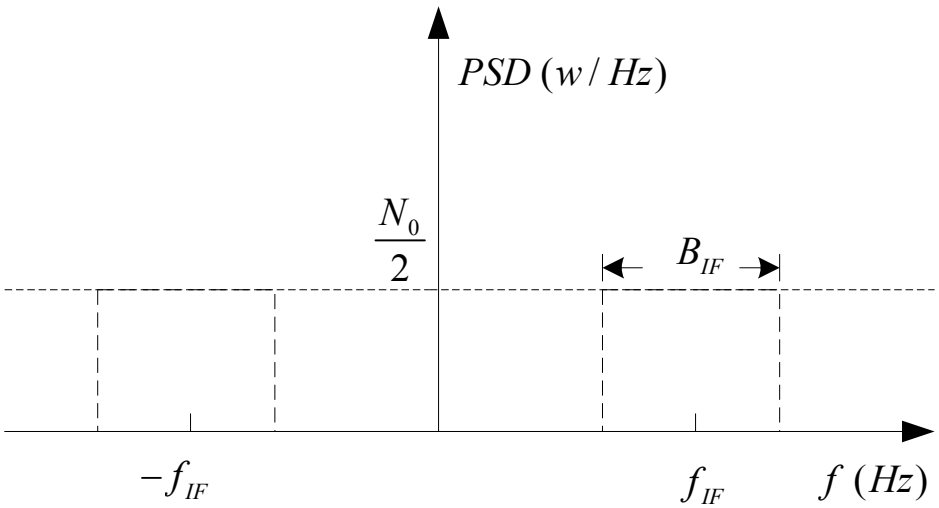

Figure 2.6: WGN Noise model.

From the mathematical equations of KF system (2.16), we can conclude the second characteristic:

2. Kalman filter system is a linear system.

This is a restriction of KF system. As shown in (2.16), both system model and measurement model are linear, but practically, the application of KF can be extended to non-linear cases with the technique termed as Extended Kalman filter (EKF) in which Taylor series theory is employed for a non-linear system to approach an approximate linear system.

Above all, another significant characteristic is the third property:

3. The propagation of error covariance P_k as shown in Fig.2.5.

This is a very important factor to decide the optimality of a KF system, since the value of P_k, Q_k and R_k can decide the weight of faith in measurements. Put simply, as R_k increases, the system will trust the value of measurement

more. As illustrated in Fig.2.5, at the beginning, a relatively big P_k is initially set, which means the faith probability of initial system states' values is very low, eventually, P_k will become smaller, especially, in stead-state, Q_k and R_k will dominate the system performance while P_k depends on Q_k and R_k to some degree at that period. Briefly, KF can be treated as a 'self-adaptive' filter.

Last but not least, another aspect of its optimality is the estimation process which will be explained as characteristic 4.

4. A Kalman filter incorporates all information that can be provided to it. It processes all available measurements, regardless Of their precision, to estimate the current value of the variables of interest [28], the information used in KF system can be summarized as:

- The information of system and measurement models which link the parameters of interest.
- The statistical description of the system noises, measurement noises.
- initial conditions of the variables of interest.

KF process estimates all the variables in a 'coupled' manner and this methodology can be extended to vector tracking techniques to improve the overall performance of a system.

2.2.3 Control Theory

In engineering and mathematics, control theory mainly deals with the behaviour of dynamical systems. In order to make a system work in a reference routine, a controller can manipulate the feedback to obtain the desired effect on the output of the system. Furthermore, rapid advances in digital system technologies help facilitating the implementation of complicated and advanced control systems.

In the field of GNSS applications, control systems are also very important due to its wide employment, such as in the tracking loop design which is a key part in GNSS receivers. Hereafter, for simplicity, Phase-Lock-Loop is mainly considered as a typical example. The model of PLL in S-domain can be illustrated as Fig.2.7.

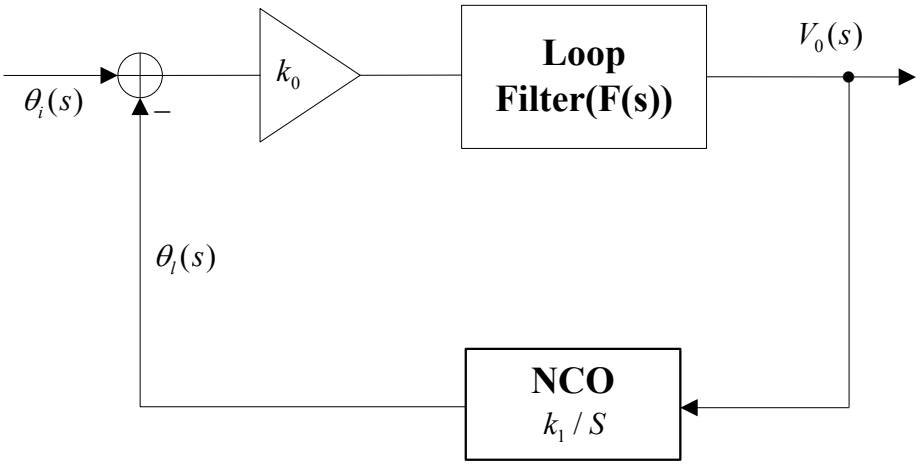

Figure 2.7: Control model of PLL.

The ***transfer function*** of the loop can be written as

$$H(s) = \frac{\theta_l(s)}{\theta_i(s)} = \frac{k_0 k_1 F(s)}{S + k_0 k_1 F(s)} \tag{2.24}$$

In addition, in complicated cases, Mason's rule can be adopted to write the transfer function in a simple way.

As presented in Fig.2.7, in order to track the input variable $\theta_i(s)$, the difference between the input variable and local reference $\theta_l(s)$ will be first computed, the error will go through the loop filter in order to decrease the noise influence (**Here, it is important to notice that strictly, 'loop filter'** $F(s)$ **is not a true filter defined traditionally, it is just one 'separate' part in one control loop**), then the output of loop filter $V_0(s)$ will be used to adjust local numerically-controlled-oscillator (NCO) to generate a new local reference as the feedback. So, the system works in a closed loop cyclically.

In the following part, only some points of a control system will be discussed briefly.

1. Stability

Give a system described by (2.24), first ***stability*** should be considered to judge if a system is suitable or not. Basically, as shown in Fig.2.8 the poles of the loop transfer function can decide the stability of the corresponding system. If poles ($S_{pole} = \sigma + jw$) are all located in left-plan, the system is stable, otherwise, not.

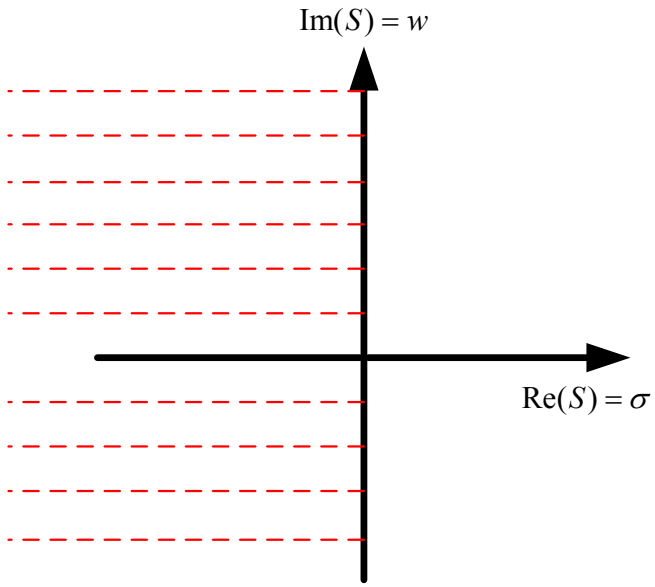

Figure 2.8: The stability of a control system.

Practically, there are several method for stability judgement:

1.Routh Hurwitz criterion

2.Calculation of exact locations of roots

- root locus technique
- Nyquist criterion
- Bode plot

3.Simulation (only general procedures for nonlinear systems)

Particulary, in terms of loop filter design, root locus technique and Bode plot can be used as tools to get thorough analysis results [16].

2. The order of the system

The choice of a control system's order depends on the specific applications. Here in a PLL the phase input can be written as:

$$H(s) = \frac{\theta_l(s)}{\theta_i(s)} = \frac{k_0 k_1 F(s)}{S + k_0 k_1 F(s)} \tag{2.25}$$

from which, it can be concluded that the order of the system depends on the selection of $F(S)$. In terms of $F(S)$ design, there are mainly three methods[16]:

- 1.The transformation from the analog domain
- 2.Controlled-root method
- 3.Minimization of a specific cost function

Traditionally, option 3 as used in [30] is commonly adopted, in real implementation design, option 2 can also be employed to improve the model accuracy which can solve the potential problems involved in option 3 such as BT problem [31].

In PLL applications the phase input is usually modeled in the form

$$\theta(t) = (a + bt + ct^2 + ...)u(t) \tag{2.26}$$

Therefore, based on (2.25) and (2.26), if the highest order of PLL is n, then the PLL can track n terms of (2.26) with zero steady-state phase error.

3. Transformation from S domain to Z domain

In our real implementation, especially in digital system designs, Z transform is crucial, as it can give a direct indication on concrete details of the system implementation. Given the mathematical model of a system in S domain,

Z-transformation has to be employed to get the approximately equivalent counterpart in discrete time.

There are three transformation methods as shown in Fig.2.9:

- Forward difference: $s \rightarrow \frac{Z-1}{T}$
- Backward difference: $s \rightarrow \frac{Z-1}{TZ}$
- Trapezoidal Approximation: $s \rightarrow \frac{2}{T}\frac{Z-1}{Z+1}$

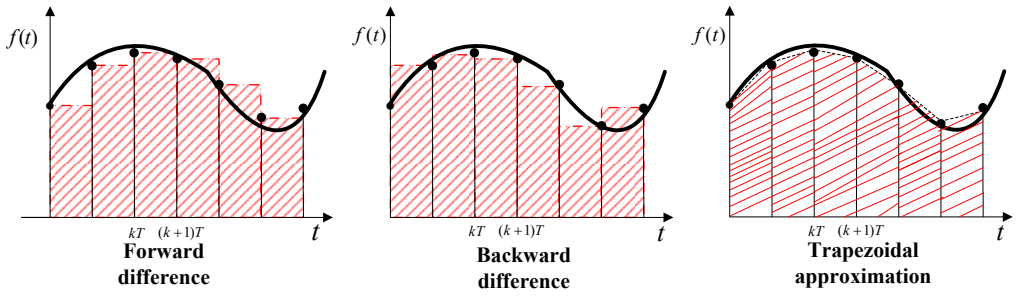

Figure 2.9: Three types of Z-transformation methods.

and the corresponding mapping of the stability region between the S plane and the Z Plane is shown in Fig.2.10

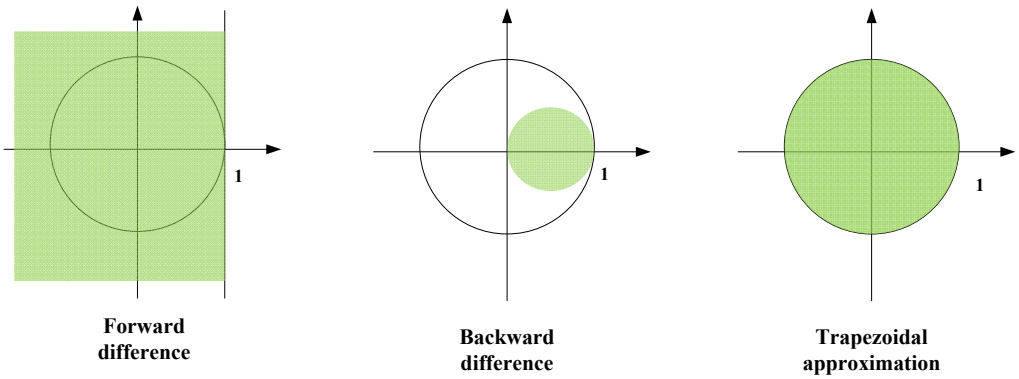

Figure 2.10: Mapping of the stability region between the S plane and the Z Plane.

The choice of transformation method depends on different applications, usually, trapezoidal approximation is employed, but the other two options can

be adopted in analysis of some specific systems, such as the Kalman system which we will discuss in Section 5.

Chapter 3

Fast Nearly ML Estimation of Doppler Frequency in GNSS Signal Acquisition Process

3.1 Introduction

The main purpose of the acquisition and tracking systems of a GNSS receiver is to provide an estimate of the Doppler frequency f_d, the code delay τ, and the phase of the carrier, ϕ, of the signal transmitted by each visible satellite. The task of the acquisition system is to detect the visible satellites and to provide, for each detected satellite, a coarse estimate $\left\langle \hat{f}_d^a, \hat{\tau}^a \right\rangle$ of f_d and τ. This parameter vector is then passed to the tracking systems, whose task is to refine this estimate. The refinement of Doppler frequency estimate is generally performed by a classic phase lock loop (PLL), which requires an initial estimate much more accurate than the one provided by the acquisition system. Therefore it is necessary to improve the accuracy of the estimate $\hat{f}_d^a$ to an acceptable level before starting the operations of the phase tracking loop. A system typically adopted by a GNSS receiver to reach this goal is a frequency lock loop (FLL) which is generally integrated within a PLL. The

first refinement is done by a robust FLL operating at wideband, then the loop bandwidth is gradually reduced and finally the system switches to a PLL scheme [1, 6]. Other methods [3, 7] refine the frequency estimate by exploiting the phase difference between two successive periods of data. An interpolation method is introduced in [8] to estimate the true value of the Doppler frequency, but it is based on an empirical approximation.

In most of the previous methods, usually the estimates of f_d and τ are picked in a search plane only considering the peak cell without any usage of the other cells. In the fields of communications, audio, medical, instrumentation, and others [32], the problem of estimating the frequency of a tone contaminated with noise is tackled for example by Quinn [33, 34], MacLeod [35, 36], and Jacobsen [32, 37], by exploiting the idea of refining the final frequency estimate using the peak sample and two neighbors of the discrete Fourier components. At the same time there are other methods, studied in [38, 39], which utilize the phase information. These methods cannot be directly applied to the acquisition of a GNSS signal, because of the very low signal-to-noise ratio and the different signal model, but they can inspire us to do some innovation in GNSS frequency estimation.

In this chapter, the peak and neighbor points of the cross-ambiguity function (CAF) in the frequency domain are used to derive a simple formula that greatly improves the accuracy of the frequency estimate provided by the acquisition system. The CAF was initially derived in [4] using statistical principles, then [40] presented a new approach of the CAF derivation. Furthermore in this chapter the approximation in CAF main lobe is analyzed in details, based on this approximation, and a new family of methods for refining the estimate of the Doppler frequency is proposed, which exploits the cells close to the peak in the search plane. Compared to the traditional methods, these methods significantly improve the accuracy without increasing the computation complexity or using additional received data.

A preliminary version of this work was presented in [41]. With respect to

that previous work, here we extend and complete all the mathematical derivations, extend the performance analysis with appropriate comparisons, derive and discuss the Cramer-Rao lower bound (CRLB) for the frequency estimator showing that the proposed approach is close to the CRLB (quasi-ML approach), and include the theoretical analysis of other non-AWGN nuisances.

This chapter is organized as follows. In Section 3.2 the signal model is presented and the approximate mathematical expression of the CAF in the main lobe is obtained. In Section 3.3 a new family of algorithms is derived and proved to work perfectly in the absence of noise. In Section 3.4 the performance of the proposed algorithms is investigated in the presence of additive noise; both the CRLB and a least-square (LS) solution are derived as benchmark, and the comparison shows that the new algorithms can approach very closely the CRLB. Besides that, a simple averaging approach based on non-coherent sums is proposed to improve the accuracy of the algorithms in low SNR conditions. Furthermore, in Section 3.5, the effects of other nuisances, uncorrelated with the additive noise, are analysed, and some countermeasures are proposed. Finally, in Section 3.6 the conclusion is drawn.

3.2 Fundamentals of the new algorithms

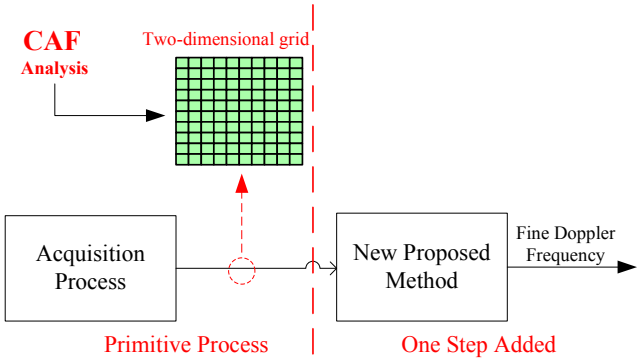

Figure 3.1: Brief structure of new Doppler frequency refinement process.

The basic scheme of the acquisition method proposed in this chapter is illustrated in Figure 3.1. The left part of the figure indicates the traditional GNSS acquisition process from which a two-dimensional search grid (marked in green color) is generally obtained, while the right side shows the presence of a new additional block able to refine the Doppler frequency estimate in a simple way. The innovation proposed in this chapter refers to the algorithms used by this additional block to refine the frequency estimate.

3.2.1 Acquisition process

The acquisition system for GNSS application is based on the maximum-likelihood estimation theory which can be briefly described as follows [42].

The incoming sampled signal can be denoted as a vector

$$\mathbf{y} = [y(0)\ y(1) \cdots y(L-1)] \tag{3.1}$$

where L is the total number of the samples, and

$$y(n) = r(n) + W(n) \tag{3.2}$$

where $r(n)$ is a signal which contains a vector of unknown parameters $\mathbf{a} = [\alpha_1\ \alpha_2\ \alpha_3 \cdots \alpha_K]$, $W(n)$ is a zero-mean White Gaussian Noise (WGN) random process with variance σ^2, and $0 \leq n \leq L-1$.

The ML estimate of the parameter vector $\mathbf{a}$ can be found by maximizing the likelihood function, which depends on the probability density function (PDF), that is

$$\begin{aligned} p(\mathbf{y};\overline{\mathbf{a}}) &= \frac{1}{(2\pi\sigma^2)^{\frac{L}{2}}} \exp\left[-\frac{1}{2\sigma^2}\sum_{n=0}^{L-1}\left(y(n)-\overline{r}(n)\right)^2\right] \\ &= \frac{1}{(2\pi\sigma^2)^{\frac{L}{2}}} \exp\left[-\frac{1}{2\sigma^2}\sum_{n=0}^{L-1}\left(y^2(n)+\overline{r}^2(n)\right)+\frac{1}{2\sigma^2}\sum_{n=0}^{L-1}y(n)\overline{r}(n)\right] \end{aligned} \tag{3.3}$$

where the test signal $\overline{r}(n)$ has the same structure of $r(n)$, but the unknown parameter vector $\mathbf{a}$ is substituted by a vector $\overline{\mathbf{a}}$, whose elements are variables

defined in a range $ran_{\mathbf{a}}$ that contains all the possible values of the unknown vector $\mathbf{a}$, that is to say, $\overline{\mathbf{a}} \in ran_{\mathbf{a}}$.

If the energy of the test signal $\overline{r}(n)$ (that is the term $\sum_{n=0}^{L-1} \overline{r}^2(n)$ in (3.3)) does not depend on $\overline{\mathbf{a}}$, then it is possible to show, [42] that the corresponding ML estimate $\widehat{\mathbf{a}}_{ML}$ of $\mathbf{a}$ is

$$\widehat{\mathbf{a}}_{ML} = \arg \max_{\overline{\mathbf{a}} \in ran_{\mathbf{a}}} \sum_{n=0}^{L-1} y(n)\overline{r}(n) \tag{3.4}$$

So, in this case, the ML estimation actually depends on the scalar product $R(\overline{a})$ between the test signal and the received signal, defined as

$$R(\overline{a}) = \sum_{n=0}^{L-1} y(n)\overline{r}(n) \tag{3.5}$$

$\widehat{\mathbf{a}}_{ML}$ can be found by searching the maximum $R(\overline{a})$ in the range $ran_{\mathbf{a}}$.

In GNSS field, without considering the influence of noise, the received signal, after down-conversion and sampling, can be written as [1]

$$y\left(nT_s\right) = \sum_{m=1}^{N_v} y_m(nT_s) \tag{3.6}$$

where N_v is the number of satellites in view, and

$$y_m(nT_s) = A_m C_m(nT_s - \tau_m) d_m(nT_s - \tau_m) \cos(2\pi(f_{IF} + f_{d,m})nT_s + \varphi_m) \tag{3.7}$$

where A_m is the amplitude of the signal, $C_m(nT_s - \tau_m) = c_m(nT_s - \tau_m)s_b(nT_s - \tau_m)$ is the product of the satellite spreading code $c_m(nT_s - \tau_m)$ and subcarrier $s_b(nT_s - \tau_m)$ used in the new GNSS systems [26], such as in Galileo (if no subcarrier is present, then $s_b(nT_s - \tau_m)$=1), τ_m is the code delay, $d_m(nT_s - \tau_m)$ is the navigation data, f_{IF} is the intermediate frequency, $f_{d,m}$ is the Doppler frequency shift, φ_m is the phase of the carrier, and T_s is the sampling interval (the inverse of the sampling frequency f_s).

From (3.7), we can learn that in principle, the satellite signal actually contains four unknown parameters: code delay (τ), Doppler frequency (f_d), carrier

phase (φ) and data bit. However in the acquisition process, only two of them are estimated, which are τ and f_d.

With respect to the parameter data bit, in the implementation, a noncoherent acquisition scheme is used to solve the problem, so here we assume that there is no data-transition in the accumulation period.

Considering the parameter carrier phase, its influence can be removed by involving two components in the acquisition process which are Inphase component (I) and 90^0 phase-shifted Quadphase (Q) component [43]. Therefore, the test signal $\overline{r}(n)$ can be written as

$$\overline{r}(n) = C(nT_s - \overline{\tau})e^{2\pi(f_{IF}+\overline{f}_d)nT_s} \tag{3.8}$$

where the parameter vector becomes $\overline{\mathbf{a}} = \left[\overline{\tau},\overline{f}_d\right]$, and the energy of $\overline{r}(n)$ is not related to $\overline{\mathbf{a}}$. So the accumulation process in acquisition can be expressed mathematically as

$$R(\overline{\tau},\overline{f}_d) = \frac{1}{L}\sum_{n=0}^{L-1} y(n)C(nT_s - \overline{\tau})e^{2\pi(f_{IF}+\overline{f}_d)nT_s} \tag{3.9}$$

Equation (3.9) is known as cross-ambiguity function (CAF). Based on (3.4) (3.5), the ML estimate of $[\tau,f_d]$ can be obtained [42], as

$$\widehat{\mathbf{a}}_{ML} = \arg\max_{ran_{\mathbf{a}}} \left|R(\overline{\tau},\overline{f}_d)\right| \tag{3.10}$$

where $|\cdot|$ means the modulus of a complex value, and the range of $\overline{\mathbf{a}}$, $ran_{\mathbf{a}}$ will be discussed in Section 3.3.

There are mainly three acquisition schemes [43]: Serial search acquisition, parallel frequency space search acquisition and parallel code phase search acquisition. No matter what kind of scheme is used, a two-dimensional search grid (Figure 3.4) is always obtained, and the resulting estimated vector is selected as the location of the peak cell, and, at the same time, the other cells in the search grid are abandoned. However because of the large frequency searching step f_{sp}, the frequency estimate error is located in the range $[-\frac{f_{sp}}{2},\frac{f_{sp}}{2}]$,

so the initial Doppler frequency estimate is usually not accurate enough to pass to the tracking loop directly.

In order to refine the Doppler frequency estimate, a system typically used is the Frequency Lock Loop (FLL) mentioned in [1, 6]. An FLL needs additional data and a special structure, which is generally embedded inside the tracking loops. Another typical technique, [3, 7], which exploits the phase relation of consecutive data (p.150 in [3]), also needs additional data, and, at the same time, encompasses an ambiguity problem in the phase measurement, that has to be solved. Actually this technique is essentially similar to an FLL with a particular discriminator.

In this chapter, we develop new methods to refine the Doppler frequency estimate, based only on the search grid already evaluated by the acquisition, that is, we do not have to compute new correlations, but we only use the neighbor cells of the CAF peak, already available in the search grid.

3.2.2 Analytical expression of the CAF

The CAF [40] is used in radar, sonar and other similar systems to estimate the time delay and the Doppler shift of an incoming signal. An accurate estimation of these signal parameters generally requires the evaluation of several CAF samples, at the cost of an increased computational complexity. In this chapter we propose a family of methods which exploits the knowledge of an approximate expression of the analytical formula of the CAF, given in [40], to reach a trade-off between accuracy and complexity.

Following the approach presented in [40], the CAF associated to the generic i-th satellite code, locally generated for each trial value of code delay $\overline{\tau}$ and Doppler frequency $\overline{f}_d$, can be written as

$$S_i(\overline{\tau},\overline{f}_d) = \sum_{m=1}^{N_v} R_{m,i}(\overline{\tau},\overline{f}_d) \tag{3.11}$$

where $R_{m,i}(\overline{\tau},\overline{f}_d)$ is the contribution to the CAF of the m-th signal $y_m(nT_s)$. Its analytical expression is [40]

$$\begin{aligned} R_{m,i}(\overline{\tau},\overline{f}_d) &= \frac{1}{T_d}\int_0^{T_d} y_m(t)\cdot\{C_i(t-\overline{\tau})e^{j2\pi(f_{IF}+\overline{f}_d)t}\}dt \\ &= \frac{A_m}{2T_d}e^{-j\varphi_m}\{F\{P_{T_d}(t)\} * F\{b_{m,i}(t)\}\}_{f=\Delta f} \\ &= B_m\sum_{k=-\infty}^{\infty} a_{k(m,i)}\text{Sinc}\left(\left(\Delta f-\frac{k}{T_p}\right)\pi T_d\right)e^{-j(\Delta f-\frac{k}{T_p})\pi T_d} \end{aligned} \tag{3.12}$$

where $B_m = (A_m/2T_d)e^{-j\varphi_m}$, the subscript i denotes the i-th satellite code generated by the local generator, T_d is the integration time, $F\{\}$ denotes Fourier transform, the symbol $*$ denotes convolution operation, T_p is the code period, $\overline{\tau}$ is the code delay estimate introduced in the local code, $\text{Sinc}(x) = \sin(x)/x$, $\overline{f}_d$ is the Doppler frequency estimate introduced in the local carrier, Δf is the Doppler frequency estimate error which can be expressed as

$$\Delta f = f_{d,m} - \overline{f}_d \tag{3.13}$$

$b_{m,i}(t)$ is the product of two spreading codes, that is

$$b_{m,i}(t) = C_m(t-\tau_m)C_i(t-\overline{\tau}), \tag{3.14}$$

and P_{T_d} is a window function defined as

$$P_{T_d} = \begin{cases} 1, & 0 < t < T_d \\ 0, & \text{otherwise} \end{cases} \tag{3.15}$$

Since $b_{m,i}(t)$ is a periodic signal with a period equal to the code period, its Fourier transform leads to a line spectrum with coefficients given by

$$a_{k(m,i)} = \frac{1}{T_p}\int_{T_p} b_{m,i}(t)e^{-jk(2\pi/T_p)}dt \tag{3.16}$$

and the convolution with the line spectrum leads to the summation in (5.4).

In Figure 3.2 the distribution of $a_{k(m,i)}$ is shown in the case $\tau_m - \overline{\tau} = 0.2\ T_{ch}$, where T_{ch} is the chip duration. Thanks to the property of Pseudo Random

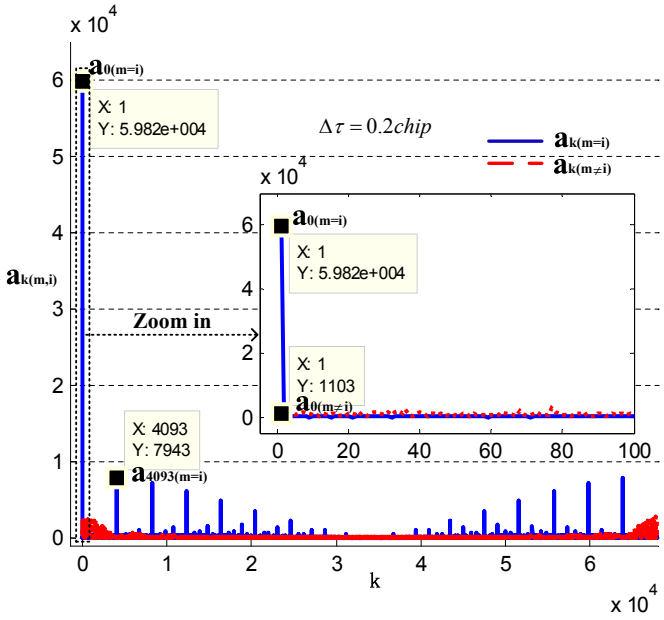

Figure 3.2: The value of a_k when $\tau_m - \overline{\tau} = \Delta\tau = 0.2\ T_{ch}$ in the GPS case.

Noise (PRN) code, as expected, $a_{0(m=i)}$ predominates over the other $a_{k(m,i)}$. To better understand the nature of the summation in (5.4), let us refer to Figure 3.3 where for simplicity, we represent the quantity

$$\sum_{k=-\infty}^{\infty} a_{k(i,i)} \left| \mathrm{Sinc}\left(\left(\Delta f - \frac{k}{T_p} \right) \pi T_d \right) \right| \tag{3.17}$$

to demonstrate the relationship among different Sinc functions. As Figure 3.3 shows, if a_0 is the peak component in (5.4) (the subscript i,i is omitted to simplify the notations) only the components strictly adjacent to a_0 (i.e. a_{-2} a_{-1} a_1 a_2 ...) affect the shape of the main lobe of (5.4), while the contribution of faraway components can be ignored. So, if we can guarantee that the adjacent coefficients (a_{-2} a_{-1} a_1 a_2 ...) are far smaller than a_0, the mathematical expression of the CAF in the main lobe (subscript 'ml') can be written as

$$\begin{aligned} S_i(\overline{\tau},\overline{f}_d)_{\mathrm{ml}} &= R_{i,i}(\overline{\tau},\overline{f}_d)_{\mathrm{ml}} + \sum_{m\neq i} R_{m,i}(\overline{\tau},\overline{f}_d)_{\mathrm{ml}} \\ &\approx \frac{A_i}{2} e^{-j\varphi_i} a_0 \mathrm{Sinc}(\Delta f \pi T_d) e^{-j\Delta f \pi T_d} \end{aligned} \tag{3.18}$$

where $a_0 = a_{0(i,i)} = R(\Delta\tau)$, and $\Delta\tau = \tau_m - \overline{\tau}$. As a conclusion the

approximate expression of the CAF in its main lobe is

$$S_i(\overline{\tau},\overline{f}_d)_{\mathrm{ml}} \approx \frac{A_i}{2} e^{-j\varphi_i} R(\Delta\tau)\mathrm{Sinc}(\Delta f \pi T_d) e^{-j\Delta f \pi T_d} \tag{3.19}$$

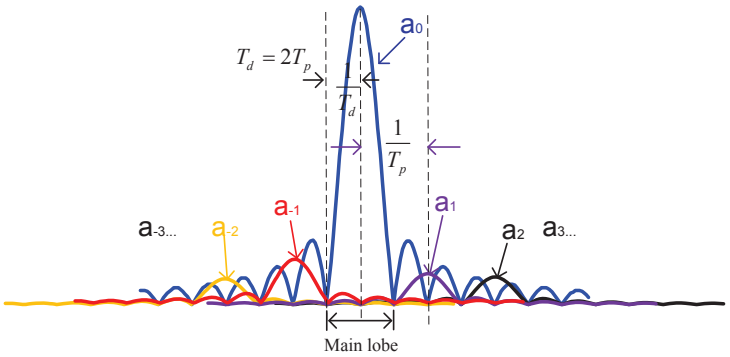

Figure 3.3: The combination of Sinc functions.

The validity of this approximation can be improved in two ways:

1. By enlarging the integration time T_d. In fact as T_d increases, the adjacent components will 'move' away relatively. In other words, as T_d increases the width of the lobe decreases, while the distance between two Sinc functions stays constant, as it depends on the code period.

2. By decreasing the values of the adjacent coefficients (a_{-2} a_{-1} a_1 a_2 ...). This can be obtained by improving the accuracy of code delay estimate, so as to work close to the maximum of $R(\Delta\tau)$.

Based on the CAF expression in (3.19), new algorithms for a better estimation of the Doppler frequency are discussed hereafter, both in ideal (i.e., noiseless, Section 3.3) and realistic (Section 3.4) scenarios.

3.3 Doppler frequency evaluation in the absence of noise

The signal acquisition process is basically a two dimensional search in a grid plane (commonly referred to as *search space*), as shown in Figure 3.4, where

$\overline{\tau} \in (0,T_p)$(X-axis range), and $\overline{f}_d \in (-f_{dmax},f_{dmax})$(Y-axis range). The variables under test $\overline{\tau}$ and $\overline{f}_d$ are discretized with a step τ_{sp} for the code delay, and a step f_{sp} for the Doppler frequency. The integration time is $T_d = LT_s$ (where L is the total number of integrated samples). The number of trial points in the two axes are $N_\tau = T_d/\tau_{sp}$, and $N_f = 2f_{dmax}/f_{sp}$. Therefore the grid plane contains $N_\tau \times N_f$ cells, and each cell (marked by yellow color in Figure 3.4) corresponds to a parameter pair $\langle \overline{\tau},\overline{f}_d \rangle$. Finally the decision variable for the acquisition is

$$\overline{S}(\overline{\tau},\overline{f}_d)_{\mathrm{ml}} = \left| S_i(\overline{\tau},\overline{f}_d)_{\mathrm{ml}} \right| \tag{3.20}$$

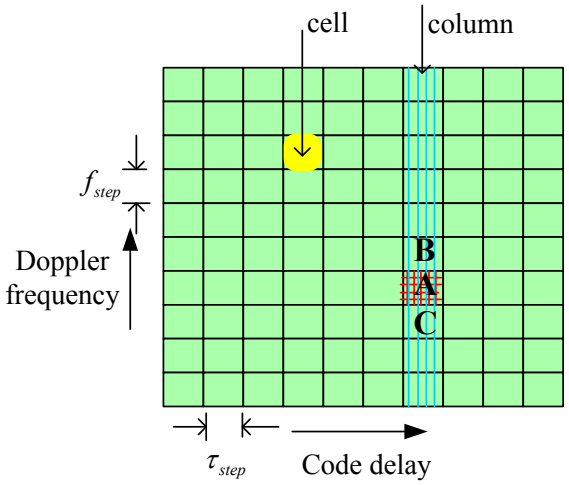

Figure 3.4: Two-dimensional search space.

The purpose of a traditional acquisition system is to find the coordinates of the peak cell of the grid plane when the satellite we want to detect is visible. To improve the accuracy of the estimates, the steps τ_{sp} and f_{sp} must be decreased, at the expenses of the computational complexity, since the number of points of the search space increases. The empirical value $f_{sp} = 2/(3LT_s)$ is a typical choice [34] for the Doppler frequency step.

An example of search space is shown in Figure 3.4. The column (marked in green) crossing the peak cell (marked A) contains cells which share the same code delay. When the i-th satellite is visible, the function in this column

is as shown in Figure 3.5, where the X-axis contains the variable Doppler frequency $\overline{f}_d$, while the Y-axis represents the absolute value of the acquisition test statistic $\overline{S}(\overline{\tau},\overline{f}_d)_{\mathrm{ml}}$. As indicated in Figure 3.3, the width of the main lobe is $2/T_d = 2/(LT_s)$. Since $f_{sp} = 2/(3LT_s)$, this guarantees that three adjacent points of the frequency domain CAF (A, B, C) are located in the main lobe, and then we can assume that (3.19) is always valid in these points.

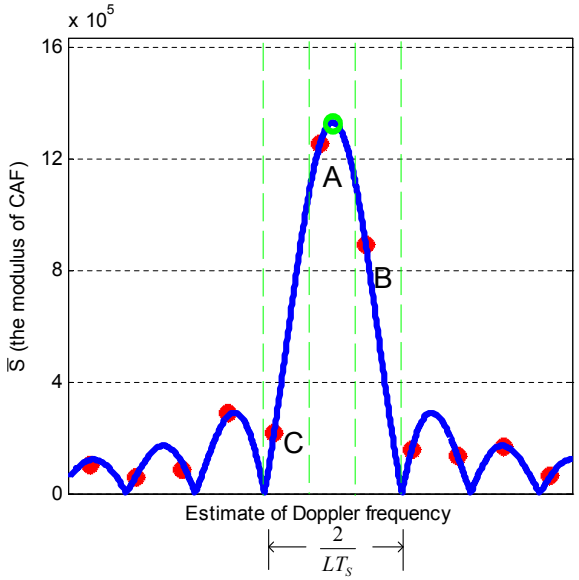

Figure 3.5: The plot of the column ($\overline{\tau} \approx \tau$).

The cells A B C are characterized by the triplets $(\overline{\tau}_A,\overline{f}_A,\overline{S}_A)$, $(\overline{\tau}_B,\overline{f}_B,\overline{S}_B)$, and $(\overline{\tau}_C,\overline{f}_C,\overline{S}_C)$, where the code delay is the same for all the cells in the same column ($\overline{\tau}_A = \overline{\tau}_B = \overline{\tau}_C$) and we adopt the notation $\overline{S}_X = \overline{S}(\overline{\tau}_X,\overline{f_{dX}})_{\mathrm{ml}}$, $X = (A,B,C)$ for simplicity. In the case of no noise, these triplets can be used to find the true Doppler frequency f_d, as it will be be shown hereafter. This will be also the starting point of the estimation method proposed in this chapter, when the measurements are affected by noise.

3.3.1 True solution based on the absolute value of CAF

In [41] which is our initial work on this topic, we can also find the basic idea about the solution based on the absolute value of the CAF. Under the

assumption that there is no data transition in the integration interval, based on (3.19) and (3.20) we can write the following equations [41]

$$\begin{aligned}\overline{S}_A &= \tfrac{A}{2}\,|R(\Delta\tau)|\,\left|\mathrm{Sinc}\left(\pi LT_s(f_d-\overline{f}_A)\right)\right| \\ \overline{S}_B &= \tfrac{A}{2}\,|R(\Delta\tau)|\,\left|\mathrm{Sinc}\left(\pi LT_s(f_d-\overline{f}_B)\right)\right| \\ \overline{S}_C &= \tfrac{A}{2}\,|R(\Delta\tau)|\,\left|\mathrm{Sinc}\left(\pi LT_s(f_d-\overline{f}_C)\right)\right|\end{aligned} \tag{3.21}$$

where the unknowns are the amplitude A, the value of the code correlation function $R(\Delta\tau)$, and the true Doppler frequency f_d. We are going to show that the value of f_d can be easily computed from the above system of equations [41].

First of all we observe that, when the points are located in the main lobe (like points A B C in Figure 3.5), we can write $\left|\mathrm{Sinc}(\pi LT_s(f_d-\overline{f}_A)\right| = \mathrm{Sinc}(\pi LT_s(f_d-\overline{f}_A))$. Now, according to (5.6) we write $\overline{f} = f_d - \Delta f$, so

$$\begin{aligned}\bar{f}\bar{S} &= (f_d-\Delta f)\overline{S} \\ &= f_d\overline{S} - \frac{A\,|R(\Delta\tau)|\sin(\pi LT_s\Delta f)}{2\pi LT_s}\end{aligned} \tag{3.22}$$

Based on (5.13) and (5.14), we can write

$$\overline{f}_A\overline{S}_A + \overline{f}_B\overline{S}_B + \overline{f}_C\overline{S}_C = f_d\overline{S}_A + f_d\overline{S}_B + f_d\overline{S}_C - S_{A,B,C} \tag{3.23}$$

where

$$S_{A,B,C} = \frac{A\,|R(\Delta\tau)|}{2\pi LT_s}\left(\sin(\pi LT_s\Delta f_A) + \sin(\pi LT_s\Delta f_B) + \sin(\pi LT_s\Delta f_C)\right) \tag{3.24}$$

Considering $f_{sp} = 2/(3LT_S)$:

$$\begin{aligned}\overline{f}_B &= \overline{f}_A + \frac{2}{3LT_s} \;\Rightarrow\; \Delta f_B = \Delta f_A + \frac{2}{3LT_s} \\ \overline{f}_C &= \overline{f}_A - \frac{2}{3LT_s} \;\Rightarrow\; \Delta f_C = \Delta f_A - \frac{2}{3LT_s}\end{aligned} \tag{3.25}$$

from which

$$S_{A,B,C} = \sin\left(\pi LT_s\Delta f_A\right) + \sin\left(\pi LT_s\Delta f_A + \frac{2\pi}{3}\right) + \sin\left(\pi LT_s\Delta f_A - \frac{2\pi}{3}\right) = 0 \tag{3.26}$$

By substituting (3.26) for $S_{A,B,C}$ in (3.23) we obtain $\overline{f}_A\overline{S}_A+\overline{f}_B\overline{S}_B+\overline{f}_C\overline{S}_C = f_d(\overline{S}_A+\overline{S}_B+\overline{S}_C)$, from which we can write the true Doppler frequency as

$$f_d = \frac{\overline{f}_A\overline{S}_A+\overline{f}_B\overline{S}_B+\overline{f}_C\overline{S}_C}{\overline{S}_A+\overline{S}_B+\overline{S}_C} \tag{3.27}$$

This expression gives the correct value of the Doppler frequency f_d, independently from the code delay error $\Delta\tau$, in the absence of noise and other nuisances. This equation represents a weighted average of the three measured points, and can be used as a first promising estimator of the Doppler frequency even when the CAF is affected by noise. Notice that (3.27) is valid only when the Doppler frequency step is $f_{sp} = 2/(3LT_S)$.

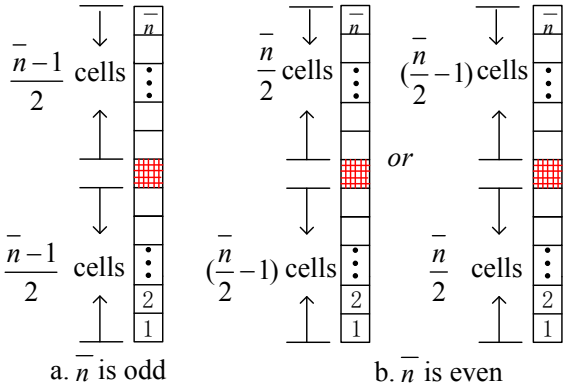

Figure 3.6: The cells chosen in the generalized method.

More in general, if we choose the Doppler frequency step as

$$f_{sp} = \frac{2}{\overline{n}LT_s} \tag{3.28}$$

where $\overline{n}$ is a positive integer, we can choose the cells as follows:

- When $\overline{n}$ is odd, we take $(\overline{n}-1)/2$ cells at each side of the peak cell as shown in Figure 3.6(a).
- When $\overline{n}$ is even, we take $\overline{n}/2$ cells at one side and $[(\overline{n}/2)-1]$ cells on the other side of the peak cell, as Figure 3.6(b) shows.

No matter what value $\overline{n}$ assumes (even or odd), there will be $\overline{n}$ cells taken into the final calculation, and (3.26) will become

$$\sum_{k=0}^{\overline{n}-1} \sin\left(\pi L T_s \Delta f_1 + \frac{2k}{\overline{L} T_s}\right) = 0 \tag{3.29}$$

where $\Delta f_1 = f_d - \overline{f}_1$ and $\overline{f}_1$ is the trial value of the Doppler frequency in the first cell of the set (i.e., the cell 1 marked in Figure 3.6). Then (3.27) becomes

$$f_d = \frac{\sum_{k=1}^{\overline{n}} \overline{f}_k \overline{S}_k}{\sum_{k=1}^{\overline{n}} \overline{S}_k} \tag{3.30}$$

which can be adopted as an estimator of the Doppler frequency in the presence of noise.

For simplicity, hereafter we refer to solution (3.27) as algorithm R-3 and solution (3.30) as algorithm R-$\overline{n}$.

3.3.2 True solution based on complex values of CAF

Based on[33, 35], we can obtain another similar solution by using the test statistic $\overline{S}(\overline{\tau},\overline{f}_d)_{\mathrm{ml}}$ in the complex form given in (3.19). In fact it is possible to show that

$$\begin{aligned} f_{d,complex} &= \mathrm{Real}\left\{\frac{\overline{f}_C S_C + \overline{f}_A S_A e^{-j\pi f_{sp} T_d} + \overline{f}_B S_B e^{-j2\pi f_{sp} T_d}}{S_C + S_A e^{-j\pi f_{sp} T_d} + S_B e^{-j2\pi f_{sp} T_d}}\right\} \\ &= \mathrm{Real}\left\{\frac{\left(\overline{f}_C |S_C| + \overline{f}_A |S_A| + \overline{f}_B |S_B|\right) e^{-j(\pi \Delta f_C T_d + \varphi_i)}}{(|S_C| + |S_A| + |S_B|) e^{-j(\pi \Delta f_C T_d + \varphi_i)}}\right\} \\ &= \frac{\overline{f}_C |S_C| + \overline{f}_A |S_A| + \overline{f}_B |S_B|}{|S_C| + |S_A| + |S_B|} \\ &= f_d \end{aligned} \tag{3.31}$$

At the same time, similarly to (3.30), we can generalize this solution as

$$f_{d,complex} = \mathrm{Real}\left\{\frac{\sum_{k=1}^{\overline{n}} \overline{f}_k S_k e^{-j(k-1)\pi f_{sp} T_d}}{\sum_{k=1}^{\overline{n}} S_k e^{-j(k-1)\pi f_{sp} T_d}}\right\} \tag{3.32}$$

where $\overline{f}_{k+1} = \overline{f}_k + f_{sp}$ and f_1 is the Doppler frequency value in cell 1 marked in Figure 3.6.

For simplicity, hereafter we refer to solution (3.31) as algorithm C-3 and solution (3.32) as algorithm C-$\overline{n}$.

3.3.3 Test of validity

The formulas in the previous sections show that, in the absence of noise and other nuisances, the proposed equations are able to evaluate the true Doppler frequency, so leading the estimation error range from the traditional $(-f_{sp}/2, f_{sp}/2)$ to theoretically zero. A possible residual error can arise due

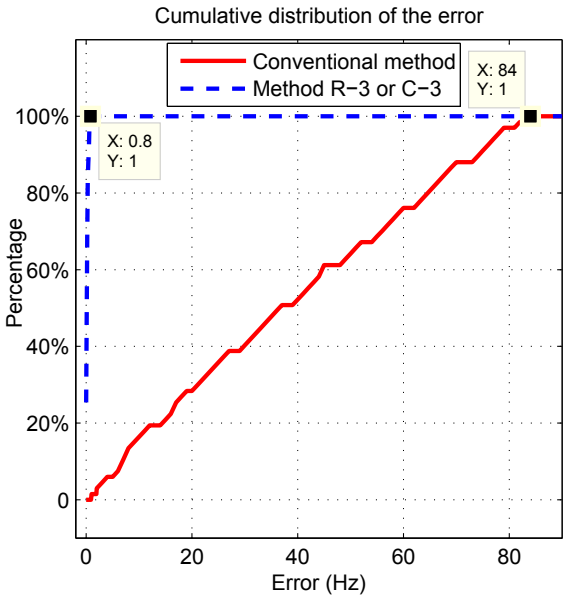

Figure 3.7: Cumulative distribution of the frequency errors (comparison between the conventional and methods R-3 and C-3).

to the fact that the method is based on an approximate formulation of the test statistic (3.19). Therefore to test its validity, we set up a simulated acquisition campaign, where the Doppler frequency estimation error due to the traditional acquisition method is compared with the residual error introduced by the algorithms R-3, R-$\overline{n}$, C-3, and C-$\overline{n}$. In the simulations the GNSS signals are generated by using the signal simulator N-FUELS [44], and several

instances of a Galileo E1-b signal are obtained. Firstly we tested the methods in an ideal scenario (i.e., noiseless), with parameters $f_{IF} = 4$ MHz, $f_s = 17$ MHz, $\tau = 0.11$ ms.

The accumulation time of the acquisition stage is set to the minimum period (4 ms), assuming that no data transition occurs in this period, the Doppler frequency step is

$$f_{sp} = \frac{2}{3LT_s} = 167 \text{ Hz} \tag{3.33}$$

and 67 different values of f_d are randomly chosen in the range (−4500,4500) Hz. This makes the original errors uniformly distributed in $(-f_{sp}/2, f_{sp}/2)$, as also proved in Figure 3.7, where the cumulative distribution of the Doppler frequency estimation errors is shown. After the refinements obtained by using R-3 or C-3, the error range decreases to nearly (−0.8,0.8) Hz, which is a residual numerical error due to the approximations introduced in (5.12), (3.19).

So we can conclude that in the absence of noise, in experiments, the new methods eliminate the error in the evaluation of the Doppler frequency due to the discretization of the search space, just using three cells selected in the main lobe of the frequency-domain CAF. The only constraint is that the Doppler frequency step has to be as given in (5.17), with $\overline{n} = 3$. Moreover the obtained results show that the method is not affected by the code delay error $\Delta\tau$.

The practical situation in which the noise is unavoidable is discussed in the next section.

3.4 Doppler frequency estimation in the presence of noise

In real scenarios, we have to consider the influence of noise, which can be modeled as an Additive White Gaussian Noise (AWGN), as it is usual in the

literature. Then the received signal model becomes

$$\begin{aligned}\widetilde{y}(nT_s) &= y(nT_s) + \eta(nT_s) \\ &= Ac(nT_s - \tau)s_b(nT_s - \tau)d(nT_s - \tau) \\ &\cos\left(2\pi(f_{IF} + f_d)nT_s + \varphi\right) + \eta(nT_s)\end{aligned} \tag{3.34}$$

where $\eta(nT_s)$ represents the white Gaussian noise normally distributed with zero mean and variance σ_{IF}^2, related to the power spectral density $S_N(f) = N_0/2$ of the analogue noise by the well-known formula

$$\sigma_{IF}^2 = E\left\{\eta^2(nT_s)\right\} = \frac{N_0 f_s}{2} \tag{3.35}$$

valid when the transfer function of the equivalent front-end filter is assumed flat over the whole digitization bandwidth $(-f_s/2, f_s/2)$. Without considering the data-transition, the In-phase and Quadrature components of the CAF for the local parameters $\overline{f}_d$ and $\overline{\tau}$ can be written as

$$\begin{aligned}I(\overline{\tau},\overline{f}_d) &= \frac{1}{N}\sum_{n=0}^{N-1}\left(y(nT_s) + \eta(nT_s)\right)C(nT_s - \overline{\tau})\cos\left(2\pi(f_{IF} + \overline{f}_d)\right) \\ Q(\overline{\tau},\overline{f}_d) &= \frac{1}{N}\sum_{n=0}^{N-1}\left(y(nT_s) + \eta(nT_s)\right)C(nT_s - \overline{\tau})\sin\left(2\pi(f_{IF} + \overline{f}_d)\right)\end{aligned} \tag{3.36}$$

which, based on (3.19) (and omitting the subscript i), becomes

$$\begin{aligned}I(\overline{\tau},\overline{f}_d) &= \text{Real}\left\{S(\overline{\tau},\overline{f}_d)\right\} + N_I \\ Q(\overline{\tau},\overline{f}_d) &= \text{Img}\left\{S(\overline{\tau},\overline{f}_d)\right\} + N_Q\end{aligned} \tag{3.37}$$

where Real{} and Img{} mean respectively real and imaginary part of a complex value, and

$$\begin{aligned}N_I &= \frac{1}{N}\sum_{n=0}^{N-1}\eta(nT_s)C(nT_s - \overline{\tau})\cos\left(2\pi(f_{IF} + \overline{f}_d)\right) \\ N_Q &= \frac{1}{N}\sum_{n=0}^{N-1}\eta(nT_s)C(nT_s - \overline{\tau})\sin\left(2\pi(f_{IF} + \overline{f}_d)\right)\end{aligned} \tag{3.38}$$

According to [45], we know that N_I and N_Q are still white noise processes with variance $\text{var}(N_I) = \text{var}(N_Q) = \sigma_{IF}^2/(2N)$, and the envelope of $\widetilde{S}(\overline{\tau},\overline{f}_d) =$

$I + jQ$ is

$$\begin{aligned}\widetilde{\overline{S}}(\overline{\tau},\overline{f}_d)^2 &= I(\overline{\tau},\overline{f}_d)^2 + Q(\overline{\tau},\overline{f}_d)^2 \\ &= \overline{S}(\overline{\tau},\overline{f}_d)^2 + 2\text{Real}\left\{S(\overline{\tau},\overline{f}_d)\right\} N_I + 2\text{Img}\left\{S(\overline{\tau},\overline{f}_d)\right\} N_Q + N_I^2 + N_Q^2 \\ &= \overline{S}(\overline{\tau},\overline{f}_d)^2 + w_I + w_Q \end{aligned} \tag{3.39}$$

where the term $w_I + w_Q = w$ is a random process with mean $E\{w\} = E\{N_I^2 + N_Q^2\} = \sigma_{IF}^2/N$ including all the noise contributions. At this point, working as in (3.27) or (3.31), we can develop two new estimators in the presence of noise, that is

$$\widehat{f}_d = \frac{\overline{f}_A \widetilde{\overline{S}}_A + \overline{f}_B \widetilde{\overline{S}}_B + \overline{f}_C \widetilde{\overline{S}}_C}{\widetilde{\overline{S}}_A + \widetilde{\overline{S}}_B + \widetilde{\overline{S}}_C} \tag{3.40}$$

and

$$\widehat{f}_{d,complex} = \text{Real}\left\{ \frac{\overline{f}_C \widetilde{S}_C + \overline{f}_A \widetilde{S}_A e^{-j\pi f_{sp} T_d} + \overline{f}_B \widetilde{S}_B e^{-j2\pi f_{sp} T_d}}{\widetilde{S}_C + \widetilde{S}_A e^{-j\pi f_{sp} T_d} + \widetilde{S}_B e^{-j2\pi f_{sp} T_d}} \right\} \tag{3.41}$$

(for simplicity the Doppler frequency step is as in (3.33)).

Hereafter, we refer to (3.40) as algorithm 'R_n-3' and to (3.41) as algorithm 'C_n-3'. As before, they can be generalized to 'R_n-$\overline{n}$' and 'C_n-$\overline{n}$'.

In the following two subsections we discuss two terms of comparison worth to be considered for the frequency estimators proposed so far. First, a least squares solution; second, the CRLB on the variance of the estimator. Performance comparisons obtained in simulation are presented in subsection 3.4.3.

3.4.1 Least-square method

Another approach to exploit the CAF points $\widetilde{\overline{S}}_A, \widetilde{\overline{S}}_B, \widetilde{\overline{S}}_C$ as defined in (3.39) is to set up a least squares (LS) problem as follows.

Since we know that the main lobe of the CAF is a Sinc function, it is possible to use the LS method in which the fitting curve is the Sinc function (5.13).

The LS method requires that the sum of the squared residuals

$$Q_{LS}(\bar{A},f_d) = \left(\widetilde{\overline{S}}_A - \overline{S}_A\right)^2 + \left(\widetilde{\overline{S}}_B - \overline{S}_B\right)^2 + \left(\widetilde{\overline{S}}_C - \overline{S}_C\right)^2 \tag{3.42}$$

is minimized with respect to the unknown parameters, where $\bar{A} = A/(2R(\Delta\tau))$. This leads to the equations

$$\begin{aligned} \frac{\partial Q_{LS}(\bar{A},f_d)}{\partial \bar{A}} &= 0 \\ \frac{\partial Q_{LS}(\bar{A},f_d)}{\partial f_d} &= 0 \end{aligned} \tag{3.43}$$

Since we are interested in the performance comparison with R_n-3 or C_n-3, we will use a numerical method to solve (3.43) for f_d.

3.4.2 Evaluation of the Cramer-Rao lower bound

Usually, a statistical estimator is characterized by its bias (mean error), variance (mean square error), and the threshold SNR (signal-to-noise ratio) [5]. So here, the Cramer-Rao lower bound (CRLB) is proposed as benchmark to compare the performance of different algorithms.

Without considering the data-transition problem and ignoring the influence of the code delay estimation error (which will be discussed in section 3.5.2), the received samples (3.34) can be mathematically expressed as

$$\begin{aligned} \widetilde{y}(nT_s) &= y(nT_s) + \eta(nT_s) \\ &= A\cos\left(2\pi(f_{IF} + f_d)nT_s + \varphi\right) + \eta(nT_s) \end{aligned} \tag{3.44}$$

which contains the unknown parameter vector $\boldsymbol{\theta} = [A,f_d,\varphi]$. The corresponding Fisher information matrix $\mathbf{I}$ for an observation of N samples has elements [5]

$$[\mathbf{I}(\boldsymbol{\theta})]_{ij} = \frac{1}{\sigma^2}\sum_{n=0}^{N-1} \frac{\partial y(n;\boldsymbol{\theta})}{\partial \boldsymbol{\theta}_i}\frac{\partial y(n;\boldsymbol{\theta})}{\partial \boldsymbol{\theta}_j} \tag{3.45}$$

where $y(n;\boldsymbol{\theta}) = A\cos(2\pi(f_{IF}+f_d)nT_s+\varphi)$, and N is the number of samples used for the estimation of the unknowns. Therefore the Fisher matrix is

$$\mathbf{I}(\boldsymbol{\theta}) = \frac{1}{\sigma_{IF}^2}\begin{bmatrix} \frac{N}{2} & 0 & 0 \\ 0 & 2\pi^2A^2T_s^2\sum_{n=0}^{N-1}n^2 & \pi A^2T_s\sum_{n=0}^{N-1}n \\ 0 & \pi A^2T_s\sum_{n=0}^{N-1}n & \frac{NA^2}{2} \end{bmatrix} \tag{3.46}$$

The CRLB is found as the $[i,i]$ element of the inverse of the Fisher matrix:

$$\mathrm{var}(\boldsymbol{\theta}_i) \geq \left[\mathbf{I}^{-1}(\boldsymbol{\theta})\right]_{ii}. \tag{3.47}$$

Therefore the CRLB for the Doppler frequency estimate is

$$\begin{aligned} \mathrm{var}(\widehat{f_d}) &\geq \left[\mathbf{I}^{-1}(\boldsymbol{\theta})\right]_{22} \\ &\geq \frac{12}{(2\pi)^2\ \rho\ T_s^2N(N^2-1)} \end{aligned} \tag{3.48}$$

where $\rho = A^2/(2\sigma_{IF}^2)$. As $N = f_sT_d \gg 1$, so (3.48) can be written as

$$\begin{aligned} \mathrm{var}(\widehat{f_d}) &\geq \left[\mathbf{I}^{-1}(\boldsymbol{\theta})\right]_{22} \\ &\geq \frac{12}{(2\pi)^2\ \rho\ f_sT_d^3} \end{aligned} \tag{3.49}$$

which is the benchmark for our estimation algorithms.

3.4.3 Simulation experiments for performance assessment

To test the algorithms R_n-3, C_n-3, and LS we performed several simulation experiments with different values of the carrier-to-noise density ratio (CNR), corresponding to a signal-to-noise ratio ρ given by:

$$SNR = \frac{C}{N_0B} \tag{3.50}$$

where B is the one side front-end bandwidth, assumed ideally flat over the whole digitization bandwidth.

The parameters used in the experiments are $f_{IF} = 4$ MHz, $f_s = 17$ MHz, $\tau = 0.11$ms, and f_{sp} is set as in (3.33). We use the root-mean-square error

(RMSE) computed for the different algorithms as a metric of performance comparison:

$$f_{RMSE} = \sqrt{E\left\{(\widehat{f}_d - f_d)^2\right\}} \tag{3.51}$$

where $\widehat{f}_d$ is the Doppler frequency estimate, and $E\{\cdot\}$ is the expected value (estimated as a temporal average along the simulation runs). The metric f_{RMSE} is calculated for each algorithm and compared with the square root of CRLB.

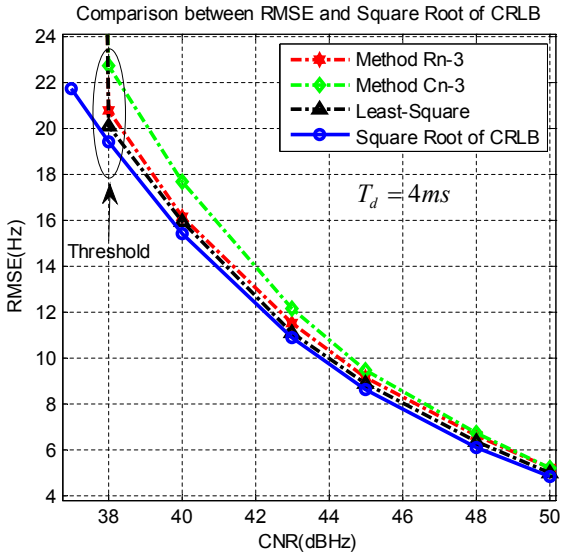

Figure 3.8: Results of the first group of experiments, with $T_d = 4$ ms (including the false alarm).

In the first group of experiments, we set $T_d = 4$ ms and we executed 1000 runs for each CNR. Then, according to (3.51), we calculated the corresponding RMSE. The results can be seen in Figure 4.1. We can see that in this case the algorithm R_n-3 is better than C_n-3, as it achieves a lower RMSE closer to the CRLB. At the same time we can see that the algorithm R_n-3 is very close to the least-square method, though the latter is slightly better. However, considering the computation complexity of the LS method, the algorithm R_n-3 appears really competitive with respect to the LS. Finally, the threshold CNR (below which the RMSE rapidly worsens) is around CNR=38 dBHz in all the proposed methods.

In the second group of experiments, we changed the integration time to $T_d =$ 8ms. Similarly, we executed 1000 runs for each CNR and obtained the results reported in Figure 4.2, where we can observe that, as expected, the RMSE is lower than in Figure 4.1, since a longer integration time reduces the effects of noise. Again, R_n-3 is the closest to the least-square method, and the threshold CNR decreases to around CNR=35 dBHz in all three proposed methods.

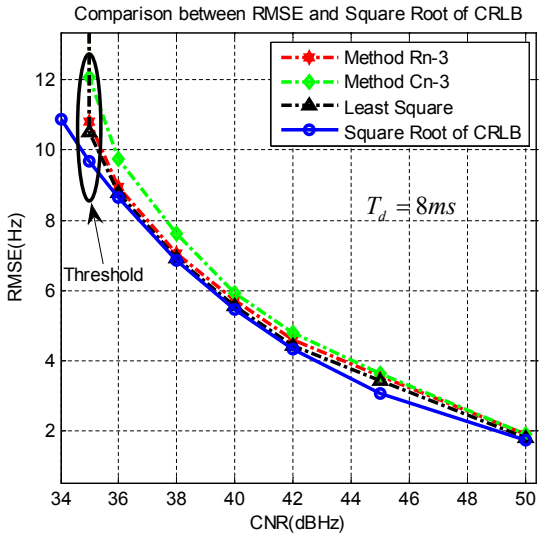

Figure 3.9: Results of second group of experiments, with $T_d = 8$ ms.(including the false alarm).

Comparing Figure 4.1 and Figure 4.2 we can observe that, first, at the same CNR, the RMSE in Figure 4.2 is decreased by about a factor of 2.8 with respect to Figure 4.1. This is in agreement with the theoretical CRLB given in (3.49). In fact when $T_d = 4$ ms is replaced with $T_d = 8$ ms the CRLB bound decreases by a factor $\sqrt{8}$. Furthermore, when CNR is relatively high (like CNR$\geq$ 45dBHz in Figure 4.1), the proposed three algorithms are very close to the CRLB and each other.

3.4.4 Averaging method

Since noise is dominant in the acquisition process, in order to increase the robustness of the proposed approach in the presence of noise, the performance of a simple averaging method, based on the idea of non-coherent sums, is assessed here. The main steps of the method represented in Figure 4.3 are:

1. Find the initial code delay using a first period of data, then pick out the column (marked in blue color in Figure 3.4), and save $(2J+1)$ points (J points at each side of the peak point as illustrated in Figure 4.3)

2. Use the parameter $\langle \overline{f}_d, \overline{\tau} \rangle$ evaluated in the first step to calculate the new columns (as shown in Figure 4.3) of the next $(M-1)$ periods of data.

3. Calculate the average of the M columns into one single mean column.

4. Pick out the top $\overline{n}$ cells in the mean column and use (3.40) to calculate the final Doppler frequency.

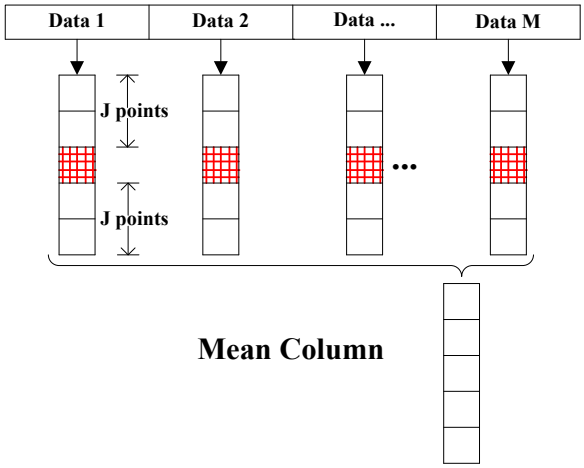

Figure 3.10: Averaging method.

In the following simulation, we set CNR=43 dBHz, $\overline{n} = 3$, $J = 2$, $M = 4$, and we execute 1000 independent runs, for both averaging and non-averaging

strategies. The result is shown in Figure 4.4, where we can see that the new averaging method decreases the error range from (-25,25) Hz to nearly (-15,15) Hz.

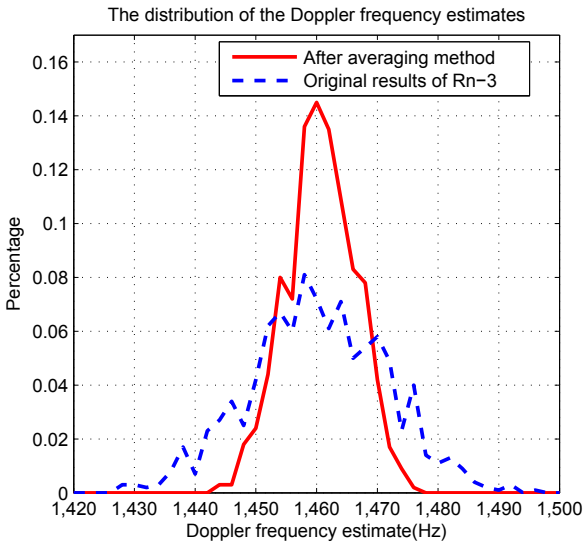

Figure 3.11: The distribution of the Doppler frequency estimates.

3.5 Analysis of other non-AWGN nuisances

The performance of the algorithms presented so far depends not only on the additive noise, but also on other nuisances, whose impact is analyzed in this section. In particular we observe that the methods R_n-3 and C_n-3 are based on the two measured vectors $\mathbf{f} = [\overline{f}_C, \overline{f}_A, \overline{f}_B]$ and $\bar{\mathbf{S}} = [S_C, S_A, S_B]$ used in (3.27) and (3.31), obtained by reading the peak cell and the adjacent cells in the same column (marked as C A B in Figure 3.20). In particular, the code delay $\overline{\tau}_p$ is kept constant in these three cells.

Since the search space is discretized, in general even in the absence of noise $\overline{f}_p \neq f_d$, and $\overline{\tau}_p \neq \tau$. This can be seen as a quantization error $\Delta f_q = \overline{f}_p - f_d$ in the frequency domain, and $\Delta\tau_q = \overline{\tau}_p - \tau$ in the time domain. We know that equations (3.27) and (3.31) completely eliminate the quantization errors in the absence of noise. However, in the presence of noise, we experience

an accuracy degradation due to the noise influence on vector $\bar{\mathbf{S}}$, as shown in the simulation results of the previous section. The purpose of the following analysis is to state the influence of the frequency and code delay quantization errors on the proposed frequency estimators, in the presence of noise.

3.5.1 The influence of the peak point's location

In this section we study the influence of the quantization error in the frequency domain, which can be re-elaborated as

$$\Delta_p = \left| \frac{\Delta f_q}{f_{sp}} \right| \tag{3.52}$$

from which it is evident that $0 \leq \Delta_p \leq 0.5$. Using (3.40) and setting f_{sp} as in (3.33), the estimation error can be expressed as

$$\begin{aligned}
\hat{f}_d - f_d = \delta_f &= \frac{\overline{f}_A \widetilde{\overline{S}}_A + \overline{f}_B \widetilde{\overline{S}}_B + \overline{f}_C \widetilde{\overline{S}}_C}{\widetilde{\overline{S}}_A + \widetilde{\overline{S}}_B + \widetilde{\overline{S}}_C} - f_d \\
&= \frac{(f_d + \Delta f_A)\widetilde{\overline{S}}_A + (f_d + \Delta f_A + f_{sp})\widetilde{\overline{S}}_B + (f_d + \Delta f_A - f_{sp})\widetilde{\overline{S}}_C}{\widetilde{\overline{S}}_A + \widetilde{\overline{S}}_B + \widetilde{\overline{S}}_C} - f_d \\
&= \frac{\Delta f_A \widetilde{\overline{S}}_A + (\Delta f_A + f_{sp})\widetilde{\overline{S}}_B + (\Delta f_A - f_{sp})\widetilde{\overline{S}}_C}{\widetilde{\overline{S}}_A + \widetilde{\overline{S}}_B + \widetilde{\overline{S}}_C} \\
&= \Delta f_A + \frac{f_{sp}(\widetilde{\overline{S}}_B - \widetilde{\overline{S}}_C)}{\widetilde{\overline{S}}_A + \widetilde{\overline{S}}_B + \widetilde{\overline{S}}_C}
\end{aligned} \tag{3.53}$$

From (3.53), and using the definition (3.52), we can calculate the expected value of δ_f as

$$E\{\delta_f\} = f_{sp} E\left\{ \Delta_p + \frac{\widetilde{\overline{S}}_B - \widetilde{\overline{S}}_C}{\widetilde{\overline{S}}_A + \widetilde{\overline{S}}_B + \widetilde{\overline{S}}_C} \right\} \tag{3.54}$$

From this result we observe that the residual error depends on both the noise contribution in the vector $\bar{\mathbf{S}}$ and the parameter Δ_p.

From Figure 5.8 we can see that Δ_p influences the accuracy of the proposed three methods, especially when it comes to the top limit 0.5. This result suggested us to adopt a strategy to mitigate this effect. Recalling Figure 3.4, in which 'A' is the peak point, 'B' is the second high point and 'C' is

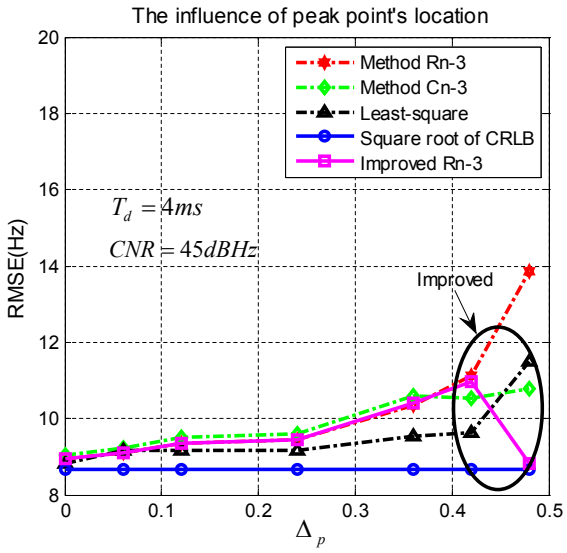

Figure 3.12: Influence of the quantization error on the RMSE as a function Δ_p.

the lowest point independently from their relative position on the frequency axis, we can easily observe that, when Δ_p is close to the limit 0.5, then $\overline{S}_C$ is close to zero. In this case the residual error defined in (3.39) introduces a significant error in the estimate (3.40), since noise dominates in point 'C'. This is experimentally proven in Figure 5.8, where the curves of R_n-3 and C_n-3 show an increasing RMSE as Δ_p increases, while the LS appears slightly more robust.

So when Δ_p is close to 0.5, to limit the accuracy degradation we changed the algorithm (3.40) as

$$\widehat{f}_{d,rel} = \frac{\overline{f}_A \widetilde{\overline{S}}_A + \overline{f}_B \widetilde{\overline{S}}_B}{\widetilde{\overline{S}}_A + \widetilde{\overline{S}}_B} \tag{3.55}$$

which will be used whenever the point 'C' gets close to zero. The idea is to ignore the 'C' term, because when Δ_p is close to 0.5, the true value $\overline{S}_C$ is nearly zero and $\widetilde{\overline{S}}_C$ mainly contains noise.

To implement this method, a threshold control has to be added, as drawn in Figure 5.9. Here we use the empirical criterion $\widetilde{\overline{S}}_B / \widetilde{\overline{S}}_A > 0.92$ to decide whether Δ_p is critically close to 0.5 or not. In Figure 5.8 we can observe

the result of the method drawn in Figure 5.9 (continuous line with square markers), which is able to consistently reduce the RMSE when Δ_p is close to 0.5 .

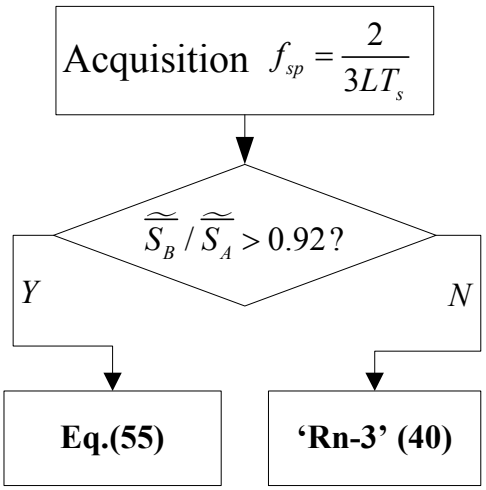

Figure 3.13: The strategy used in improved algorithm R_n-3.

3.5.2 The influence of the code delay error

The peak column selected in the search space (marked in Figure 3.20) also depends on the resolution of the search space in the code delay domain. The mentioned quantization error $\Delta\tau_q = \overline{\tau}_p - \tau$ affects the CAF samples with an amplitude scale factor $|R(\Delta\tau_q)|$ as shown in (5.13), where now $\Delta\tau = \Delta\tau_q$. This factor is expected to affect the performance of the estimators C_n-3, and R_n-3.

The influence of such a code delay error can be quantified by modifying the expression of the signal-to-noise ratio ρ in the CRLB (3.49), so as to take into account the term $R(\Delta\tau_q)$. Thus, defining the modified SNR $\tilde{\rho} = \frac{A^2|R(\Delta\tau_q)|^2}{2\sigma_{IF}^2}$, (3.49) becomes

$$\mathrm{var}(\widehat{f_d}) \geq \frac{12}{(2\pi)^2\ \tilde{\rho}\ f_s T_d^3} \tag{3.56}$$

From (3.56), because $R(\Delta\tau_q \leq 1)$, we can conclude that the CRLB value increases as the code delay $\Delta\tau_q$ increases; this increase will be also experienced by the RMSE of the proposed algorithms. In conclusion the effect of the quantization error $\Delta\tau_q$ is an attenuation, which does not modify the results of Figure 4.1 and Figure 4.2, except for a scaling factor in the abscissa.

3.6 Conclusion

In this chapter a new family of algorithms is proposed for the fine estimation of the Doppler frequency based on an approximate analytical expression of the CAF. The proposed methods have been analyzed in both ideal (i.e., noiseless) and realistic (i.e., noisy) scenarios and compared with a similar LS approach. The CRLB has been derived and used as benchmark for performance assessment. The influences non-AWGN nuisances is also analyzed under a theoretical perspective. In application, from the experiments, we can see that the method R_n-3 almost achieves the performance of LS, which is very close to CRLB, but the complexity of R_n-3 is notably lower. Moreover, performance can be improved by adopting a simple averaging method.

Chapter 4

New Design of a FLL Discriminator Based on Energy

4.1 Introduction

With the development of Global Navigation Satellite System (GNSS), different satellite systems are coming up, such as Galileo, Compass and modernization of GPS. To improve the performance (increased accuracy, enhanced tracking robustness and better resistance against multipath and interference) and compatibility with the other present navigation systems, the signal modulation methods are chosen appropriately [26]. With respect to these changes, there is a benefit in adjusting the traditional receiver architectures to adapt to the new trend.

The main broad objective of a GNSS receiver is to synchronize the local signal with the incoming satellite signal and decode the navigation message to calculate the final navigation solution. This process normally involves four logical stages which are acquisition, tracking, data demodulation and Position-Velocity-Time (PVT) calculation [1]. The acquisition stage is aimed at providing the coarse estimates of frequency shift and code delay, which are

passed to the tracking loops, including Phase-Lock-Loop (PLL), Frequency-Lock-Loop (FLL) and Delay-Lock-Loop (DLL), dedicated to refine the unknown parameters and maintain the local signal synchronized with the incoming satellite signal. In cascade, PVT results are computed and made available at a certain output rate.

Focusing on carrier tracking, a traditional well-designed receiver starts from a FLL stage with a wide-band carrier loop filter to refine the coarse frequency estimate to some acceptable degree, eventually it moves into a PLL using a bandwidth as narrower as the anticipated dynamics permits. Due to the data transition that may happen in the incoming signal, the discriminators both used in FLL and PLL are commonly insensitive to 180-deg phase reversals, consequently decreasing the pull-in range [1]. In the modern GNSS systems, like in Galileo E1 signal, the navigation data duration is set to 4 ms, equal to the period of the Pseudo-Random-Noise (PRN) code. For this reason, a traditional tracking architecture is subject to the potential phase jump and frequency ambiguity problem caused by frequent data-transition.

In [6] both four-quadrant and two-quadrant arctangent discriminators in FLL are analyzed. Four-quadrant arctangent discriminator is sensitive to data-transition, though two-quadrant arctangent function can solve the problem but it narrows the pull-in range at the same time. Reference [10] proposes a new discriminator based on energy (i.e., the accumulation result of one period of data), but the mathematical expression of the discriminator is complex; it involves approximation and also needs to know the value of signal amplitude and code delay error to compute the exact frequency error. Here in this chapter, based on our previous work [9], a new FLL discriminator based on energy is proposed. It differs from [10] in that the mathematical formula of the discriminator is simpler and more accurate, and, most importantly, it is independent from the knowledge of signal amplitude and code delay error. Compared with traditional arctangent discriminators, it has larger pull-in range, which means it can bear more dynamic stress and still can converge

to the correct frequency estimate even with a large initial frequency error. At the same time it is also definitely insensitive to the data-transition as it can determine the frequency error only using the minimum period of received data while in traditional way, at least two consecutive periods of data are needed.

A significant enhancement carried with new GNSS signals is the presence of dataless pilot channel which shares 50% of the total transmitted power while the other half part is occupied by data channel, as in the Galileo E1 OS signal [26]. Therefore, if only one channel is used, as conventional GNSS receivers do, half of the total transmitted power is wasted, under the tracking point of view. In order to take full usage of both modulation channels, [46, 47] propose algorithms for data/pilot combination. All these joint data/pilot architectures are designed for the acquisition process and analyzed mainly in terms of receiver operating characteristic (ROC). Thus, the idea of data/pilot combination can also be applied in our new FLL discriminator to improve signal-to-noise ratio (SNR), aiming at a theoretical 3 dB improvement in SNR, compared to the previous FLL without usage of pilot channel.

The chapter is organized as follows: In section 2, the GNSS signal model is analyzed and the new discriminator is derived. In section 3, the comparison with traditional ATAN discriminator and another similar one in [10] is done to prove the advantages of new proposed discriminator; at the same time, a representative simulation is shown to evaluate the performance of the three different discriminators in case of a large initial frequency error. In section 4, the coherent combination of data and pilot is analyzed and adopted to improve the frequency estimate accuracy by exploiting full transmitted power. Finally, in section 5 the conclusion is drawn.

4.2 New FLL Discriminator

The new FLL discriminator proposed in this chapter is based on a measure of energy, i.e., on the result of accumulating the correlated signal along one period of data. Similarly to a DLL discriminator, it computes the frequency error only using minimum period of data equal to the period of PRN. Besides that, compared with a conventional FLL discriminator, it has larger pull-in range which guarantees the capability of bearing more dynamic stress. Based on the previous work in [9], this FLL discriminator can be treated as a maximum-likelihood (ML) estimator in case of the closed-loop structure; even in a quasi-open loop case [48], it can still achieve performance close to that of a ML estimator. The whole derivation is presented in the following sections.

4.2.1 General Signal Model

The incoming signal from one visible satellite passes through the receiver RF front-end, which consists of pre-amplification, down-conversion, filtering, IF sampling and AD conversion. This process leads to the received digital signal which can be mathematically expressed as [1]:

$$y[n] = A{\cdot}c(nT_s{-}\tau)s_b(nT_s{-}\tau)d(nT_s{-}\tau){\cdot}\cos[2\pi(f_{IF}{+}f_d)nT_s{+}\varphi_0]{+}\eta[n] \quad (4.1)$$

where: A is the amplitude of the satellite signal, τ is the code delay of the satellite signal, T_s is the sampling interval (the inverse of the sampling frequency f_s), $c(nT_s - \tau)$ is the PRN code of the satellite, $s_b(nT_s - \tau)$ is the subcarrier used in new GNSS system ($s_b(nT_s - \tau) = 1$ when there is no subcarrier), $d(nT_s - \tau)$ is the navigation data of the satellite, f_{IF} is the intermediate frequency, f_d is the Doppler frequency in units of rad/s, φ_0 is the phase of the carrier and $\eta[n]$ is the additive noise, assumed as a white Gaussian noise (WGN) sequence with two-sided power spectral density (PSD)

$N_0/2$. Then

$$\eta[n] \sim (0,\sigma_{IF}^2) \tag{4.2}$$

where $\sigma_{IF}^2 = N_0 \cdot f_s/2$.

In practice, there will be always more than one visible satellite available, due to the quasi-orthogonality of the spreading codes (PRNs), the receiver can deal with each visible satellite signal independently which is the reason why we only focus on one single satellite in 4.1.

In order to cope with the uncertainty of phase information, the locally generated signal always contains In-phase (I) and Quadrature (Q) components. Its corresponding complex mathematical expression is

$$y[n] = A \cdot c(nT_s - \tau_L)s_b(nT_s - \tau_L) \cdot \exp[2\pi(f_{IF} + f_{d,L})nT_s + \varphi_L] \tag{4.3}$$

where τ_L and $f_{d,L}$ are the estimates of code delay and Doppler frequency used in the local signal.

The incoming signal (4.1) is multiplied with the local one (4.3) and accumulated along every integration period T_d (point correlation). Neglecting the high-frequency terms and noise, which are almost filtered out by the integration, at the end of each accumulation time the output of this correlation operation can be written as a function of the residual delay, frequency and phase errors as [9]

$$Z(\Delta\tau,\Delta f,\Delta\varphi) = \frac{A}{2}R(\Delta\tau)\mathbf{Sinc}(\Delta f\pi T_d) \cdot e^{\Delta\varphi+\Delta f\pi T_d} \tag{4.4}$$

where T_d is the accumulation time, $R(\Delta\tau)$ is the code correlation function and the estimation errors are defined as

$$\begin{cases} \Delta\tau = \tau - \tau_L \\ \Delta f = f_d - f_{d,L} \\ \Delta\varphi = \varphi_0 - \varphi_L \end{cases} \tag{4.5}$$

It is important to note that the noise term in (4.1) will still keep the property of WGN even after the multiplication with the local signal (4.3). That is to

say

$$\tilde{\eta}[n] = \eta[n] \cdot y_L[n] \tag{4.6}$$

$$\tilde{\eta}[n] \sim (0,\sigma_{IF}^2) \tag{4.7}$$

This is due to the fact that the local spreading code is actually a pseudo-random sequence with the values in the set 1,-1.

4.2.2 Derivation of New FLL Discriminator

The new proposed discriminator utilizes the energy (i.e., the result of the accumulation operation at the correlation output) to determine the frequency error, similarly to a traditional DLL discriminator. The principle architecture is illustrated in Fig.4.1

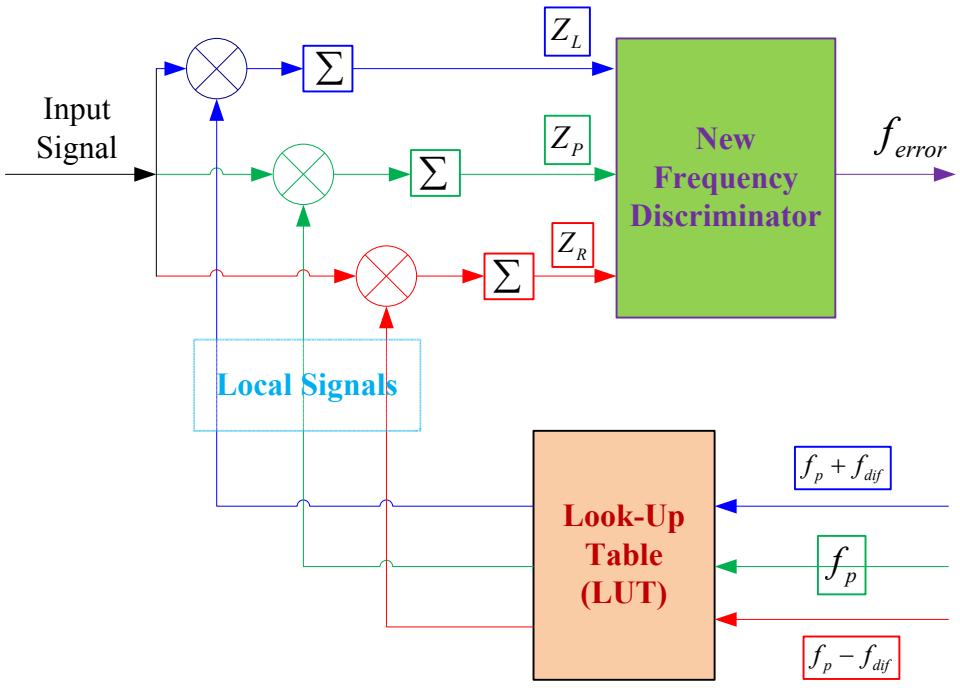

Figure 4.1: Signal processing architecture for the new FLL discriminator.

As shown in Fig.4.1 , the new discriminator needs three correlators which attempt to correlate the incoming signal with the carrier replicas at frequencies $f_P - f_{step}$ (left component), f_P (prompt component), $f_P + f_{step}$ (right

component) separately. represents the prompt frequency estimate while is the frequency difference between left/right and prompt components. Here in this chapter we set

$$f_{step} = \frac{2}{3T_d} \tag{4.8}$$

The new frequency discriminator computes the frequency error with the following simple rule

$$f_{error} = \frac{|Z_L| - |Z_R|}{|Z_L| + |Z_P| + |Z_R|} \cdot f_{step} \tag{4.9}$$

The rationale for this choice is derived as follows. We start from the identity

$$\mathbf{sin}(\theta - \frac{2\pi}{3}) + \mathbf{sin}(\theta) + \mathbf{sin}(\theta + \frac{2\pi}{3}) = 0 \tag{4.10}$$

then, setting $\theta = f_{error} \cdot \pi T_d$ and exploiting the choice $f_{step} = \frac{2}{3T_d} = \frac{2\pi}{2} \cdot \frac{1}{\pi T_d}$ we re-elaborate (4.10) in

$$\begin{aligned}(f_{error} - f_{step}) \cdot \frac{\mathbf{sin}(f_{error} \cdot \pi T_d - \frac{2\pi}{3})}{f_{error} \cdot \pi T_d - \frac{2\pi}{3}} + f_{error} \cdot \frac{\mathbf{sin}(f_{error} \cdot \pi T_d)}{f_{error} \cdot \pi T_d} \\ +(f_{error} - f_{step}) \cdot \frac{\mathbf{sin}(f_{error} \cdot \pi T_d + \frac{2\pi}{3})}{f_{error} \cdot \pi T_d + \frac{2\pi}{3}} = 0\end{aligned} \tag{4.11}$$

In addition, when

$$|f_{error}| \leq \frac{f_s tep}{2} \tag{4.12}$$

we can get

$$|Z_L| = \frac{A}{2} R(\Delta\tau) \frac{\mathbf{sin}(f_{error} \cdot \pi T_d - \frac{2\pi}{3})}{f_{error} \cdot \pi T_d - \frac{2\pi}{3}} \tag{4.13}$$

$$|Z_R| = \frac{A}{2} R(\Delta\tau) \frac{\mathbf{sin}(f_{error} \cdot \pi T_d + \frac{2\pi}{3})}{f_{error} \cdot \pi T_d + \frac{2\pi}{3}} \tag{4.14}$$

$$|Z_R| = \frac{A}{2} R(\Delta\tau) \frac{\mathbf{sin}(f_{error} \cdot \pi T_d)}{f_{error} \cdot \pi T_d} \tag{4.15}$$

Therefore, by substituting (4.13)-(4.15) into (4.11), (4.9) is obtained.

It is important to observe that in an ideal scenario where no noise is involved, (4.9) is independent from code delay error $\Delta\tau$ and signal amplitude A.

According to [9], we observe that this discriminator is an Maximum-Likelihood (ML) estimator when is close to zero. Even when is large, (4.9) still can perform closely to a ML estimator. It is worth stressing that the close-loop

frequency adjustment in the FLL works to drag f_{error} close to zero eventually [49], so that the condition for the ML estimation is almost always met. In this sense, we can get [9]

$$var\{f_{error}\} = \frac{12}{(2\pi)^2 \cdot \widetilde{SNR} \cdot f_s \cdot T_d^3} \tag{4.16}$$

where

$$\widetilde{SNR} = \frac{A^2 R^2(\Delta\tau)}{2\sigma_{IF}^2} \tag{4.17}$$

It is noted that when $R(\Delta\tau) = 1$, (4.16) is the Cramer-Rao Lower Bound (CRLB) on the frequency estimation error.

4.3 Comparison With Existing Architectures

As discussed above, the new discriminator (4.9) calculates the frequency error only exploiting a minimum period of data T_d while the traditional one needs at least two consecutive periods of data. To our best knowledge, in current available literature there is only one similar discriminator proposed based on energy [10], in which also only a minimum period of data is enough for one frequency error estimate.

In order to compare these two similar discriminators, here we indicate the method [10] as 'discriminator-R', and ours as 'discriminator-P'.

To guarantee fairness of comparison, the frequency step in discriminator-R is also set as in (4.8). Therefore, discriminator-R can be mathematically expressed as [10]

$$f_{error-R} = \frac{Z_L^2 - Z_R^2}{K_{df}} \tag{4.18}$$

where

$$\begin{aligned} K_{df} = {} & [A \cdot R(\Delta\tau)]^2 \pi T_d \cdot \mathbf{Sinc}(\frac{2\pi}{3}) \\ & \cdot \frac{\mathbf{sin}(\frac{2\pi}{3}) - (\frac{2\pi}{3})\mathbf{cos}(\frac{2\pi}{3})}{(\frac{2\pi}{3})^2} \end{aligned} \tag{4.19}$$

From (4.19) we observe that in discriminator-R the term $A \cdot R(\Delta\tau)$ has to be known in order to get a correct frequency error estimate which is the fatal drawback of this algorithm, while discriminator-P is independent of A and $\Delta\tau$ as discussed above.

As mentioned in introduction, this chapter mainly focuses on the new coming satellite systems, so the Galileo E1 OS signal model will be considered as a representative example in all the following simulations.

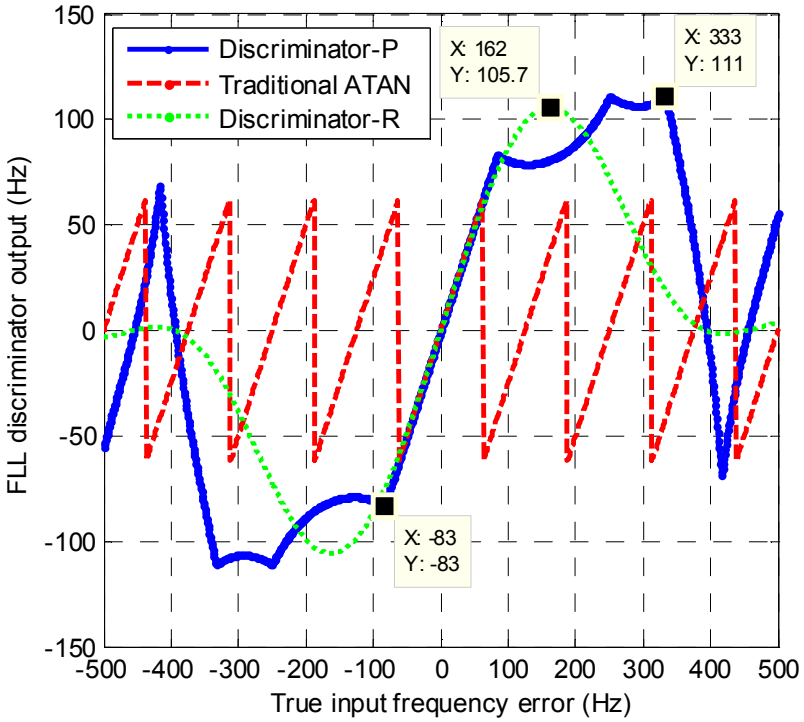

Figure 4.2: Comparison of the S-curves of three different FLL discriminators.

4.3.1 Curve Analysis

A first comparison of performance is based on the theoretical evaluation of the noise-free S-curve of the three considered discriminators (namely, discriminator-P, discriminator-R and the traditional ATAN), in order to evaluate their pull-in ranges, as shown in Fig.4.2. The integration time is set to 4 ms.

It is important to recall that in discriminator-R, we have to set A and $\Delta\tau$ as known; here for simplicity, we set $A = 1, \Delta\tau = 0$.

From Fig.4.2, we can see that discriminator-R and discriminator-P have nearly six times larger pull-in range as traditional arctangent discriminator, and discriminator-P has the widest linear range which is $-f_{step}/2, f_{step}/2$. From [10], it is known that discriminator-R involves approximation using Taylor's expansion, which is the reason why actually the strict linear range in discriminator-R is very small around zero. Besides that, discriminator-P has wider effective pull-in range than discriminator-R, as illustrated in Fig.4.2.

On the other hand, when noise is considered, as analyzed in section 4.2.2, discriminator-P can be treated as a ML estimator with the close-loop operation in FLL. On the contrary discriminator-R is a non-ML discriminator especially when carrier-to-noise density ratio is low [10].

We summarize our comparison results in Table.4.1, where we notice that the new proposed discriminator-P inherits the advantages of discriminator-R and traditional ATAN discriminator but avoids their weaknesses (marked in red in Table 4.1) at the same time.

Table 4.1: Comparison of three FLL discriminators in terms of different attributes

Type	**Discriminator-P**	**Discriminator-R**	**Traditional ATAN**
Effective Pull-in range	Large	Middle	Small
Accuracy	ML	Non-ML	ML
Need to know A and $\Delta\tau$	No	Yes (fatal drawback)	No
Minimum Length of input data	Single period	Single period	Two consecutive periods

4.3.2 Closed-loop Analysis

In order to test the validity of the new proposed discriminator in FLL, a conventional closed-loop architecture is set up in simulation, whose linear model is illustrated in Fig.4.3. The main parameters of the closed-loop simulations

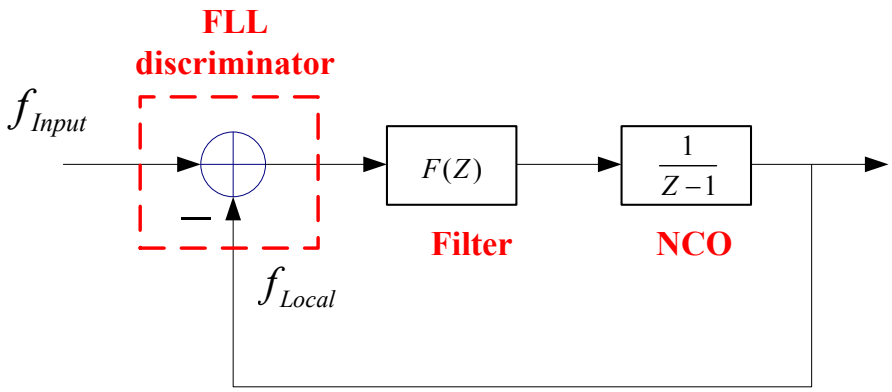

Figure 4.3: Block diagram of the linearized FLL.

are set as follows: initial frequency error $f_{error,ini} = 350Hz$, $C/N_0 = 35dBHz$, noise bandwidth $B = 3Hz$, signal amplitude $A = 1$, code delay error $\Delta\tau = 0$. A one-pole loop filter is used. The results are shown in Fig.4 and Fig.5.

Fig.4 compares the frequency estimation error, computed as the difference $f_{Input} - f_{Local}$ in the architecture of Fig.4.3, for the FLL in which the conventional arctangent discriminator, discriminator-P and discriminator-R are implemented. It can be seen that the ATAN discriminator suffers from its far narrower pull-in range compared to the other two, while discriminator-P converges faster than discriminator-R thanks to its perfectly linear S-curve. In Fig.5 we compare the discriminator outputs for the P and R rules: it can be observed how discriminator-P has lower variance than discriminator-R, which proves the aforementioned accuracy term in Table.4.1. As analyzed above, in low C/N_0 scenarios discriminator-P can be more accurate than discriminator-R. Although the advantage could not appear obvious or significant in traditional closed-loop FLL, it is arguable that it become more

important in another architecture named quasi-open loop [48], in terms of final frequency estimate accuracy.

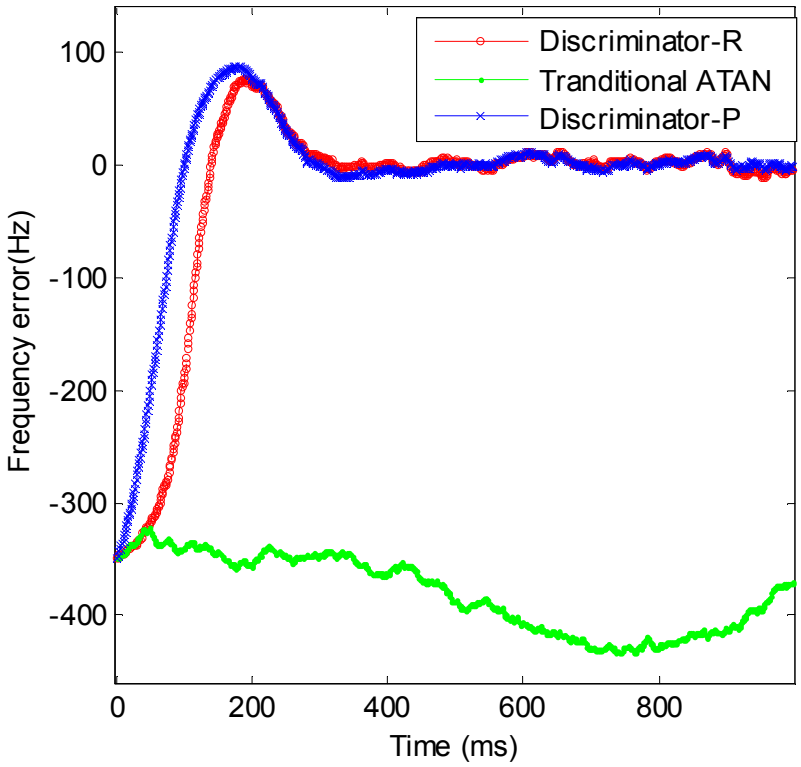

Figure 4.4: Frequency estimation error ($f_{Input} - f_{Local}$) in the FLL, achieved with the three discriminators (large initial estimation error, $C/N0 = 35dBHz$).

4.4 Combination of Pilot and Data Channels

With the advent of new GNSS, such as Galileo, Compass and the modernized GPS, composite GNSS signals are introduced to guarantee coexistence and interoperability, such as Galileo E1 OS signal which contains data (B channel) and pilot (C channel) components. B channel carries the navigation message while C channel is used for determining accurate pseudoranges between the satellites and receivers. References [45, 47] propose different algorithms to

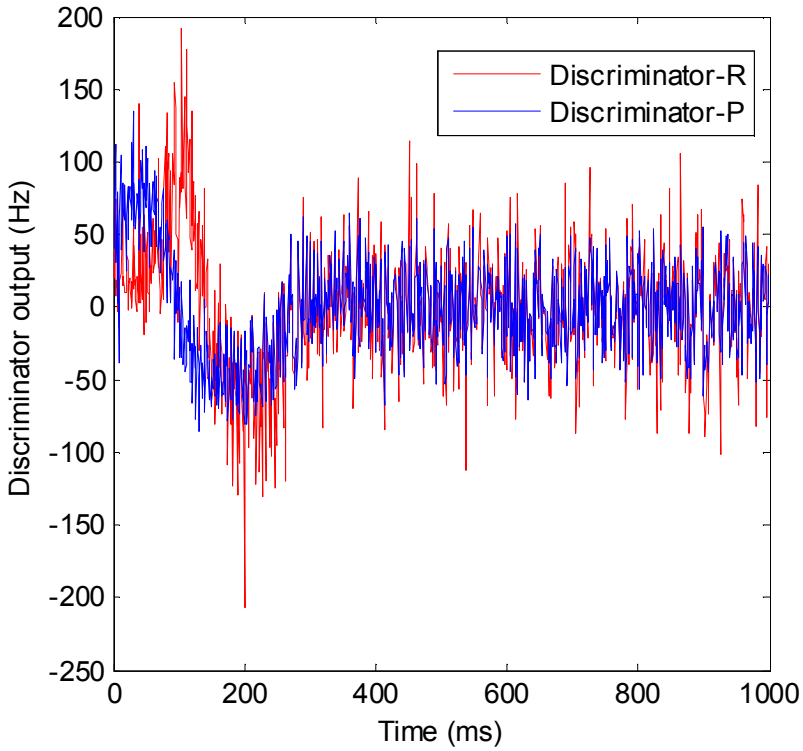

Figure 4.5: Discriminator's output for the two energy-based rules, in the FLL with $C/N0 = 35dBHz$.

combine these two channels to improve the receiver performance in signal acquisition. Considering the property of new proposed FLL discriminator, we adopt the coherent combination approach used in [45] to improve the accuracy of our new discriminator, as illustrated in Fig.4.6.

The Galileo E1 OS signal is modulated with a CBOC (composite binary offset carrier) scheme, which consist of a composition of BOC(1,1) and BOC(6,1) modulations. Because 90% of the transmitted power is devoted to BOC(1,1), here BOC(6,1) is ignored for simplicity, so that the input signal (4.1) can be changed to

$$y[n] = A\cdot((C_B(nT_s-\tau)d(nT_s-\tau)+(C_c(nT_s-\tau)c_{2nd}(nT_s-\tau))\cdot\cos[2\pi(f_{IF}+f_d)nT_s+\varphi_0]+\eta[n]$$

where $C_B(nT_s-\tau)$ and $C_c(nT_s-\tau)$ are the primary PRN codes with corresponding subcarriers, $d(nT_s-\tau)$ is the navigation message while $c_{2nd}(nT_s-\tau)$

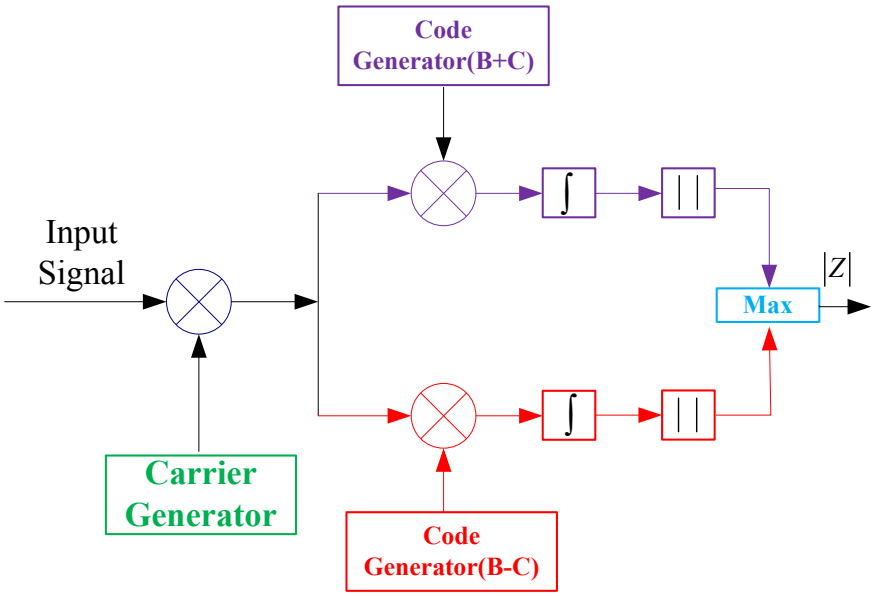

Figure 4.6: Coherent combination of data and pilot channels.

is the secondary code in pilot channel with the same chip period as $d(nT_s-\tau)$.

Denote $C_T = (C_B(nT_s-\tau)d(nT_s-\tau) + (C_c(nT_s-\tau)c_{2nd}(nT_s-\tau)$, Then

$$C_T = \begin{cases} \text{sign}(d(nT_s-\tau))[C_B(nT_s-\tau) + C_c(nT_s-\tau)] \\ or \\ \text{sign}(d(nT_s-\tau))[C_B(nT_s-\tau) - C_c(nT_s-\tau)] \end{cases} \tag{4.20}$$

Due to the sign uncertainty of $d(nT_s-\tau)$ and $c_{2nd}(nT_s-\tau)$. The scheme in Fig.4.6 assures that the effective part of the accumulation result can be expressed as

$$Z = AR(\Delta\tau)\mathbf{Sinc}(\Delta f\pi T_d)\cdot e^{\Delta\varphi+\Delta f\pi T_d} \tag{4.21}$$

which is twice as large as (4.4).

As far as noise term is considered, in Fig.4.6 we can observe that noise term $\eta[n]$ is multiplied with the composite local code (B+C) or (B-C), so there are two parts in the new combined noise term $\tilde{\eta}[n]$

$$\tilde{\eta}[n] = \begin{cases} \eta_B[n] + \eta_c[n] \\ or \\ \eta_B[n] - \eta_c[n] \end{cases} \tag{4.22}$$

As mentioned before, $\eta_B[n]$ and $\eta_c[n]$ still follow the WGN property of $\eta[n]$ in the input signal, so

$$\eta_B[n] \sim (0,\sigma_{IF}^2) \tag{4.23}$$

$$\eta_C[n] \sim (0,\sigma_{IF}^2) \tag{4.24}$$

and, since $C_B(nT_s - \tau)$ and $C_C(nT_s - \tau)$ are uncorrelated, it is clear that

$$\tilde{\eta}[n] \sim (0,2\sigma_{IF}^2) \tag{4.25}$$

Therefore the new equivalent carrier-to-noise ratio based on the structure in Fig.4.6 can be calculated as

$$\widehat{SNR} = \frac{(2A)^2}{2 \cdot 2\sigma_{IF}^2} = 2 \cdot \frac{A^2}{2\sigma_{IF}^2} \tag{4.26}$$

which is twice as large as the previous SNR in case where only one channel is used.

Additionally, from 4.16 we can learn that the variance of frequency error will be decreased by 50% and the corresponding root-mean-square error (RMSE) of new FLL discriminator will be decreased by 30%.

4.5 Conclusion

In this chapter, in order to deal with the changes introduced in the new coming-up GNSS system, a new FLL discriminator based on energy, noted as discriminator-P is proposed, which can solve the problem of frequent data-transition by using the minimum period of data and broaden the pull-in range to six times larger as the traditional arctangent discriminator. At the same time, the derivation is also presented. Compared with a similar algorithm in [10], noted as discriminator-R, discriminator-P overcomes the fatal disadvantage of the previous one, that requires the knowledge of signal amplitude A and code delay $\Delta\tau$. At the same time, discriminator-P has more

effective pull-in range and more accurate estimate in low C/N_0 scenarios. In a word, the new proposed discriminator-P inherits the merits of traditional ATAN and discriminator-R but discards the drawbacks at the same time. Last but not least, considering the composite GNSS signal such as E1 OS signal, coherent combination of pilot and data channels is also adopted to improve the estimate accuracy by using full power of the transmitted power, the corresponding RMSE of frequency estimate can be decreased by 30%.

Chapter 5

The Practical Implementation and Analysis of Kalman Filter Based Tracking Loop

5.1 Introduction

The primary function of a general Global Navigation Satellite System (GNSS) receiver is to achieve the synchronization between the incoming satellite signal and its 'local' replica generated in the receiver, in order to decode the navigation message and be able to compute the final navigation solution. This process involves four logical stages in the receiver, namely acquisition, tracking, data demodulation and Position-Velocity-Time (PVT) calculation [1]. Particularly, in the conventional tracking architecture, the local replica of the signal is kept synchronized to the received signal by two different Numerically Controlled Oscillators (NCOs) [4]: one is used to refine the carrier frequency and phase estimates (Frequency/Phase Lock Loop, FLL/PLL) and the other to adjust the code delay (Delay Lock Loop, DLL). These loops work simultaneously to maintain the local signal synchronized with the incoming signal.

Thanks to the rapid development of the digital processors, advanced and innovative algorithms have been proposed recently to be used in software-based GNSS receivers. Among the new approaches, the application of Kalman Filter (KF) within the tracking stage is getting more and more attractive in the GNSS field [21]. For example, in [13] the authors proposed the usage of Kalman filter in an ultra-tight GPS/INS (Inertial Navigation System) integration which couples the tracking of different satellites via the estimated position and velocity.

In case of a GPS stand-alone receiver architecture (i.e., without any coupling with other sensors, such as INS), two main kinds of Kalman filters for signal tracking are proposed in the literature, according to the different measurement models used in the filter's design: one is the linear-KF which uses the discriminator outputs of both the PLL/FLL and DLL as measurements, respectively [14], whereas the second one is the Extented Kalman Filter (EKF) that directly uses the baseband In-phase (I) and Quadrature-phase (Q) output of the correlators as measurements inside the tracking loops [13]. Some work has been done in the past aimed at comparing the EKF-based or linear KF-based tracking loops with the traditional tracking architecture: in [21] the authors developed a method to compute the equivalent noise bandwidth when a linear-KF is used within the PLL module and such bandwidth has been compared with that of a traditional PLL in order to have a metric to evaluate the benefits of the KF. In [22, 12] the performance of the equivalent PLL based on the EKF has been evaluated in terms of steady-state response to both thermal noise and signal dynamics, and compared with the one obtained through a traditional PLL. Eventually, in [13] three KF-based tracking loop implementations, which use different system and measurement models, have been investigated with particular emphasis given to the carrier phase estimation.

However, from the previous literature there is no clear answer on how to update the NCO phases and frequency at each epoch, and usually the designer

is left free to choose if to modify just the phase rate or both the phase and frequency. Moreover, the accuracy of the PVT solution strongly depends on this choice and this aspect has never been analyzed in details so far, according to the writers' opinion. Besides that, the influence of EKF or linear KF-based tracking loop on the accuracy of PVT is seldom investigated especially in real scenarios. Therefore this section first tries to clarify the two aforementioned issues.

On the other side, less attention has been given to the in-depth theoretical analysis of the KF-based tracking loop itself and KF tuning. According to the writer's knowledge, typical analysis results can be available in [21]-[23]. In [21] the Kalman system is analyzed by simply comparing its equivalent noise bandwidth with the traditional tracking loop only in steady state. In [22] an experimental methodology is proposed to decide the equivalent PLL for a given EKF-based tracking loop. Furthermore, in [21] the authors offer a more comprehensive and sensible analysis, comparing the discrete-time domain expressions of a traditional second-order PLL and KF system model and deriving the mathematical relationships between them. However, [21] considers only two states in the KF model, and an approximated observation matrix which seem limiting the effective contribution to situations in which the integration time is very small (like a few milliseconds) or the frequency error (and frequency rate error) is close to zero; in addition, the values of initial error covariance, process noise covariance and measurement noise covariance are set in an empirical way.

Therefore, in the second part of this section, in order to overcome the aforementioned issues, a new approach is proposed to link the KF-based tracking loop and the traditional one. This allows us to derive a detailed mathematical description that gives better insight of such new tracking loop design and a clear understanding of the benefits gained by the KF-based tracking loop.

This work is organized as follows: in Section 5.2 we give an overview of the design of a tracking loops based on an EKF strategy, followed by an explicit

statement of the NCO update rules; in Section 5.3, we present the overall architecture necessary to implement the enhanced tracking loop, including the solutions to determine certain parameters needed by the EKF. In Section 5.4 the EKF-based architecture is tested in a real scenario and its performance is compared on one hand with the traditional tracking architecture implemented in the same software receiver, and on the other hand with two commercial receivers. Furthermore, 5.5 gives the in-depth analysis of KF-based tracking loop, and the relationship between KF-based tracking loop and traditional one is compared in mathematical models. Eventually, Section 5.6 draws the conclusions.

5.2 EKF-based tracking loop

In this section we give a brief description of the system and measurement model of the EKF adopted in the tracking loop, based on [13, 22] (subsection 5.2.1). Then, in subsection 5.2.2, we discuss the methodology to update the frequency and phase of the NCOs, necessary to correctly implement the EKF-based signal tracking.

5.2.1 An overview of the EKF tracking loop

When an EKF-based tracking loop is adopted, the correlator outputs are directly used as measurements in a proper extended Kalman filter architecture that estimates the following state parameters:

- amplitude, A (dimensionless),
- code phase error, $\delta\tau$ (unit: chips),
- carrier phase error, $\delta\theta$ (unit: radians),
- carrier frequency error, δf (unit: Hz),

- carrier frequency rate error, $\delta\alpha$ (unit: Hz/s).

They are used to generate the local replica of the signal in the receiver. A general scheme of an EKF tracking loop is depicted in Fig.5.1.

The system model can be written as follows [13, 22]

$$\begin{aligned}\begin{bmatrix}\dot{A}\\ \dot{\delta\tau}\\ \dot{\delta\theta}\\ \dot{\delta f}\\ \dot{\delta\alpha}\end{bmatrix} &= \begin{bmatrix}0&0&0&0&0\\0&0&0&\beta&0\\0&0&0&2\pi&0\\0&0&0&0&1\\0&0&0&0&0\end{bmatrix}\cdot\begin{bmatrix}A\\ \delta\tau\\ \delta\theta\\ \delta f\\ \delta\alpha\end{bmatrix}\\ &+\begin{bmatrix}1&0&0&0&0\\0&1&\beta&0&0\\0&0&1&0&0\\0&0&0&1&0\\0&0&0&0&1\end{bmatrix}\cdot\begin{bmatrix}W_A\\ W_{code}\\ W_{clock}\\ W_{freq}\\ W_{acc}\end{bmatrix}\end{aligned} \tag{5.1}$$

where the vector $\mathbf{W} = \begin{bmatrix}W_A & W_{code} & W_{clock} & W_{freq} & W_{acc}\end{bmatrix}^{\dagger}$ represents the process noises of the signal amplitude, code phase error (e.g. caused by multipath effects), clock bias, clock drift and frequency rate error; the superscript † indicates the transpose operator. The statistical characterization of the noise variance can be found in [22]. The coefficient β is used to convert the units of cycles to units of chips (e.g., for GPS L1 $\beta = \frac{1}{1540}$, where 1540 is the number of cycles of the L1 carrier, $f_{L1} = 1575.45$ MHz, in one chip period, 1/1023 ms). It can be noticed that the system model (5.1) is an error-state model [23].

The measurement model can be written as

$$\mathbf{Z} = [I_P\ I_E\ I_L\ Q_P\ Q_E\ Q_L]^{\dagger} \tag{5.2}$$

where $I_\bullet$ and $Q_\bullet$ stand for In-phase and Quad-phase correlator outputs, respectively, while the indices P, E and L represent the 'prompt', 'early', and

'late' components. In formulae, the $I_\bullet$ and $Q_\bullet$ terms can be stated according to [40] as:

$$\begin{aligned} I_\bullet &= \frac{A}{2}\,\mathrm{R}(\delta\tau - \Delta_\bullet)\,\mathrm{Sinc}(\pi\,\delta f\,T)\cos(\overline{\delta\varphi}) \;+\; n_{I_\bullet} \\ Q_\bullet &= \frac{A}{2}\,\mathrm{R}(\delta\tau - \Delta_\bullet)\,\mathrm{Sinc}(\pi\,\delta f\,T)\sin(\overline{\delta\varphi}) \;+\; n_{Q_\bullet} \end{aligned} \tag{5.3}$$

where $\mathrm{R}(\cdot)$ represents the normalized code autocorrelation function; $\Delta_\bullet$ is the spacing between the prompt and the early/late correlators; T is the integration time; $\overline{\delta\varphi}$ is the average phase error which can be expressed as [13]:

$$\overline{\delta\varphi} = \delta\theta + \delta f\,\frac{T}{2} + \delta\alpha\,\frac{T^2}{6} \tag{5.4}$$

where $\delta\theta$ is the true phase error as stated in (5.1). Finally $n_{I_\bullet}$, $n_{Q_\bullet}$ are the noise components at the output of the In-phase and Quad-phase correlators. It is important to stress that in a traditional PLL architecture, the PLL discriminator actually measures the average phase error $\overline{\delta\varphi}$ instead of the true phase error $\delta\theta$.

Finally, the noise variance in observations can be computed as a function of the carrier-to-noise density ratio C/N_0, as reported in [13]:

$$\sigma^2_{n_{I_P}} = \sigma^2_{n_{Q_P}} = \frac{C}{2 \cdot 10^{\frac{(C/N_0)|_{\mathrm{dBHz}}}{10}} \cdot T} \tag{5.5}$$

for the P correlator, where C is the signal power (i.e. $C = \frac{A^2}{2}$), and $(C/N_0)|_{\mathrm{dBHz}}$ is expressed in dBHz. At the same time, the noise variance of the early and late components can be written as shown in [12]:

$$\sigma^2_{n_{I_E}} = \sigma^2_{n_{I_L}} = \sigma^2_{n_{Q_E}} = \sigma^2_{n_{Q_L}} = \mathrm{R}(\Delta)\sigma^2_{n_{I_P}} \tag{5.6}$$

Thus, (5.2), (5.3) represent the measurement model of the EKF that will be used in our software receiver, while the system model is reported in (5.1). All the details related to the discrete time conversion of the transition matrix and the process noise covariance can be found in[29].

5.2.2 NCO update

The NCO update strategy is a key part of the tracking loop as it influences the final accuracy of the locally generated signals. In a typical PLL + DLL tracking architecture [1], each NCO is defined by two states (i.e., phase and frequency) and drives the local generator for either the carrier signal or the spreading code. Therefore in a GNSS receiver we can model a four-state control input for the NCO updates

$$\mathbf{X}_{NCO} = [f_{carr}\ \theta_{carr}\ f_{code}\ \theta_{code}]^{\dagger} \tag{5.7}$$

where the subscripts '*carr*' and '*code*' refer to the states of the carrier and code generators, respectively.

In most of the traditional tracking schemes, the NCO phases are not directly modified at each epoch, but rather the phase rates (i.e. frequency) are updated. This is referred to as a rate-only update NCO [21]. This means that only the frequency of each NCO is directly modified based on the discriminator outputs[50]. However, theoretically, all the four NCO states stated in (5.7) could be modified at the same time [21]. As a consequence, we have rewritten the NCO updates in order to take into consideration all the four states described above.

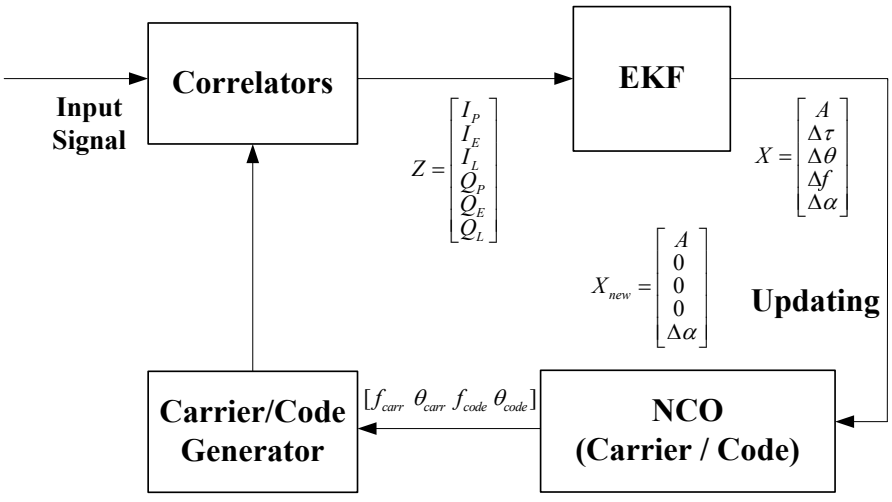

Figure 5.1: The structure of the EKF-based tracking loop.

As illustrated in Fig.5.1, at the end of each measurements update in the EKF, we can get the new state vector as:

$$\mathbf{X}_k = [A \ \delta\tau \ \delta\theta \ \delta f \ \delta\alpha]_k^\dagger \tag{5.8}$$

where k is the discrete epoch index in the tracking loop. Then the update rule of the carrier and code NCOs can be written as:

Carrier NCO update rule:

$$\begin{cases} f_{carr_k} = f_{carr_{k-1}} + \mathbf{X}_k(4) \\ \theta_{carr_k} = \left(\theta_{carr_{k-1}} + \mathbf{X}_k(3)\right) \bmod (2\pi) \end{cases} \tag{5.9}$$

where $\mathbf{X}_k(m)$ is the m-th entry of the vector $\mathbf{X}_k$; then,

Code NCO update rule:

$$\begin{cases} f_{code_k} = f_{code_{fix}} + \beta f_{dop_k} \\ \theta_{code_k} = \theta_{code_{k-1}} + \mathbf{X}_k(2) \end{cases} \tag{5.10}$$

where $f_{code_{fix}} = 1.023MHz$, f_{dop_k} is the Doppler frequency estimate at the epoch k, i.e.,

$$f_{dop_k} = f_{carr_k} - f_{IF} \tag{5.11}$$

where f_{IF} is the intermediate frequency of the incoming signal at the output of the front-end.

Furthermore, after every NCO update, the state vector has to be reset as follows:

$$\mathbf{X}_{new_k} = [A \ 0 \ 0 \ 0 \ \delta\alpha]_k^\dagger \tag{5.12}$$

which will be used as the initial state vector in the next iteration of EKF. The reason for the resetting rule (5.12) is the type of system model (5.1) which is error-state: at the end of each measurement update, the parameters of the NCO are corrected by the state vector, and then the corresponding values of the error-state vector have to be set to zero. This operation will not cause any obvious jump in the NCO output as the errors are usually very small in steady-state process, even if some interference happens causing the spurious error, we would reject it rather than let it corrupt the filter computation.

5.2.3 Tuning the noise covariances

The tuning of the system noise covariance matrix $\mathbf{Q}$ and measurement noise covariance matrix $\mathbf{R}$ plays an important role on the performance in EKF/KF-based tracking loop [29].

From [51], we can perceive the Kalman filter as a deterministic filter with a time-varying bandwidth determined by Kalman gain ($\mathbf{K}_k$). Therefore, at the initialization of EKF, the state error covariance ($\mathbf{P}_k^-$) should be set much larger than $\mathbf{Q}$ to give the system a corresponding larger bandwidth; then, as the Kalman filter converges, the final steady-state performance depends on $\mathbf{QR}^-$. In this work, $\mathbf{Q}$ conforms with the models explained in (5.1)2.12.1, and $\mathbf{R}$ can be determined by (5.5) and (5.6).

5.3 Practical implementation issues of the EKF tracking loop

In the past, the EKF-based tracking loop has been compared with the traditional one in terms of carrier and code phase estimation accuracy and equivalent noise bandwidth [13, 22, 12]. However, typically, certain implementation issues remain open, although they appear to be fundamental for achieving good performance in real and dynamic tracking conditions.

Fig. 5.2 illustrates the overall logical architecture that is essential to implement a correct EKF-tracking loop. In particular, we are going to discuss hereafter the two non-standard blocks indicated as 'Preparation-For-Tracking' (PFT) and 'parameter estimation' (EST).

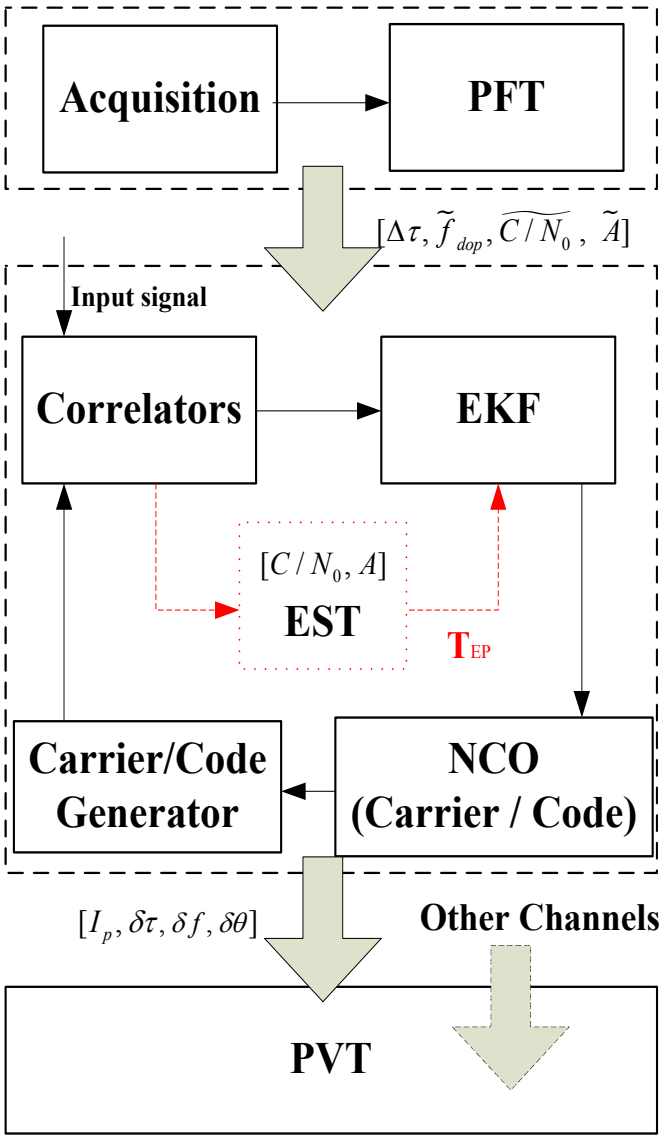

Figure 5.2: Logical structure of a receiver with EKF-based tracking.

5.3.1 Acquisition refinement and Preparation-For-Tracking (PFT)

In order to initialize the EKF-based tracking loop, besides the estimates of code delay $\Delta\tau$ and Doppler frequency f_{dop} from the traditional acquisition process, two additional parameters, carrier-to-noise density ratio C/N_0 and signal amplitude A, have to be computed. For the better estimates of C/N_0

and A, the f_{dop} from acquisition has to be refined first in a fast way. Additionally, a more accurate Doppler frequency estimate can decrease the possibility of false frequency-lock case in the following EKF-based tracking loop especially in the case of weak signals.

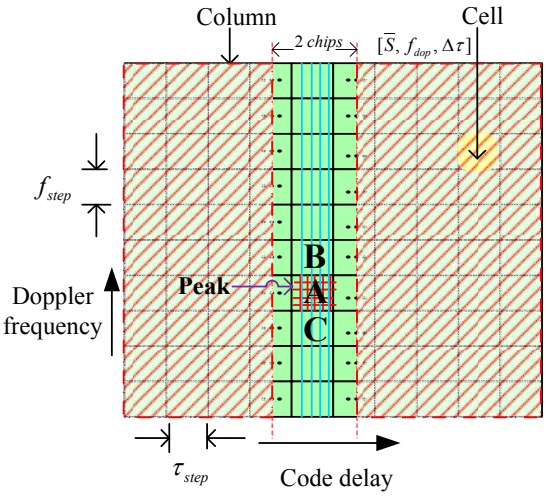

Figure 5.3: Two-dimensional acquisition.

The first task of PFT is to refine the Doppler frequency, by using, for instance, the method proposed in [9]. A by-product of this Doppler refinement method is the possibility to obtain an initial and precise estimation of C/N_0, which will be fed into the EKF tracking loop through (5.5) and (5.6). Starting from the approach in [52], the C/N_0 can be evaluated as:

$$\widetilde{C/N_0} = 10\log\left(\frac{S_P^2 - \overline{S}_N^2}{\mathrm{Sinc}^2\left(\left|\widetilde{f}_{dop} - \overline{f}_P\right|\pi T\right)\overline{S}_N^2}\cdot\frac{1}{T}\right) \tag{5.13}$$

where S_P is the amplitude of the cross-ambiguity function (CAF) accumulated in the acquisition search space in correspondence of the Peak cell (as shown in Fig. 5.3 for better clarity), $\overline{f}_P$ is the Doppler frequency associated to the peak cell, $\widetilde{f}_{dop}$ is the refined Doppler frequency estimate, and $\overline{S}_N^2$ is the average noise power computed from the cells which are 1-chip away from the search space column where the peak is found (i.e., all the grey cells in Fig. 5.3). $\overline{S}_N^2$ is determined as

$$\overline{S}_N^2 = \frac{1}{M}\sum_{m=1}^{M} S_m^2 \tag{5.14}$$

where M is the number of cells used for the average.

At the same time, the PFT block is in charge of evaluating the amplitude of the satellite's incoming signal, which, following again the framework drawn in [52], is

$$\widetilde{A} = \frac{2S_P}{\text{Sinc}\left(\left|\widetilde{f}_{dop} - \overline{f}_P\right| \pi T\right)} \tag{5.15}$$

Eventually, these three estimates (i.e.$[\widetilde{f}_{dop}, \widetilde{C/N_0}, \widetilde{A}]$) and $\Delta\tau$ will be used to initialize the EKF-based tracking loop.

5.3.2 Tracking stage

In order to keep the tracking loop working properly, an additional module (indicated with EST in Fig. 5.2) is necessary to continuously update the C/N_0 estimate and the amplitude A of the incoming signal to refine the estimate of the measurement noise variance. It is worth noticing that the C/N_0 estimate is a typical function in any GNSS receiver, so its implementation is not an additional burden for the receiver.

The EST block can work at a lower rate (e.g., with an estimation period $T_{EP} = 0.1 - 1$ s) than the EKF's update rate (e.g., with an epoch duration of $1 - 20$ ms).

According to [52], the Moment Method can be used for C/N_0 estimation, starting from an estimate of the post-correlation the signal-to-noise ratio (SNR). Then the C/N_0 in dBHz can be easily computed as:

$$C/N_0 = 10 \cdot \log\left(SNR \cdot B_{eq}\right) \quad \text{(dBHz)} \tag{5.16}$$

where B_{eq} is the correlators' equivalent noise bandwidth and it is usually set as $B_{eq} = \frac{1}{T}$.

As far as the amplitude A is concerned, its update can be done at the same low rate $1/T_{EP}$ of the EST block instead of the EKF rate. In this work, we set $T_{EP} = 100$ ms.

5.4 Performance assessment of the receiver with EKF-based tracking

As mentioned before, in order to test the advantage of the new EKF-based tracking loop, we first insert it in a simple software receiver architecture which obtains the sequence of PVT estimates by resolving a sequence of one-shot Least-Squares (LS) problems [1, 4, 43]. The receiver is then fed by datasets collected during dynamic trials on board of a car. The PVT results are then compared with those obtained by the same receiver with a traditional tracking loop [43]. Additionally, these PVT results are compared with those provided by two commercial receivers, namely a professional Septentrio PolaRx2e@ and a mass-market Ublox LEA-5T.

5.4.1 PVT estimation performance

Several tests have been carried out with real data collected in dynamic scenarios, in order to have an exhaustive understanding of the performance of the EKF-based receiver. In particular the navigation solution provided by the professional receiver is considered as the reference one.

First, in Fig.5.4 we show the estimated trajectory of a car equipped with the two commercial receivers, which can log their output data, and a data grabber which stores raw data from the front-end to allow post-processing in the software receiver. It can be seen that the trajectory estimated by the EKF-based receiver is very close to that of the two commercial receivers, while the positioning result from the traditional tracking architecture followed by a LS PVT estimation has significant variance compared to the other trajectories. As it is likely that the commercial receivers implement some smoothing procedure on the PVT solution at least (e.g., a Kalman filter approach to compute the PVT, [29]), we can conclude that the EKF approach moved to the tracking loop, followed by a simple LS approach for PVT computation, achieves

almost the same PVT performance as a PVT smoothing approach. This is a consequence of the fact that the EKF-based tracking loop, when carefully fed with an accurate estimate of the necessary noise statistics, can achieve smoother and more accurate estimates of Doppler frequency and code delay than the traditional tracking loops, allowing the computation of a smoother and more accurate trajectory. Although the observation of the enhanced performance of the EKF-based tracking was already stated for example in [22], its effect on the PVT estimates was not equivalently clear so far.

The EKF-based tracking architecture is demonstrated here to achieve the same accuracy in PVT as an existing commercial receiver. Nonetheless, this architecture shows a distinctive feature: it allows to move *complexity* from the PVT stage to the tracking stage of the receiver; and, together with complexity, it also moves the issue of *accuracy* and *stability* to the tracking stage, since the estimates of the EKF-based tracking stages are significantly more stable than those of a traditional PLL-DLL tracking loop. This is an important feature for those applications that require an "external PVT solution, i.e., a PVT computed by a module external to the GNSS receiver. Such an external module typically takes as input not only the pseudoranges computed by one o more GNSS receivers stand-alone, but also the measurements from other sensors, such as odometers, laser scanners, inertial navigation systems, and so on, with the purpose of fusing data to improve accuracy and continuity, or to meet safety requirements by redundancy [53, 54]. Other such applications implementing an external PVT solution may need to take input from two or more GNSS receivers to implement an ad-hoc differential solution [55]: in such case the accuracy and stability of the carrier phase measurements produced by the GNSS modules is of the utmost importance to achieve the accuracy in attitude determination required by the specific application. This could be easily achieved if the signal tracking were implemented by an EKF.

In order to better and more quantitatively evaluate the PVT performance of the EKF-based tracking, we show in Fig. 5.5 the position error achieved

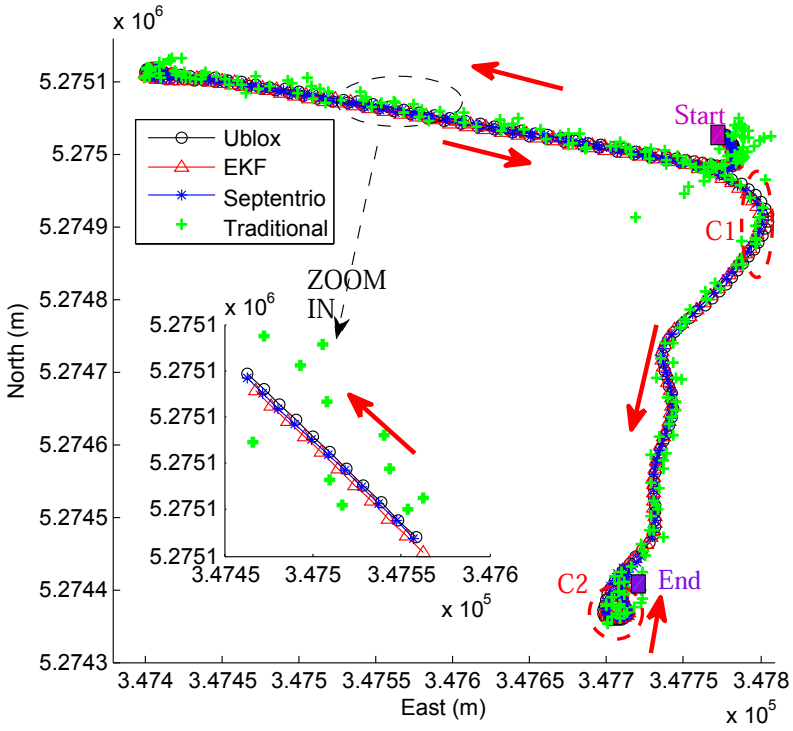

Figure 5.4: Example of a two dimensional car trajectory estimated by different receivers.

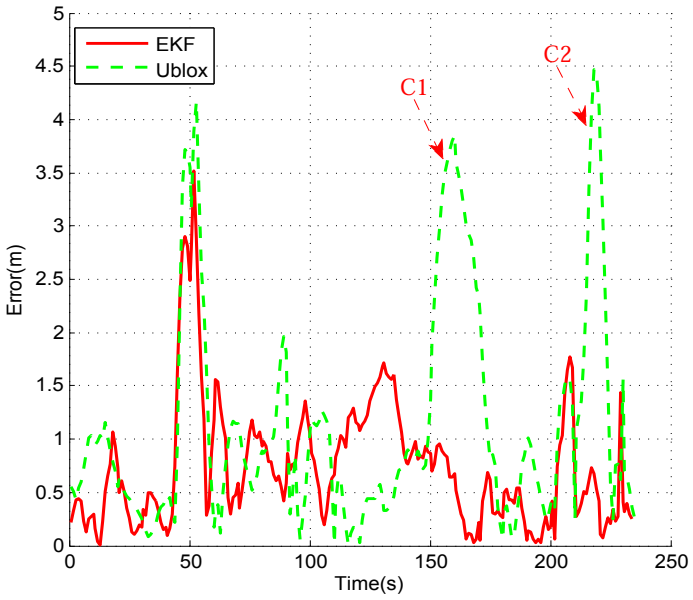

Figure 5.5: Position error in meters with respect to the reference trajectory, for the software EKF-based receiver and the Ublox receiver. The reference trajectory is that produced by the Septentrio PolaRx2e@ receiver.

by the EKF-based software receiver and by the Ublox receiver, with respect to the positions provided by the professional Septentrio receiver. We can see that errors are comparable almost everywhere, but in the case of major curves along the route (marked as C1 and C2 in Fig. 5.4 and Fig. 5.5), where the EKF-based receiver is more precise than the other one.

Furthermore, the comparison of the velocity estimates reported in Fig. 5.6 confirms that the EKF-based receiver can get much more accurate estimate of velocity compared with the traditional one, while it performs similarly to the LEA-5T.

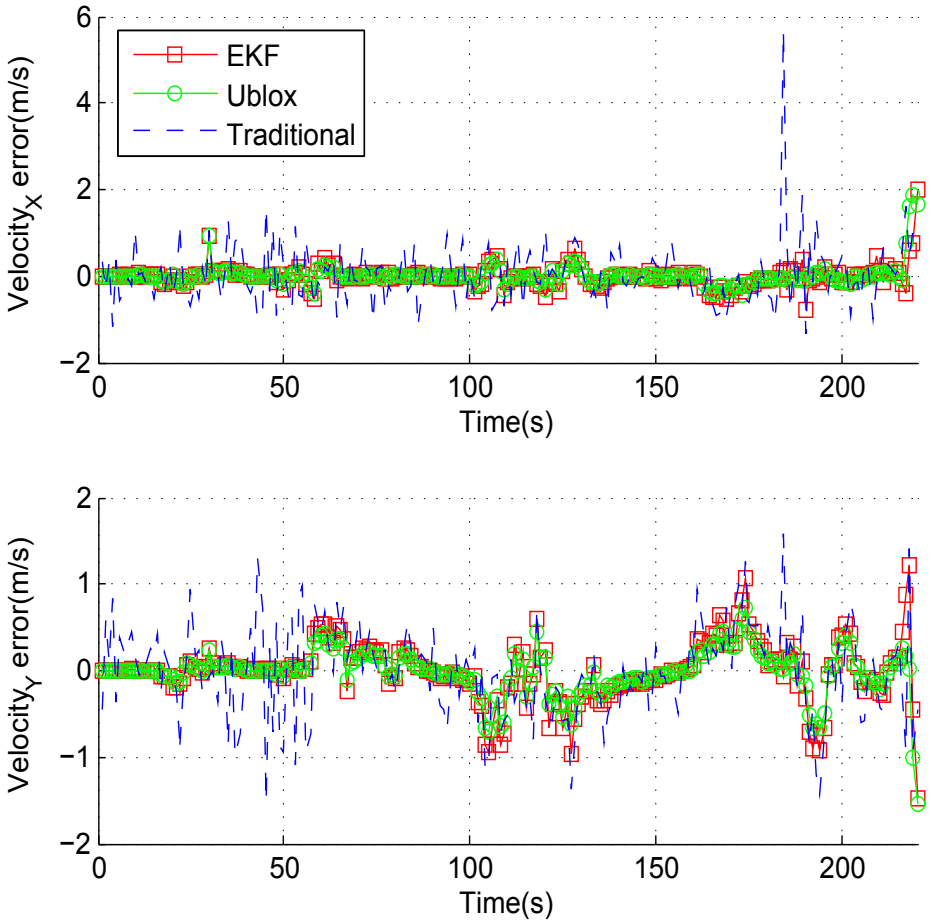

Figure 5.6: The velocity errors along the time considering Septentrio PolaRx2e@ as a reference.

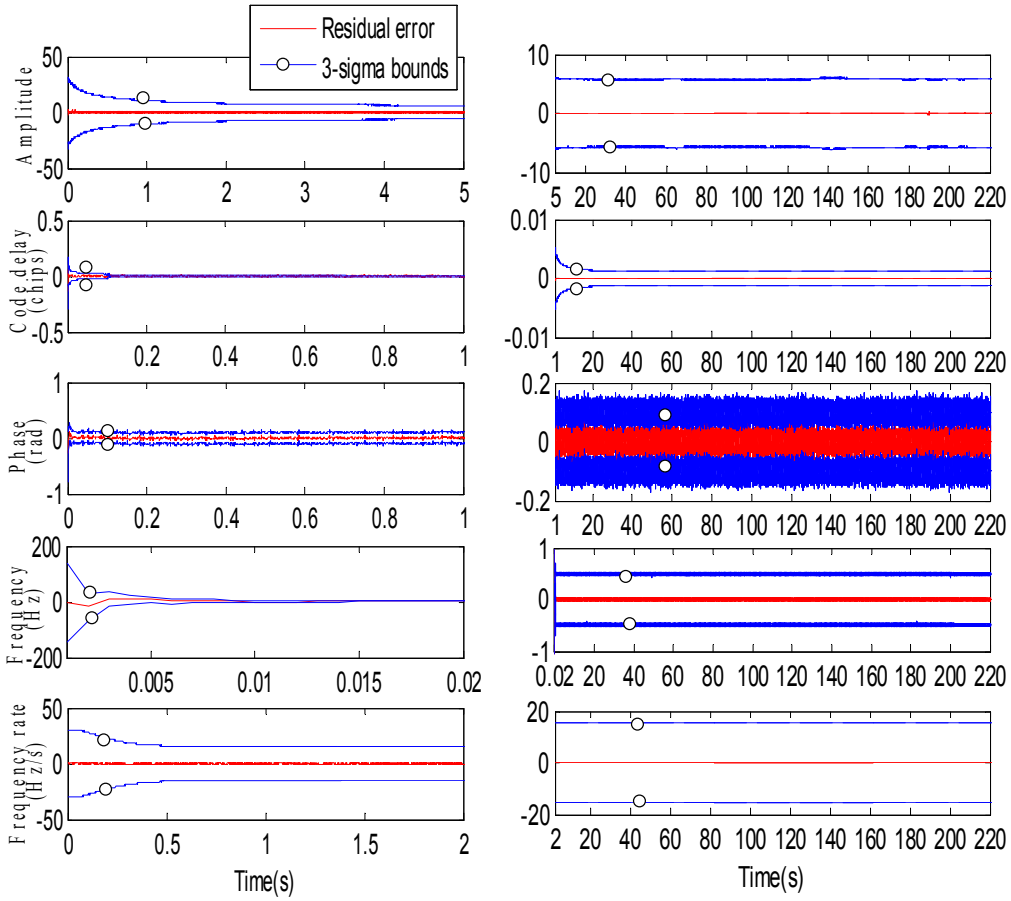

Figure 5.7: Residual error analysis of the five EKF tracking states: time evolution of the residual errors and 3σ confidence intervals computed along the path shown in Fig. 5.4. Left column: evolution during the transient interval. Right column: evolution in steady state.

5.4.2 Analysis of the residual errors

In order to proceed with the performance assessment of the EKF-based tracking loop, a residual error analysis [56] is used in this section.

The residual error vector $\tilde{\boldsymbol{\epsilon}}$ for the states $\mathbf{X}$ and its 3σ bound can be theoretically computed at each epoch k as [56]

$$\begin{cases} \tilde{\epsilon}_k = \mathbf{K}_k \left(\mathbf{Z}_k - \mathbf{h}(\mathbf{X}_k^-) \right) \\ \boldsymbol{\sigma}_k^2 = \mathrm{diag} \left((\mathbf{I} - \mathbf{K}_k \mathbf{H}_k) \, \mathbf{P}_k^- \right) \end{cases} \tag{5.17}$$

where $\mathbf{K}_k$ is the Kalman gain, $\mathbf{Z}_k$ is the measurement vector defined in (5.2), $\mathbf{h}(\mathbf{X}_k^-)$ is the observation function that relates the predicted states vector $\mathbf{X}_k^-$

with the observations, diag(·) means the diagonal of a matrix, $\mathbf{I}$ is the identity matrix, $\mathbf{H}_k$ is the Jacobian matrix of the measurement model and $\mathbf{P}_k^-$ is the predicted error covariance matrix.

As it can be observed in Fig. 5.7, the residual error and $\pm 3\sigma$ confidence interval for the code delay error $\delta\tau$ and the frequency error δf converge in a very short time. A wider confidence interval is shown for the fifth state (frequency error variation rate), this is because the covariance of the process noise component W_{acc} has to be set significantly bigger than the others in order to bear the uncertainty of this state especially in high dynamic cases.

5.5 Theoretical Analysis of the Kalman Filter-based Tracking Loop

As mentioned before, EKF adopts Taylor series to approximate the nonlinear relationship between the measurements and Kalman states while the measurement model in KF-based tracking loop is originally linear (under the hypothesis of linearity of the discriminators). For simplicity, we focus hereafter on the analysis of the linear KF-based tracking loop only.

5.5.1 Linear Kalman-based Tracking Loop

A linear KF-based tracking model is typically used to estimate the following parameters: Code phase error, $\Delta\tau$ (unit: chips), Carrier phase error,$\Delta\theta$ (unit: radians), Carrier frequency error,Δf (unit: Hz), Carrier frequency rate error, $\Delta\alpha$(unit: Hz/s).

The system model (error-state) in discrete-time domain can be described as:

$$\begin{bmatrix} \Delta\tau \\ \Delta\theta \\ \Delta f \\ \Delta\alpha \end{bmatrix}_{k+1} = \begin{bmatrix} 1 & 0 & \beta T & \frac{\beta T^2}{2} \\ 0 & 1 & 2\pi T & \pi T^2 \\ 0 & 0 & 1 & T \\ 0 & 0 & 0 & 1 \end{bmatrix} \begin{bmatrix} \Delta\tau \\ \Delta\theta \\ \Delta f \\ \Delta\alpha \end{bmatrix}_{k} + W_k \tag{5.18}$$

where the coefficient β is used to convert the units of cycles to units of chips (e.g. for GPS L1 $\beta = 1/1540$), T represents the integration time and W_k represents the process noise vector. The subscript $k \in \mathbb{N}$ indicates the discrete time instant.

In this KF-based vector tracking model, the outputs of two discriminators (i.e. carrier phase error discriminator and code phase error discriminator) are utilized as measurements, i.e., $\overline{\delta\varphi}$ (carrier phase error) and $\overline{\delta\tau}$ (code phase error). Then, the measurement model of a linear system can be written as:

$$\begin{bmatrix} \overline{\Delta\varphi} \\ \overline{\Delta\tau} \end{bmatrix}_{k+1} = \begin{bmatrix} 0 & 1 & -\pi T & \frac{\pi T^2}{3} \\ 1 & 0 & -\frac{\beta T}{2} & \frac{\pi T^2}{6} \end{bmatrix} \begin{bmatrix} \Delta\tau \\ \Delta\theta \\ \Delta f \\ \Delta\alpha \end{bmatrix}_{k+1} + V_k \tag{5.19}$$

where V_k is the measurement noise vector.

From the system model (5.18) and measurement model (5.19), we can observe that the whole system can be treated as the combination of two similar systems, namely code phase tracking loop and carrier tracking loop. Without loss of generality, we focus hereafter on the carrier-phase tracking loop, which is described by the following subsystem of equations:

$$\begin{bmatrix} \Delta\theta \\ \Delta f \\ \Delta\alpha \end{bmatrix}_{k+1} = \begin{bmatrix} 1 & -\pi T & \pi T^2 \\ 0 & 1 & T \\ 0 & 0 & 1 \end{bmatrix} \begin{bmatrix} \Delta\theta \\ \Delta f \\ \Delta\alpha \end{bmatrix}_{k} + W'_k$$

$$\overline{\delta\varphi}_{k+1} = \begin{bmatrix} 1 & -\pi T & \frac{\pi T^2}{3} \end{bmatrix} \begin{bmatrix} \Delta\theta \\ \Delta f \\ \Delta\alpha \end{bmatrix}_{k+1} + V'_k \tag{5.20}$$

The KF theory indicates that we can get an *a posteriori* state estimate $\hat{X}_k$ by incorporating the measurement Z_k in the predicted state (*a-priori* state estimate) [29] as follows:

$$\hat{X}_{k+1} = \hat{X}^-_{k+1} + K_{k+1} \cdot (Z_{k+1} - H_{k+1} \cdot \hat{X}^-_{k+1}) \tag{5.21}$$

where $\hat{X}^-_{k+1}$ is the *a priori* state estimate obtained by propagating in time the state estimate ($\hat{X}^-_{k+1} = A_{k+1} \cdot \hat{X}_k$, A_{k+1}= state propagation matrix), K_{k+1} is the so-called Kalman gain and H_{k+1} is the observation matrix, which connects the measurements with the current states.

Comparing (5.20) and (5.21) and defining

$$\begin{aligned}
&\hat{X}_k = [\Delta\theta, \Delta f, \Delta\alpha]^T_k \\
&Z_{k+1} = \text{Measurement at time (k+1)} \\
&H_{k+1} = [1 \;\; -\pi T \;\; \frac{\pi T^2}{3}] \\
&A_{k+1} = \begin{bmatrix} 1 & 2\pi T & \pi T^2 \\ 0 & 1 & T \\ 0 & 0 & 1 \end{bmatrix}
\end{aligned} \tag{5.22}$$

the corresponding *a posteriori* state estimate can be written as

$$\begin{bmatrix} \Delta\theta \\ \Delta f \\ \Delta\alpha \end{bmatrix}_{k+1} = A_k \begin{bmatrix} \Delta\theta \\ \Delta f \\ \Delta\alpha \end{bmatrix}_k + \begin{bmatrix} k_1 \\ k_2 \\ k_3 \end{bmatrix}_{k+1} \left(Z_{k+1} - H_{k+1} \cdot A_{k+1} \cdot \begin{bmatrix} \Delta\theta \\ \Delta f \\ \Delta\alpha \end{bmatrix}_k \right) \tag{5.23}$$

where $K_{k+1} = [k_1, k_2, k_3]^T_{k+1}$ and $H_{k+1} \cdot A_{k+1} = \left[1, \pi T, \frac{\pi T^2}{3}\right]$.

It is important to note that in [23] the observation matrix H_{k+1} is set approximately as

$$H_{k+1} = [1\ 0\ 0] \tag{5.24}$$

without considering the influence of frequency error or frequency rate error on the discriminator output. In this sense, (5.24) can only work well in case of short integration time and small frequency (and frequency rate) error.

Here in this chapter, the influence of averaging effect [13] in discriminator is considered as shown in (5.22). Finally, the structure 5.23 can be illustrated in Fig.5.8 where the averaging effect is also marked.

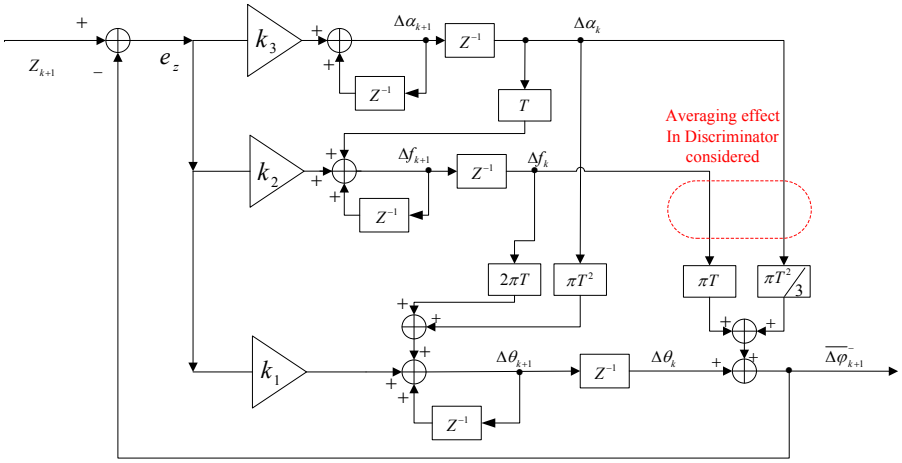

Figure 5.8: Block diagram of the Kalman filter tracking loop. Z^{-1} represents one-step delay in Z domain.

5.5.2 Equivalent Control System

Based on the diagram illustrated in Fig.5.8, we can derive the corresponding e*quivalent control system model* to facilitate the analysis of KF-based tracking loop. It is known that an integrator in the continuous time domain

$$\dot{u}(t) = f(t) \tag{5.25}$$

sampled every T seconds can be expressed as

$$u((k+1)T) = u(T) + \int_{kT}^{(k+1)T} f(t)dt \tag{5.26}$$

Therefore the mathematical discrete approximation illustrated in Fig.5.9 can be applied to (5.26) so as to obtain

$$u(k+1) \approx u(T) + f(k) \cdot T \tag{5.27}$$

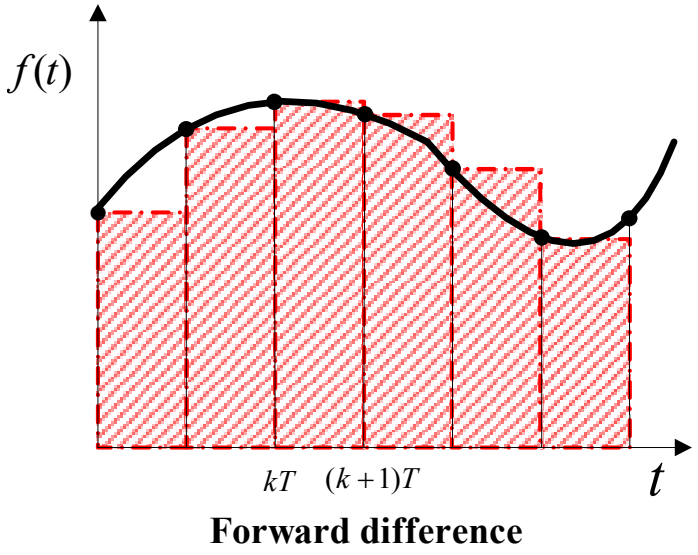

Figure 5.9: Integral approximation.

whose corresponding transfer function in the Z domain is

$$H(Z) = \frac{TZ^{-1}}{1 - Z^{-1}} \tag{5.28}$$

Then, the equivalent control system of the Kalman filter illustrated in Fig.5.8 can be obtained as shown in Fig.3 by substituting the Laplace operator $1/S$ to the Z-transfer function (5.28).

According to Mason's gain formula (MGF), the following transfer function in the domain can be easily derived for the system in Fig.5.10

$$\frac{\varphi_{out}^{-}(S)}{\varphi_{in}(S)} = \frac{(\frac{T\pi k_3}{3} + \pi k_2 + \frac{k_1}{T})S^2 + (2\pi k_3 + \frac{2\pi k_2}{T})S + \frac{2\pi k_3}{T}}{S^3 + (\frac{T\pi k_3}{3} + \pi k_2 + \frac{k_1}{T})S^2 + (2\pi k_3 + \frac{2\pi k_2}{T})S + \frac{2\pi k_3}{T}} \tag{5.29}$$

which conforms to the expression of optimal third-order phase-lock loop in [30].

According to [29], the corresponding noise bandwidth can be computed as

$$\begin{aligned} B_n &= \frac{m_1 \cdot m_2^2 + m_1^2 - m_2 \cdot m_0}{4(m_1 \cdot m_2 - m_0)} \\ &= \frac{m_2}{4} - \frac{m_1^2}{4(m_1 \cdot m_2 - m_0)} \end{aligned} \tag{5.30}$$

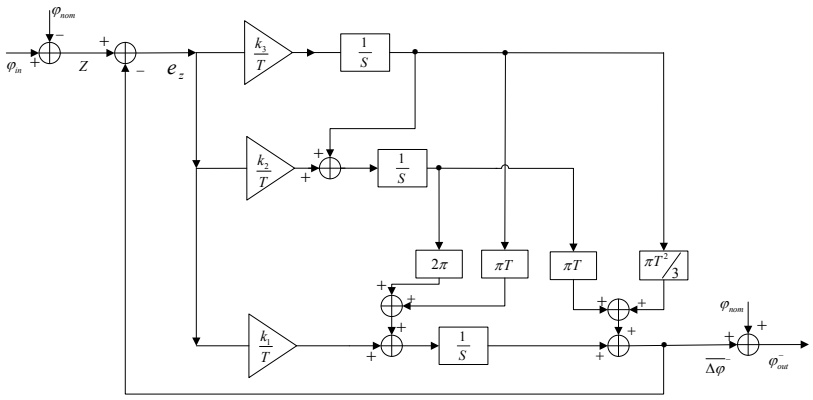

Figure 5.10: The system of the Kalman filter tracking loop in the continuous-time domain.

where

$$\begin{cases} m_0 = \frac{2\pi k_3}{T} \\ m_1 = 2\pi k_3 + \frac{2\pi k_2}{T} \\ m_3 = \frac{T\pi k_3}{3} + \pi k_2 + \frac{k_1}{T} \end{cases} \tag{5.31}$$

So, it can be concluded that the equivalent noise bandwidth of Kalman filter is actually decided by the Kalman gain vector K_k and integration time T (i.e., the parameters in (5.31)) and therefore it evolves over time with K_k .

5.6 Conclusion

In this chapter we presented a detailed description of the practical implementation architecture of an EKF-based tracking loop, discussing in particular the rules adopted for the NCOs update and the run-time determination of the statistical properties of the noise processes, necessary to obtain good performance of the tracking system. Differently from the traditional signal tracking architecture which implements a PLL + DLL pair and updates only the frequency of their NCOs, the EKF-based tracking updates simultaneously both the frequency and phase of the two NCOs governing the local carrier and local code generators. The corresponding mathematical expressions of the

update rules are also given. Furthermore, it is shown that the practical implementation of this tracking architecture in a receiver requires appropriate methods to first initialize, then to determine at run-time the C/N_0 ratio and the amplitude A of the received signal. The implementation of such estimators, both for the initialization stage and for the normal tracking operations, is presented.

Based on this architecture, a software receiver equipped with an EKF-based tracking is tested in a real dynamic scenario, where it is shown that positioning accuracy can be improved dramatically with respect to a traditional tracking architecture. Furthermore, two commercial receivers are also used in the PVT performance comparison, showing that the EKF-based tracking architecture achieves comparable results with the commercial ones even when a basic one-shot LS approach is used to resolve the PVT.

Later in the last part, KF-based tracking loop is analyzed in details, the equivalent control model is derived based on the mathematical expression of Kalman system only concerning carrier tracking. With all these results, it becomes much easier to implement KF-based tracking loop scheme in the frame of traditional tracking loop without changing the original structure too much.

Chapter 6

Conclusions and Recommendations

This chapter summarizes the various aspects of the work presented in this thesis and the main contributions are discussed. Finally based on the conclusion and experience gained in previous chapters, future possible developments are proposed as recommendations.

6.1 Conclusions

The main goal of this thesis is to enhance the receiver techniques in the frame of software receivers, meanwhile, to provide insights into the advanced algorithms. Briefly, this thesis is focused on the enhancement in parameters estimation including frequency, phase and code delay estimates.

• ***Frequency estimation***: First in the traditional acquisition part, rough Doppler frequency estimate can be got from the peak cell in the two-dimensional search space. In theory, this process conforms to ML estimation theory, but due to the search space interval, the initial frequency estimate is not exactly a ML estimate. Therefore the first contribution is to fulfill ML estimation thoroughly. Based on the previous search space, more cells are exploited to get

an approximate ML estimate, and the new treatment only needs one simple further step. Furthermore, this ideal can be extended to design a new FLL discriminator which is the second main work that has been done in this thesis. The new FLL discriminator is different from the traditional counterpart, it computes the frequency error by exploiting the energy of the received signal, so only one single period of data is needed. At the same time, it broadens the pull-in range dramatically which can increase the capability of bearing dynamic stress.

• ***Parameters estimation in vector mode***: In Section 5, an EKF-based tracking loop is analyzed and implemented in the frame of a real software receiver, and the improvement in positioning accuracy is mainly discussed. At the same time, a real scenario campaign is done to evaluate the new proposed scheme by taking two professional receivers as reference. Furthermore, a bigger contribution in this topic is the development of a new method to analyze the KF-based tracking loop, different from other available similar methods, since it directly derives the equivalent control model from the KF system, and then the derived control model serves as a bridge to link the traditional tracking loop and KF system. This analysis can help disclosing the 'secret' of the advanced KF system, at the same time, it can give an insight into the real implementation of the complex KF algorithm in the frame of a real receiver in hardware without too much effort.

6.2 Future work

Based on the work that has been done in this thesis, some recommendations on future work are outlined as follows:

• ***Vector tracking loop***:As mentioned before, KF-based tracking loop can be regarded as 'small-scaled' vector tracking. When it comes to high-level scheme, different channels can be related by vector tracking as shown in Fig.6.1. So the first possible extended work can be related to the design and

implementation of a vector tracking loop. Actually, vector-tracking loop has

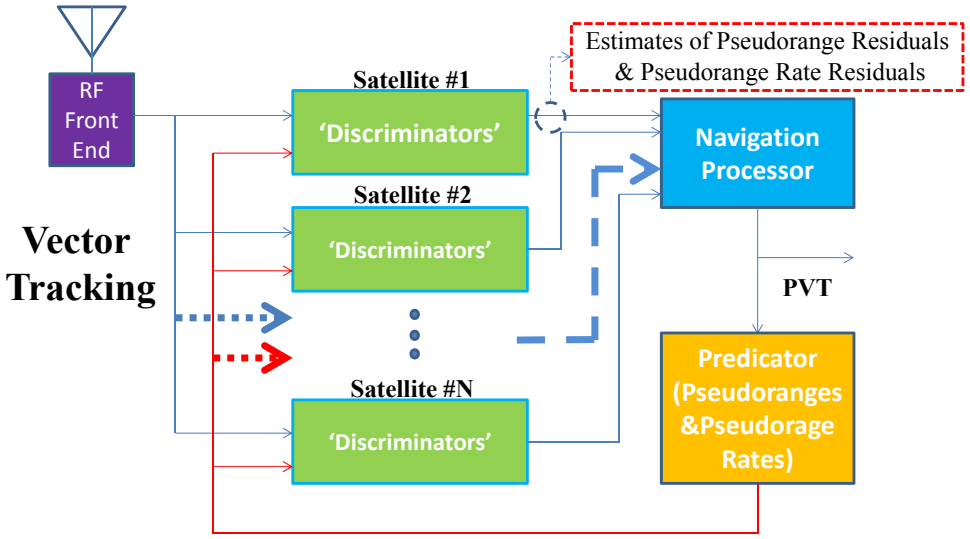

Figure 6.1: Vector tracking scheme.

been studied frequently in previous literature. Here, based on the available results, several key points can still be further studied:

1. The design of feedback, as shown in Fig.6.1, the feedback for each channel is commonly the employment of PVT results. In future, we can also design the partial feedback in every individual channel and re-design the total feedback from PVT part. In addition, comparison should be done to evaluate the performance of the new feedback system.

2. How to assess the criteria to select the correct channels. It is well known, there is one serious potential problem in vector tracking loop that is one abnormal channel can corrupt the other related channels, so criteria should be set to evaluate the health situation of each individual involved channel. At the same time, the system can add or abandon channels in an adaptive manner.

• ***Implementation of a KF-based Tracking Loop in the Frame of Traditional Tracking loop in Hardware***:As discussed in Section 5, KF-based tracking loop is too complex to be implemented directly in hardware.

Based on the in-depth analysis of KF-based tracking loop, the implementation of this algorithm can be achieved only by changing the values of some involved parameters. In this sense, the goal of a real-time KF-based tracking loop can really be achieved without too much effort.

• ***The Detection of Phase Jump***: As mentioned in section 4, frequency error can be computed using the energy rather than phase information, therefore, the new proposed FLL discriminator can also be used as reference to measure wether there is phase jump within two consecutive periods of received data. If there is phase jump within two consecutive periods of data, the frequency error computed from two different algorithms (one is based on phase different, another one is based on energy) will be different.

• ***Integrated Navigation System***: With additional information from other sensors such as IMU, new integrated navigation systems can be developed. The central principle is still the design of how to incorporate the available information to optimize the system.

Bibliography

[1] E.D. Kaplan and C.J. Hegarty, editors. *Understanding GPS Principles and Applications*. Artech House, Norwood, MA, 2006.

[2] Thomas Pany. *Navigation Signal Processing for GNSS Software Receivers*. Artech House, 2010.

[3] J. B. Tsui. *Fundamentals of global positioning system receivers - A software approach*. John Wiley & Sons, Inc., 2000.

[4] B.W. Parkinson and J.J. Spilker, editors. *Global Positioning System: Theory and Applications, Vol. I*. American Institute of Aeronautics and Astronautics, Washington, D.C., 1996.

[5] S.M. Kay. *Fundamentals of Statistical Signal Processing, Vol. I: Estimation Theory*. Prentice-Hall, Upper Saddle River, NJ, 1993.

[6] Curran J.T.; Lachapelle G.; Murphy C.C. Improving the design of frequency lock loops for gnss receivers. *IEEE Transaction on aerospace and electronic system*, 48:850–868, 2012.

[7] Borio D.; Camoriano L.; Lo Presti L.; Fantino M. Dtft-based frequency lock loop for gnss applications. *IEEE Transactions on Aerospace and Electronic Systems*, 44:595–612, 2008.

[8] Ma C.; Lachapelle G.; Cannon M.E. Implementation of a software gps receiver. In *Proceedings of ION GNSS 2004 (Session A3)*, pages 142–149, Long Beach, USA,, September 2004.

[9] X. Tang; E. Falletti; L. Lo Presti. Fast nearly ml estimation of doppler frequency in gnss signal acquisition process. *Sensors*, 13:5649–5670, 2013.

[10] Yu-Hsuan Chen Jyh-Ching Juang. Phase/frequency tracking in a gnss software receiver. *IEEE Journal of Selected Topics in Signal Processing*, 3, August 2009.

[11] Tao Lin. *Contributions to a Context-Aware High Sensitivity GNSS Software Receiver*. PhD thesis, University of Calgary, 2013.

[12] Florence M. *Development and testing of an L1 combined GPS-Galileo software receiver*. PhD thesis, University of Calgary, 2010.

[13] M. Petovello and G.Lachapelle. Comparison of vector-based software receiver implementations with application to ultra-tight gps/ins integration. In *ION GNSS 2006*, Fort Worth TX, USA, September 2006.

[14] Bernd Eissfeller Jong-Hoon Won, Dominik Dotterbock. Performance comparison of different forms of kalman filter approach for a vector-based gnss signal tracking loop. In *ION GNSS 2009*, September 2009.

[15] X. Tang; Falco G.; E. Falletti; L. Lo Presti. Practical implementation and performance assessment of an extended kalman filter-based signal tracking loop. In *International Conference on Localization and GNSS(ICL-GNSS)*, 2013.

[16] Pejman Lotfali Kazemi. *Development of New Filter and Tracking Schemes for Weak GPS Signal Tracking*. PhD thesis, University of Calgary, 2010.

[17] James L. Garrison Nesreen I. Ziedan. Bit synchronization and doppler frequency removal at very low carrier to noise ratio using a combination of viterbi algorithm with an extended kalman filter. In *ION GPS/GNSS 2003*, 2003.

[18] Hee Jung Mark L. Psiaki. Extended kalman filter methods for tracking weak gps signals. In *ION GPS/GNSS 2003*, 2003.

[19] etc. Christophe MACABIAU, Lina DEAMBROGIO. Kalman filter based robust gnss signal tracking algorithm in presence of ionospheric scintillations. In *ION GNSS 2012*, 2012.

[20] Lawrence R. Weill. A high performance code and carrier tracking architecture for ground-based mobile gnss receivers. In *ION GNSS 2010*, 2010.

[21] G. Lachapelle Cillian O¡¯Driscoll. Comparison of traditional and kalman filter based tracking architecture. In *European Navigation Conference 2009, Naples, Italy*, 2009.

[22] G. Lachapelle Dina Reda Salem, Cillian O¡¯Driscoll. Methodology for comparing two carrier phase tracking techniques. *GPS Solutions*, 16:197–207, 2012.

[23] B. Jong-Hoon Won; Pany, T.; Eissfeller. Characteristics of kalman filters for gnss signal tracking loop. *IEEE Transactions on Aerospace and Electronic Systems*, 48:3671–3681, 2012.

[24] B.P.Lathi. *Modern Digital and Analog Communication System.* Oxford University Press, Inc., 1998.

[25] Betz J. The offset carrier modulation for gps modernization. In *ION Technical meeting*, Cambridge, Massachusetts, 1999.

[26] European Union and European Space Agency. *European GNSS (Galileo) Open Service ICD*, 2010.

[27] Alan V. Oppenheim. *signals and systems.* Prectice Hall, 1997.

[28] Peter S. Maybeck. *Stochastic models, estimation, and control.* ACADEMIC PRESS New York, 1979.

[29] P. Y. Hwang R. G. Brown, editor. *Introduction to Random Signals and Applied Kalman Filtering.* John Wiley&Sons, 1997.

[30] E. Rechtin R. Jaffe. Design and performance of phase-lock circuits capable of near-optimum performance over a wide range of input signal and noise levels. *IRE Transactions on Information theory*, 1:66–76, 1955.

[31] J. B. THOMAS S. A. STEPHENS. Controlled-root formulation for digital phase-locked loops. *IEEE TRANSACTIONS ON AEROSPACE AND ELECTRONIC SYSTEMS*, 31, 1995.

[32] Jacobsen E. Kootsookos P. Fast. Accurate frequency estimators. *IEEE Signal Process. Mag.*, 24:123–125, 2007.

[33] Quinn B.G. Estimating frequency by interpolation using fourier coefficients. *IEEE Trans. on Signal Process.*, 42:1264–1268, 1994.

[34] Quinn B.G. Estimation of frequency, amplitude, and phase from the dft of a time series. *IEEE Trans. on Signal Process.*, 45:814–817, 1997.

[35] Macleod M.D. Fast high accuracy estimation of multiple cisoids in noise. *Signal Processing V: Theories and Applications*, pages 333–336, 1990.

[36] Macleod M.D. Fast nearly ml estimation of the parameters of real or complex single tones or resolved multiple tones. *IEEE Trans. Signal Process.*, 46:141–148, 1998.

[37] Eric Jacobsen. On local interpolation of dft outputs.

[38] Kay S.M. A fast and accurate single frequency estimator. *IEEE Trans. Acoust., Speech, Signal Processing*, 37:1987–1990, 1989.

[39] Candan C. A method for fine resolution frequency estimation from three dft samples. *IEEE ASSP MagazineSignal Processing Letters*, 18:351 – 354, 2011.

[40] Motella B Lo Presti L. The math of ambiguity. *Inside GNSS 2010*, pages 20–28, 2010.

[41] X. Tang; E. Falletti; L. Lo Presti. Fine doppler frequency estimation in gnss signal acquisition process. In *In Proceedings of 6th ESA Workshop on Satellite Navigation Technologies and European Workshop on GNSS Signals and Signal Processing*, 2012.

[42] Lo Presti L.; Xuefen Z.; Fantino M.; Mulassano P. Gnss signal acquisition in the presence of sign tansition. *IEEE Journal of selected topics in signal processing*, 3:557–570, 2009.

[43] Kai Borre. *A Software-Defined GPS and Galileo Receiver (A Single-Frequency Approach)*. Birkhauser Boston, 2007.

[44] Falletti E.; Margaria D.; Motella B. A complete educational library of gnss signals and analysis functions for navigation studies. *Coordinates*

2009, pages 30–34, 2009.

[45] Borio D.; O¡¯driscoll C;Lachapelle G. Composite gnss signal acquisition over multiple code periods. *IEEE Trans. On Aerospace And Electronic System*, 46:193–206, 2010.

[46] G. Lachapelle D. Borio, C. O¡¯Driscoll. Composite gnss signal acquisition over multiple code periods. *IEEE Transactions on Aerospace and Electronic Systems*, 46, 2010.

[47] T.H.Ta; F. Dovis; D. Margaria; L.Lo Presti. Comparative study on joint data/pilot strategies for high sensitivity galileo e1 open service signal acquisition. *IET Radar Sonar and Navigation*, 4:764¨C779, 2010.

[48] M.Fantino M. Tahir, L.Lo Presti. A novel quasi-open loop architecture for gnss carrier recovery system. *International Journal of Navigation and Observation*, 2012.

[49] E. Aboutanios S. Reisenfeld. A new algorithm for the estimation of the frequency of a complex exponential in additive gaussian noise. *IEEE Communications Letters*, 7, 2003.

[50] G. Lachapelle D. Borio, N. Sokolova. Doppler measurement accuracy in standard and high sensitivity global navigation satellite system receivers. *IET Radar, Sonar and Nav.*, 5:657–665, 2011.

[51] H.-G. Yeh. Real-time implementation of a narrow-band kalman filter with a floating-point processor dsp32. *IEEE Trans. on Industrial Electronics*, 37:13–18, 1990.

[52] L. Lo Presti E. Falletti, M. Pini. Low complexity carrier to noise ratio estimators for gnss digital receiver. *IEEE Trans. on Aer. and Electronic Systems*, 47:420–437, 2011.

[53] R. Scopigno; D. Margaria;T. Acarman;U. Peker;K. Par; E. Kaplan. Gloves manifesto: leveraging gnss time-space information to improve vanets performances and enrich vanets services. In *Proc. of 9th ITS European Congress*, 2013.

[54] V. Palma; F. Toni; etc. Assessment of augmentation network solution for

the evolution of the ertms-etcs train control system. In *Eur. Navigation Conf.*, 2013.

[55] M. C. Cossio Gutierrez G. Falco, A. Puras Trueba. Multi-gnss receiver/imu system aimed at the design of a heading-contrained tightlycoupling algorithm. In *ICL-GNSS 2013*, 2013.

[56] P. Maybeck. *Stochastic models, estimation, and control.* Academic Press, 1979.